

Volume 4 | Issue 2 | Autumn 2018



Shahid Chamran University of Ahvaz

# Journal of Hydraulic Structures

Scientific Professional Journal



نشریه علمی پژوهشی

ISSN 2345-413X  
<http://jhs.scu.ac.ir>

# **In the name of GOD**

*Journal of Hydraulic Structures  
Department of Civil Engineering  
Faculty of Engineering  
Shahid Chamran University of Ahvaz*

# JORNAL OF HYDRAULIC STRUCTURES

SHAHID CHAMRAN UNIVERSITY OF AHVAZ

**Manager:** Prof. Hamid R. Ghafouri

**Editor-in-chief:** Dr. Ali Haghighi

**Editorial coordinator:** Dr. Seyed Mohammad Ashrafi

Department of Civil Engineering, Faculty of  
Engineering, Shahid Chamran University of Ahvaz,  
Ahvaz, Iran.

## Members

**Prof. Hossein M. V. Samani**

Civil Engineering Department, Shahid Chamran University of  
Ahvaz, Ahvaz, Iran

**Prof. Hamid R. Ghafouri**

Civil Engineering Department, Shahid Chamran University of  
Ahvaz, Ahvaz, Iran

**Dr. Ali Haghighi**

Civil Engineering Department, Shahid Chamran University of  
Ahvaz, Ahvaz, Iran

**Prof. Mahmood S. Bajestan**

Hydraulic Structures Department, Shahid Chamran University of  
Ahvaz, Ahvaz, Iran

**Prof. Saeed R. S. Yazdi**

Civil Engineering Department, K.N. Toosi University of Technology,  
Tehran, Iran

**Dr. Mohammad S. Pakbaz**

Civil Engineering Department, Shahid Chamran University of  
Ahvaz, Ahvaz, Iran

**Dr. Arash Adib**

Civil Engineering Department, Shahid Chamran University of Ahvaz,  
Ahvaz, Iran

**Dr. Mojtaba Labibzadeh**

Civil Engineering Department, Shahid Chamran University of  
Ahvaz, Ahvaz, Iran

**Prof. Helena M. Ramos**

Instituto Superior Técnico (IST), University of Lisbon

**Dr. S. Mohammad Ashrafi**

Civil Engineering Department, Shahid Chamran University of  
Ahvaz, Ahvaz, Iran

**Dr. S. Abbas Haghshenas**

Institute of Geophysics, University of Tehran | UT, Tehran, Iran

**Dr. Mohammad Zounemat-Kermani**

Department of Water Engineering, Shahid Bahonar University of  
Kerman, Kerman, Iran

**Dr. Taher Rajaei**

Civil Engineering Department, University of Qom, Qom, Iran

**Dr. Mohammad Vaghefi**

Civil Engineering Department, Faculty of Engineering, Persian Gulf  
University, Bushehr, Iran

**Dr. A. A. Telvari**

Soil Conservation and Watershed Management Research  
Institute; Department of Civil Engineering, Islamic Azad University,  
Ahvaz branch, Ahvaz, Iran



## CONTENTS

VOL 4, Issue 2, Autumn 2018

### I. *In the name of God*

### II. *Table of Contents*

### III. *Aims and Scope*

#### 01 A Mass Conservative Method for Numerical Modeling of Axisymmetric flow

R. Asadi

#### 10 Development of A new Hydraulic Relationship for Submerged Slide Gates

S. Jahan Kohan; Hossein M.V. Samani; H. Ebrahimi

#### 17 Effect of rice husk ash on the swelling pressure of bentonite soil stabilized with lime in the presence or lack of sulfate

Mohammad S. Pakbaz; S. SeyedAlizadeh Ganji

#### 27 Characteristic Based Split Finite Element for Unsteady Dam-Break Problem

J. Parsa

#### 42 Boundary Integral Equations for Quasi- Static Unsaturated Porous Media

E. Jabbari; M. Behnia

#### 60 Evaluating performance of meta-heuristic algorithms and decision tree models in simulating water level variations of dams' piezometers

R. Salajegheh; A. Mahdavi-Meymand; M. Zounemat-Kermani

## Aims and Scope

Hydraulic Structure Journal is an interdisciplinary journal which publishes high-quality peer-reviewed articles addressing the latest developments and applied methods **in construction, maintenance, management, and operation policy of Hydraulic Structures.**

The Journal aims at providing an efficient route to fast-track publication, **within 10-12 weeks after manuscript submission.** Manuscripts will be considered for publication in the following categories: **research articles, technical notes, case reports and discussions.**

The general areas covered by the Journal include:

- Technical and methodological advances in application, design/selection, production, modification of construction materials
- Advances in numerical and analytical methods
- Hydro informatics and soft computing
- Hydraulic aspects of hydraulic structures
- Applied surface and subsurface hydrology and hydrometeorology
- Forecasting approaches in water resources engineering
- Economic and social aspects of hydraulic structures
- Uncertainty analysis and risk management in hydraulics and water resources engineering
- Application of Nanotechnology in Hydraulic Structures
- Geotechnics of Hydraulic Structures
- Damage detection techniques

The following might be considered as hydraulic structures:

- Dams and associated structures
- River and Watershed Structures
- Offshore and Onshore Structures
- Irrigation and Drainage Channel Networks
- Bridges
- Water Storage and Conveyance Structures
- Pipelines and Pump Stations
- Sewerage Systems
- Water and Wastewater Treatment Plants
- Historical Water Structures

## General Information

**Title:** Journal of Hydraulic Structures

**Subject:** Hydraulics and water resources engineering

**Coverage area:** International

**Journal Type:** Scientific and technical

**License Holder:** Shahid Chamran University of Ahvaz

**Editor-in-Chief:** Dr. Ali Haghighi

**Manager:** Prof. Hamid R. Ghafouri

**Editorial coordinator:** Dr. Seyed Mohammad Ashrafi

**Language Editor:**

Dr. Mohammad Azizipour

**Address:** Department of Civil Engineering, Faculty of Engineering, Shahid Chamran University of Ahvaz

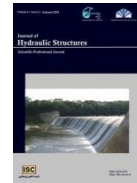
**Phone #:** +986133330011-19 (5610 & 5603)

**Fax #:** +986113337010

**Language:** English

**Email:** jhs@scu.ac.ir

**Website:** jhs.scu.ac.ir



## A Mass Conservative Method for Numerical Modeling of Axisymmetric flow

Roza Asadi<sup>1</sup>

### Abstract

In this paper, the axisymmetric flow toward a pumping well has been numerically solved by the cell-centered finite volume method. The numerical model is discretised over unstructured and triangular-shaped grid which allows simulating inhomogeneous and complex-shaped domains. Due to the non-orthogonality of the irregular grids, the multipoint flux approximation (MPFA) schemes are used to discretize the flux term. In this work, the diamond scheme as the MPFA method has been employed and the least square method is applied to express the full discrete form of the vertex-values of the hydraulic head. The scheme has been verified via the Theis solution, as a milestone in well hydraulics. The numerical results show the capability of the developed model in evaluating transient drawdown in the confined aquifers. The proposed numerical model leads to the stable and local conservative solutions contrary to the standard finite element methods. Also this numerical technique has the second order of accuracy.

**Keywords:** Axisymmetric radial flow, Cell-centered finite volume method, MPFA method, Diamond scheme.

Received: 11 March 2018; Accepted: 29 Jun 2018

### 1. Introduction

Groundwater accounts for about 30 percent of the world's supply of fresh water. In arid and semi-arid regions this resource serves as an alternative to the surface reservoirs of water. These issues make well hydraulics an important aspect in hydrological and water science problems. The mathematical analysis of well pumping on head decline in confined aquifers first provided by Theis in 1935 [1]. The analytical solutions for other types of aquifers such as leaky and unconfined aquifer were obtained by Hantush and Jacob [2] and Neuman [3-6], respectively. However, the analytical solutions are limited to the ideal cases. Thus, numerical methods have been developed to model the real and complicated circumstances. Despite the traditional numerical schemes such as the standard finite element method developed extensively to model the groundwater problems, it suffers from the numerical oscillations especially in inhomogeneous porous media [7-10]. In order to resolve the numerical instabilities and provide

---

<sup>1</sup> Department of Civil Engineering, K.N. Toosi University of Technology, Tehran, Iran, asadi@kntu.ac.ir  
(Corresponding author)

mass conservative solution, the finite volume methods (FVMs) have been formulated to simulate the groundwater flow equation [10-15]. Since the unstructured grid is the most efficient and flexible mesh to model the complex geometries and sharp heterogeneities [16], this type of mesh is applied in this study. Due to non-orthogonality of the irregular grids, MPFA schemes are used to discretize the flux term [17,18]. In this work, the diamond scheme as the MPFA method has been employed on the unstructured triangular grids [19-23]. Moreover, the least square method is applied to express the full discrete form of the vertex-values of the hydraulic head. This procedure results in the cell-centered finite volume method (CC-FVM). It was demonstrated in [15, 21] that this scheme provides second-order accurate solutions.

In [13], this discretization scheme was combined with the mechanics equation to simulate the Biot's model [24] in two-dimensional domain. It was illustrated that the proposed numerical method result in stable and local conservative solutions. In addition, it was shown that the unstructured grid makes the model well-suited for simulating heterogeneous domains and complicated geometries [13].

The axisymmetric flow toward a pumping well has been numerically solved by the cell-centered finite volume method. Since the computational cost of the axially symmetric model is less than the equivalent three dimensional one, this simplification has been assumed in the formulations. Indeed, in this study the effectiveness of the model in simulating flow in confined aquifer subjected to pumping has been investigated.

## 2. Mathematical formulation

The governing equation for fluid flow in a confined aquifer is:

$$S_s \frac{\partial h}{\partial t} + \text{div} \mathbf{v} = f \quad (1)$$

where  $S_s$  is the specific storage coefficient which can be defined as  $\rho_w g(\alpha + n\beta)$ ,  $\mathbf{v} = \bar{\mathbf{K}} \nabla h$  is the Darcy's velocity,  $h$  denotes the hydraulic head and  $\bar{\mathbf{K}}$  is the tensor form of the hydraulic conductivity.  $t$  is time,  $\rho_w$  denotes the density of fluid,  $n$  is the porosity and  $\alpha$  and  $\beta$  are the compressibility of aquifer and fluid, respectively. Finally,  $f$  is a sink /source term.

The required boundary conditions can be written as follows:

$$h = h_D \quad \text{on} \quad \Gamma_h \quad (2)$$

$$\mathbf{v} \cdot \mathbf{n} = q \quad \text{on} \quad \Gamma_q \quad (3)$$

where  $h_D$  and  $q$  are the boundary values of the hydraulic head and flux, respectively. The unit normal vector  $\mathbf{n}$  is pointing outward from the boundaries which are defined as:

$$\Gamma_h \cup \Gamma_q = \partial\Omega \quad (4)$$

$$\Gamma_h \cap \Gamma_q = \emptyset \quad (5)$$

## 3. Numerical model

A detailed description of the numerical formulations is presented in this section. For this purpose at the first stage, the FVM method has been applied for discretizing the flow equation and then a diamond scheme has been implemented to approximate the flux term. As mentioned earlier the variation of the hydraulic properties in the angular direction has been neglected and the model simulates the planar domain.

### 3.1.1 The CC-FVM

To apply the FVM, integral of the flow equations is calculated over the generic control volume  $V_i$ :



$$\int_{V_i} \left( S_s \frac{\partial h}{\partial t} + \text{div} \mathbf{v} \right) dV = \int_{V_i} f dV \quad (6)$$

where in the above equation  $dV$  is the volume element which is defined as  $rdrd\theta dz$  in the cylindrical coordinates. For the axisymmetric case the above equation can be reduced to the double integral as follows:

$$\int_{\Omega_i} r \left( S_s \frac{\partial h}{\partial t} + \text{div} \mathbf{v} \right) d\Omega = \int_{\Omega_i} r f d\Omega \quad (7)$$

where  $d\Omega$  is the area element such that  $d\Omega = drdz$ ,  $\Omega_i$  denotes the two dimensional control volume and  $r$  and  $z$  are the radial and axial coordinates, respectively. By implementing theorem of Gauss–Green to Eq. (7), the integral form of the flow equation will read as:

$$\int_{\Omega_i} r \left( S_s \frac{\partial h}{\partial t} \right) d\Omega - \int_{\partial\Omega_i} \mathbf{n} \cdot \bar{\mathbf{K}} \nabla h r d\Gamma = \int_{\Omega_i} r f d\Omega \quad (8)$$

The symbols  $\partial\Omega_i$  denotes the control volume's boundary. With approximating hydraulic head and the source/sink term at the centroid of the control volumes, the discretized form of the flow equation is obtained as follows:

$$\bar{r} S_s \frac{\partial h_i}{\partial t} |\Omega_i| + \sum_{\Gamma_{ij} \in \partial\Omega_i} r_e V_{ij} |\Gamma_{ij}| = \bar{r} f_i |\Omega_i| \quad (9)$$

in which  $h_i$  is cell-averaged value of the hydraulic head.  $\Gamma_{ij}$  is the internal edge between two adjoining cells ( $\Omega_i$  and  $\Omega_j$ ) and the absolute value of  $\Gamma_{ij}$  ( $|\Gamma_{ij}|$ ) represents its length.  $V_{ij}$  denotes the flux across this edge and  $|\Omega_i|$  is used to present area of the control volume.  $\bar{r}$  and  $r_e$  denote the radial distances from the cell center and the midpoint of the edge  $\Gamma_{ij}$ .  $f_i$  indicates the cell average of the sink/source term.

The velocity term is discretized with the equation proposed by Coudière et al. [20]:

$$V_{ij} = -\frac{1}{|\Gamma_{ij}|} \int_{\Gamma_{ij}} \mathbf{n} \cdot \bar{\mathbf{K}} \nabla h d\Gamma \quad (10)$$

In the next section this integral flux has been approximated by a multipoint flux scheme [13, 18-20]. Fig. 1 depicts the different parameters introduced in the equations.

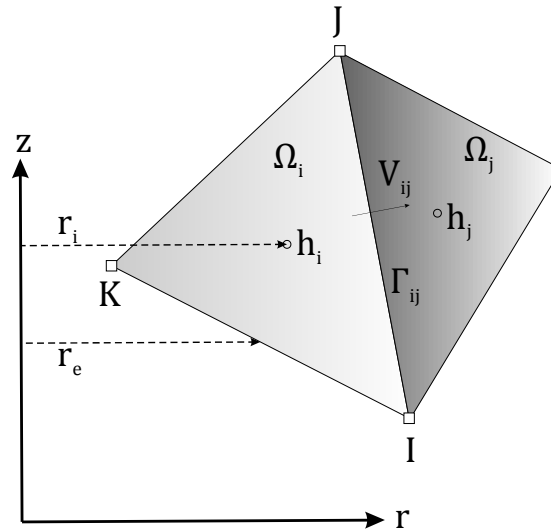


Figure 1. Symbols used in the numerical formulations

### 3.1.2 Approximating flux integral

As mentioned earlier, a diamond scheme as a multipoint flux approximation is applied to evaluate the flux at the interface of the cells. In this procedure, the gradient of hydraulic head is calculated with the values of head at the vertices and center of the cells [18-20, 22, 25]. Indeed, using only cell center values of hydraulic head result in inaccurate solution for the unstructured grids [18, 25]. The gradient of hydraulic head across the boundary  $\Gamma_{ij}$  is given by [13, 15, 19, 20, 23]:

$$\psi_{ij} = \left( \frac{h_j - h_i}{D_{ij}} - \cot \theta \frac{h_j - h_I}{|\Gamma_{ij}|} \right) \mathbf{n}_{ij} + \frac{h_j - h_I}{|\Gamma_{ij}|} \mathbf{t}_{ij} \quad (11)$$

In the above equation,  $\mathbf{n}_{ij}$  indicates the unit normal of  $\Gamma_{ij}$  and is assumed that pointing from  $i$  to  $j$  (Fig. 2), and  $\mathbf{t}_{ij}$  is the tangent vectors of the respective face. As illustrated in figure 2,  $h_i$  and  $h_I$  are the head values at the centroid of cell  $i$  and vertex  $I$ , and  $h_j$  and  $h_J$  are the corresponding values at the center of the control volume  $j$  and node  $J$ , respectively. As shown in Fig.2, the parameter  $D_{ij}$  is defined as  $D_{ij} = d_{ij} + d_{ji}$ , in which  $d_{ij}$  and  $d_{ji}$  are the length of the lines between points  $i$  and  $j$  and the cell face, respectively [13, 15, 19, 20, 23]. Other parameters in Eq.(11) are illustrated in Fig.(2).

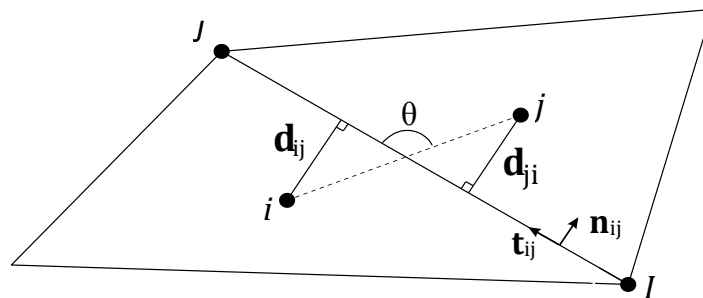


Figure 2. Parameters used in the multipoint flux stencil



Combining Eq. (10) and (11), yields the full discrete form of flux as [13, 19, 20]:

$$V_{ij} = -\kappa \psi_{ij} \cdot \mathbf{n}_{ij} \quad (12)$$

In the above equation, the conductivity tensor  $\kappa$  is the full matrix which can be expressed as follows [13, 19, 20]:

$$\kappa = \frac{1}{|\Gamma_{ij}|} \int_{\Gamma_{ij}} \bar{\mathbf{K}} d\Gamma = \begin{bmatrix} \kappa_{nn} & \kappa_{nt} \\ \kappa_{tn} & \kappa_{tt} \end{bmatrix} \text{ in } (\mathbf{n}_{ij}, \mathbf{t}_{ij}) \quad (13)$$

By substituting Eqs. (10) and (12) into Eq. (11), the numerical flux reads as [13, 19, 20, 23]:

$$V_{ij} = -\kappa_{nn} \frac{h_j - h_i}{D_{ij}} - (\kappa_{nt} - \cot \theta \kappa_{nn}) \frac{h_j - h_i}{|\Gamma_{ij}|} \quad (14)$$

Finally by interpolating head values at vertices in terms of the cell center values, the FV discretization will be completed [18, 20]. Averaging procedure for computing the weight factors is the least squares algorithm [15, 19-22]. By applying this averaging procedure,  $h_I$  is calculated as follows:

$$h_I = \sum_{i=1}^{N_I} w_i h_i \quad (15)$$

The above summation is done over the cells common to the point I, and the weighting function  $w_i$  is defined for any control volume sharing vertex I as [13, 19, 20]:

$$w_i = \frac{1 + \Lambda_r(r_i - r_I) + \Lambda_z(z_i - z_I)}{N_I + \Lambda_r R_r + \Lambda_z R_z} \quad (16)$$

where  $r_i$  and  $r_I$  are the radial distances of the cell center  $i$  and vertex I, respectively.  $z_i$  and  $z_I$  denote the vertical distances of  $i$  and I from the z-axis. Also the following equations are used to formulate other functions in Eq. (16) [13, 19, 20]:

$$\Lambda_r = \frac{I_{rz} R_z - I_{zz} R_r}{I_{rr} I_{zz} - I_{rz}^2} \quad (17)$$

$$\Lambda_z = \frac{I_{rz} R_r - I_{rr} R_z}{I_{rr} I_{zz} - I_{rz}^2} \quad (18)$$

$$I_{rr} = \sum_{i=1}^{N_I} (r_i - r_I)^2 \quad (19)$$

$$I_{zz} = \sum_{i=1}^{N_I} (z_i - z_I)^2 \quad (20)$$

$$I_{rz} = \sum_{i=1}^{N_I} (r_i - r_I) (z_i - z_I) \quad (21)$$

$$R_r = \sum_{i=1}^{N_I} (r_i - r_I) \quad (22)$$

$$R_z = \sum_{i=1}^{N_I} (z_i - z_I) \quad (23)$$

By substituting Eqs. (15) and (16) into Eq.(14), the final discrete form of this equation can be obtained. The similar procedure has been performed for all faces of each control volume to complete discretization of Eq.(9).

#### 4 Numerical result

To verify the proposed scheme, the Theis solution has been solved and the numerical results have been compared with the analytical solutions. The validation demonstrates the effectiveness of the numerical technique for modeling the radial flow toward wells in confined aquifers. Moreover, to construct the triangular grids, NETGEN algorithm has been implemented as the mesh generator tool [26] and all of the numerical codes have been written in MATLAB 2010 software.

The first analytical solution for the drawdown problem in the confined aquifer was derived by Theis (1935) [1]. To simplify the problem the following assumptions have been made in the Theis solution:

1. The confined aquifer is considered as a homogeneous, isotropic porous media and has infinite horizontal extent.
2. The piezometric surface is considered horizontal prior to pumping.
3. The well is fully penetrated and the pumping rate is constant.
4. The radial flow towards well is horizontal.
5. The radius of the pumping well is very small.
6. The layer has uniform extent and confined top and bottom.
7. Water is released from the porous media as head declines [27, 28].

These conditions are illustrated in Fig. 3. With the above assumptions, the drawdown  $s'$  is calculated as [27, 28]:

$$s' = \frac{Q}{4\pi T} \int_u^\infty \frac{e^{-y}}{y} dy \quad (24)$$

where  $Q$  is the pumping rate,  $T$  denotes transmissivity, the parameter  $u$  is defined as  $\frac{r^2 S}{4Tt}$  and  $S$  is the storage coefficient [27,28].

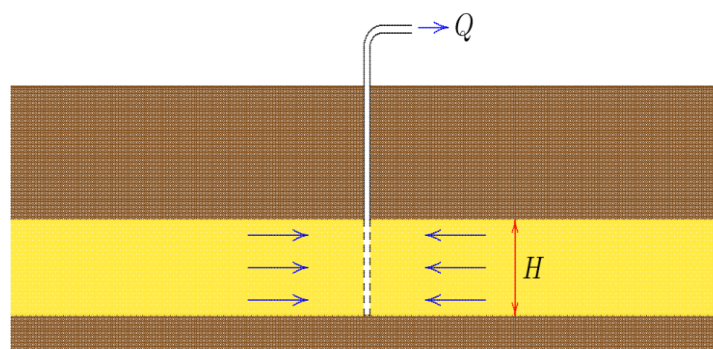


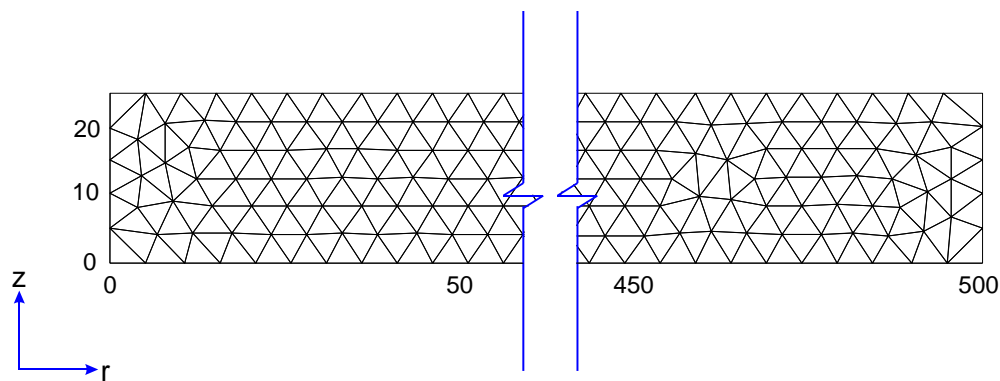
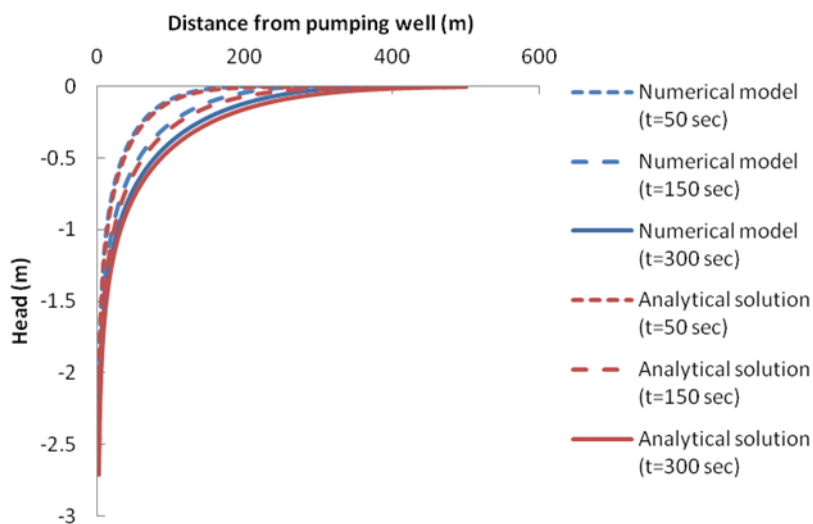
**Figure 3. Schematic of the Theis problem**

To solve the problem following values are considered for the confined aquifer:

**Table 1. Hydraulic parameters of the porous medium**

Parameters	Values
Thickness of the aquifer	25 m
Horizontal extent	500 m
Pumping rate	$Q = 0.2 \text{ m}^3/\text{sec}$
Transmissivity	$T = 6.37 \times 10^{-2} \text{ m}^2/\text{sec}$
Storage coefficient	$S = 8.49 \times 10^{-4}$

The computational mesh is shown in Fig.4. In Fig.5, the numerical and analytical solutions are compared. As illustrated in Fig. 5, numerical results closely correspond to the analytical solutions.

**Figure 4. This problem: Grid layout****Figure 5. This problem: comparison between numerical and analytical solutions**

## 5. Conclusions

This study presents a mass conservative method to model the axisymmetric groundwater flow toward a pumping well. Since the MPFA methods use head values in more than two cells in the unstructured grids, applying this scheme improves the accuracy of the result.

Furthermore, the diamond method has been implemented to construct the flux expression in terms of head values at the vertices and cell centers. Moreover, to interpolate the hydraulic values at the vertices, the least square method has been applied. Finally, to investigate the efficiency of the proposed numerical scheme, the model is verified against the Theis solution as a milestone in well hydraulics. The result illustrates that the model successfully simulates the transient drawdown in the confined aquifers.

## References

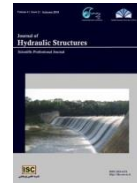
1. Theis CV (1935) The relation between the lowering of the piezometric surface and the rate and duration of discharge of a well using ground-water storage. Transactions American Geophysical Union, 16, 519–24.
2. Hantush, MS, Jacob CE (1955) Non-steady radial flow in an infinite leaky aquifer. Eos, Transactions American Geophysical Union, 36(1), 95-100.
3. Neuman SP (1972) Theory of flow in unconfined aquifers considering delayed gravity response. Water Resources Research 8(4), 1031–1045.
4. Neuman SP (1973) Supplementary comments on theory of flow in unconfined aquifers considering delayed gravity response. Water Resources Research 9(4), 1102–1103.
5. Neuman SP (1974) Effect of partial penetration on flow in unconfined aquifers considering delayed gravity response. Water Resources Research 10(2), 303–312.
6. Neuman SP (1975) Analysis of pumping test data from anisotropic unconfined aquifers. Water Resources Research, 11(2), 329–345.
7. Vermeer PA, Verruijt A (1981) An accuracy condition for consolidation by finite elements. International Journal of Numerical and Analytical Methods in Geomechanics, 5(1), 1-14.
8. Murad MA, Loula AFD (1992) Improved accuracy in finite element analysis of Biot's consolidation problem. Computer Methods in Applied Mechanics and Engineering 95(3), 359–382.
9. Ferronato M, Castelletto N, Gambolati G (2010) A fully coupled 3-D mixed finite element model of Biot consolidation. Journal of Computational Physics, 229(12), 4813–4830.
10. Kim J (2010) Sequential methods for coupled geomechanics and multiphase flow. PhD thesis, Stanford University.
11. Asadi R, Ataie-Ashtiani B (2015) A comparison of finite volume formulations and coupling strategies for two-phase flow in deforming porous media. Computers and Geotechnics, 67, 17-32.
12. Asadi R, Ataie-Ashtiani B, Simmons CT (2014) Finite volume coupling strategies for the solution of a Biot consolidation model. Computers and Geotechnics, 55, 494-505.
13. Asadi R, Ataie-Ashtiani B (2016) Numerical modeling of subsidence in saturated porous media: A mass conservative method. Journal of hydrology, 542, 423-436.
14. Caviedes-Voullième D, Garcı P, Murillo J (2013) Verification, conservation, stability and efficiency of a finite volume method for the 1D Richards equation. Journal of hydrology, 480, 69-84.

15. Manzini G, Ferraris S (2004) Mass-conservative finite volume methods on 2-D unstructured grids for the Richards' equation. *Advances in Water Resources*, 27(12), 1199-1215.
16. Lee SH, Jenny P, Tchelepi HA (2002) A finite-volume method with hexahedral multiblock grids for modeling flow in porous media. *Computers and Geosciences*, 6(3-4), 353-379.
17. Edwards MG (2002) Unstructured, control-volume distributed, full-tensor finite-volume schemes with flow based grids. *Computational Geosciences*, 6(3-4), 433-452.
18. Szymkiewicz A (2012) Modelling water flow in unsaturated porous media: accounting for nonlinear permeability and material heterogeneity. Springer Science & Business Media.
19. Coudière Y, Villedieu P (2000) Convergence rate of a finite volume scheme for the linear convection-diffusion equation on locally refined meshes. *Mathematical Modelling and Numerical Analysis*, 34(6), 1123-1149.
20. Coudière Y, Vila JP, Villedieu P (1999) Convergence rate of a finite volume scheme for a two dimensional convection–diffusion problem, *Mathematical Modelling and Numerical Analysis*, 33, 493–516.
21. Bertolazzi E, Manzini G (2004) A cell-centered second-order accurate finite volume method for convection–diffusion problems on unstructured meshes. *Mathematical Models and Methods in Applied Sciences*, 14(8), 1235-1260.
22. Bertolazzi E, Manzini G (2005) A unified treatment of boundary conditions in least-square based finite-volume methods. *Computers & Mathematics with Applications*, 49(11), 1755-1765.
23. Bevilacqua I, Canone D, Ferraris S (2011) Acceleration techniques for the iterative resolution of the Richards equation by the finite volume method. *International Journal for Numerical Methods in Biomedical Engineering*, 27(8), 1309-1320.
24. Biot MA (1941) General theory of three-dimensional consolidation. *Journal of Applied Physics*, 12, 155–164.
25. Edwards MG, Rogers C (1998) Finite volume discretization with imposed flux continuity for the general tensor pressure equation. *Computers & Geosciences*, 2(4), 259–290.
26. Schöberl J (1997) NETGEN An advancing front 2D/3D-mesh generator based on abstract rules. *Computing and Visualization in Science*, 1(1), 41-52.
27. Fetter CW (1994) *Applied Hydrogeology*, third ed. Prentice Hall, New Jersey.
28. Bedient PB, Rifai HS, Newell CJ (1994). *Ground water contamination: transport and remediation*. Prentice-Hall International, Inc.



© 2018 by the authors. Licensee SCU, Ahvaz, Iran. This article is an open access article distributed under the terms and conditions of the Creative Commons Attribution 4.0 International (CC BY 4.0 license) (<http://creativecommons.org/licenses/by/4.0/>).





## **Development of A new Hydraulic Relationship for Submerged Slide Gates**

Sasan Jahan Kohan<sup>1</sup>  
Hossien M. V. Samani<sup>2</sup>  
Hossein Ebrahimi<sup>3</sup>

### **Abstract**

Slide gates are one of the most common gates used in hydraulic structures. These gates are often in practice hydraulically submerged. The usual method to determine the flow passes through the gate is solving simultaneously the energy and the momentum nonlinear equations by a numerical method. In this manuscript, a large number of various cases of gate sizes and flows are considered and solved numerically by using these two equations to obtain a database. This database is converted to dimensionless groups and then a direct relationship is developed by using three-dimensional curve fitting. The results obtained by the developed relationship are compared with those obtained by the numerical common method. The comparison results in a good agreement which indicates that the developed relationship is accurate and simple to be used in the design of slide gates.

**Keywords:** Slide gate, Numerical method, Submerged gate, Curve fitting.

Received: 18 February 2018; Accepted: 21 September 2018

### **1. Introduction**

Slide gates are common in irrigation networks, used for controlling the flow in channels. The flow passes the gate may result in either a free or submerged hydraulic jump when interacts with the tailwater. The outflow is said to be free when the issuing jet of the supercritical flow is open to the atmosphere and is not submerged. The outflow is known as submerged, if the tailwater

---

<sup>1</sup> Water Resources Engineering Department, Faculty of Engineering, Shahre Qods Islamic Azad University, Shahr Qods, Tehran, Iran, sasangahan@gmail.com

<sup>2</sup> Water Resources Engineering Department, Faculty of Engineering, Shahre Qods Islamic Azad University, Shahr Qods, Tehran, Iran, hossein.samani@gmail.com (**Corresponding author**)

<sup>3</sup> Water Resources Engineering Department, Faculty of Engineering, Shahr Qods Islamic Azad University, Shahr Qods, Tehran, Iran, ebrahimi165@yahoo.com



depth,  $y_3$  is greater than the conjugate depth needed to form a hydraulic jump. The commonly observed case is the submerged one. Figures 1 and 2 show the free and submerged hydraulic jumps, respectively.

Henry [1] conducted experiments on free and submerged slide gates and showed the experimental results in terms of the gate flow coefficient,  $C_d$  as a function of  $\frac{y_1}{y_G}$  and  $\frac{y_3}{y_G}$ . Rao

and Rajaratnam [2] also showed a good accord between theory and experiment for the case of submerged flow from a culvert which is similar to the case of the submerged flow from the slide gate.

Rajaratnam and Subramaniya [3] have developed the following equation for gates in which free hydraulic jumps occur:

$$Q = C_d b y_G \sqrt{2 g y_1} \quad (1)$$

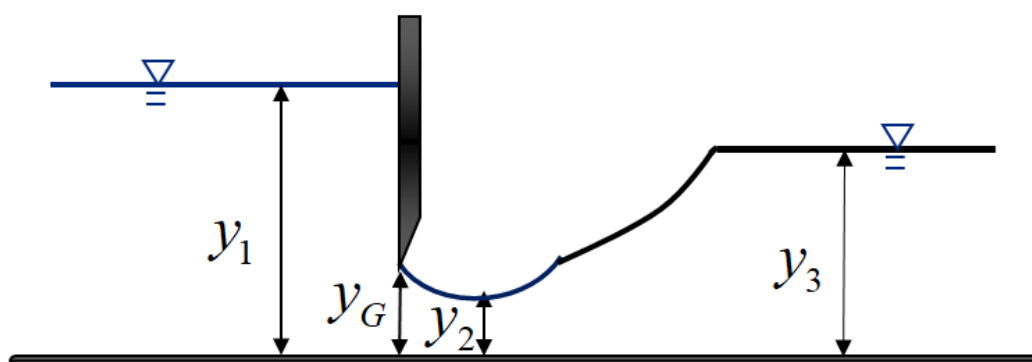


Figure 1. Free hydraulic jump in a slide gate

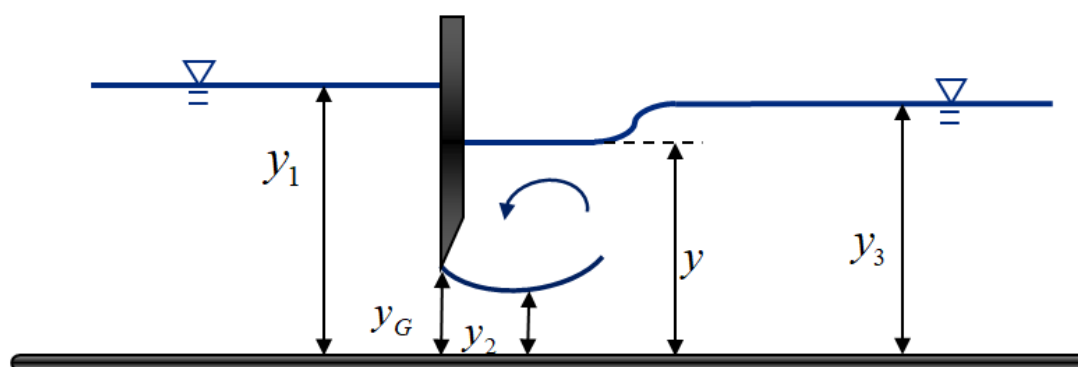


Figure 2. Submerged hydraulic jump in a slide gate

In which  $Q$  is the flow discharge passes through the gate,  $C_d$  is the gate flow coefficient,  $b$  is the gate width,  $y_G$  is the gate opening,  $y_1$  is the flow depth upstream the gate,  $y_2$  is the contracted jet depth going out the gate opening,  $y$  is the water depth just behind the gate, and  $y_3$  is the tailwater depth. Rajaratnam [4] proved that the gate flow coefficient is a function of  $y_G/y_1$ . Garbrecht [5] developed Equation (2) for the gate flow coefficient,  $C_d$ . Henry [1]



proved that  $C_d$  has the form shown in Equation (3). Swamee [6] obtained Equation (4) for the coefficient  $C_d$ .

$$C_d = 0.6468 - 0.1641 \sqrt{\frac{y_G}{y_1}} \quad (1)$$

$$C_d = \frac{0.6108}{\sqrt{1 + 0.6108 \frac{y_G}{y_1}}} \quad (2)$$

$$C_d = 0.611 \left( \frac{y_1 - y_G}{y_1 + 0.15y_G} \right)^{0.072} \quad (3)$$

Swamee [7] in his research has shown that the flow coefficient in submerged gates depends on the tailwater depth in addition to the gate opening and the flow depth upstream of the gate. Ferro [8] and Negam et al., [9] et al. studied the case of the simultaneous flow over and under the gate. Negam [10] developed equations to determine the combined flow over a weir and under the gate.

No direct explicit equation has been developed to calculate the flow through submerged gates. In this research, a new direct explicit relationship to calculate the flow in terms of the gate dimensions, upstream flow depth, gate opening, tailwater depth is developed.

## 2. Materials and methods

### 2.1. Traditional common method

The flow discharges pass through the gate can be found by the traditional common method in which the energy equation between upstream and cross section 2 and the momentum equation between this cross-section and the tailwater depicted in Figure 2 are solved simultaneously. The energy and momentum equations are given in Equations (5) and (6), respectively:

$$y_1 + \frac{Q^2}{2g(by_1)^2} = y + \frac{Q^2}{2g(by_2)^2} \quad (5)$$

in which  $y_2 = 0.61y_G$

$$\frac{y}{2}(by) + \frac{Q^2}{g(by_2)} = \frac{y_3(by_3)}{2} + \frac{Q^2}{g(by_3)} \quad (6)$$

The nonlinear Equations (5) and (6) are solved by using the solver in Excel program to obtain the unknowns  $Q$  and  $y$ .

A large number of cases of submerged gates including various gate dimensions, upstream flow depths, gate openings, and tailwater depths are regarded and solved as indicated above to produce a database covering almost all possible cases in practice. The produced database covers the followings:

$$Q = 0.05 - 100 \text{ m}^3/\text{s}$$

$$y_1 = 0.05 - 10 \text{ m}$$

$$y_3 = 0.04 - 9.7 \text{ m}$$

$$b = 0.5 - 10 \text{ m}$$

Some of the results by the above-explained traditional method are given in Table 1.

**Table 1. Some of the results obtained by the traditional method for submerged gates**

$y_2$ (m)	$y$ (m)	$Q$ (m <sup>3</sup> /s)	$y_3$ (m)	$y_G$ (m)	$b$ (m)	$y_1$ (m)
0.3465	0.654	1.3	0.75	0.568	2	0.8
0.1904	0.66	0.5	0.8	0.312	1	1
0.2749	0.495	0.9	0.8	0.451	1	1
0.2397	0.59	1.4	0.8	0.393	2	1
0.2465	0.576	2.2	0.8	0.404	3	1
0.3093	0.786	2	0.9	0.507	3	1
0.2593	0.548	4	0.8	0.425	5	1
0.19	0.66	3	0.8	0.312	6	1
0.1252	0.549	1.5	0.7	0.205	4	1
0.2496	0.569	3	0.8	0.409	4	1
0.2323	0.603	4	0.8	0.381	6	1
0.2652	0.532	5	0.8	0.435	6	1
0.353	0.896	5	1.2	0.579	4	1.5
0.6544	1.205	7	1.4	1.073	4	1.5
0.3068	1.168	3.2	1.3	0.503	4	1.5

## 2.2 The developed equation using non-linear optimization

The involved variables in the problem are converted to dimensionless groups by using dimensional analysis. The resulted dimensionless groups are as follows:

$$\frac{y_G}{y_1}, \frac{y_3}{y_1}, \text{ and } \frac{Q^2 b}{g(b y_G)^3}$$

$\frac{Q^2 b}{g(b y_G)^3}$  is considered as a function of  $\frac{y_G}{y_1}$  and  $\frac{y_3}{y_1}$ . Many types of functions with unknown coefficients are regarded and by using the Generalized Reduced Gradient (GRG) nonlinear optimization method, the function which results in the best fit in which the summation of the squares of the differences between the obtained function and the given points is minimized. The type of the function which results in the maximum correlation coefficient was as given in the following:

$$\frac{Q^2 B}{g(b y_G)^3} = \left[ -10.4 + 2.31 \ln\left(\frac{y_3}{y_1}\right) + \frac{11.37}{\left(\frac{y_G}{y_1}\right)} - 10.25 \left( \ln\left(\frac{y_3}{y_1}\right) \right)^2 - \frac{11.03}{\left(\frac{y_G}{y_1}\right)^2} - 21.16 \frac{\ln\left(\frac{y_3}{y_1}\right)}{\left(\frac{y_G}{y_1}\right)} - 0.184 \left( \ln\left(\frac{y_3}{y_1}\right) \right)^3 + \frac{9.81}{\left(\frac{y_G}{y_1}\right)^3} + 17.92 \frac{\ln\left(\frac{y_3}{y_1}\right)}{\left(\frac{y_G}{y_1}\right)^2} + 9.51 \frac{\left( \ln\left(\frac{y_3}{y_1}\right) \right)^2}{\left(\frac{y_G}{y_1}\right)} \right] \quad (7)$$

The correlation coefficient,  $r^2$ , of the function given in Equation (7) is equal to 0.9997 which indicates that the developed equation is accurate enough to be used for the design of the

submerged slide gates.

### 3. Results and conclusions

The results of the developed relationship given in Equation (7) are compared with those obtained by the traditional method in which the energy and momentum equation are solved simultaneously in Table 2 for a wide range of gate dimensions and hydraulic conditions.

**Table 2. Comparison of the discharges obtained by the traditional method and Equation (7)**

$y_1(m)$	$b(m)$	$y_G(m)$	$y_3(m)$	$Q$ by traditional method( $m^3/s$ )	$Q$ by Equation (7)( $m^3/s$ )
0.5	0.5	0.333949	0.45	0.18	0.1909
0.7	0.5	0.398951	0.6	0.3	0.3026
0.9	0.5	0.564419	0.8	0.45	0.4425
1	0.5	0.427442	0.8	0.4	0.4035
0.5	1	0.188622	0.45	0.15	0.1564
0.8	1	0.46586	0.7	0.7	0.7047
0.8	2	0.568098	0.75	1.3	1.2968
1	1	0.450588	0.8	0.9	0.8782
1	2	0.392881	0.8	1.4	1.414
1	3	0.507066	0.9	2	2.0721
1	6	0.311538	0.8	3	3.0127
1	4	0.205164	0.7	1.5	1.4997
1.5	4	0.578758	1.2	5	5.0528
1.5	5	0.951711	1.4	7	7.2311
2	1	0.703618	1.5	2	1.9761
2	2	0.703664	1.5	4	3.9525
2	4	0.584516	1.5	6	6.0158
2	6	0.935148	1.8	10	10.332
3	2	0.699138	2	5	4.9815
3	3	0.781972	2	9	8.7515
3	5	0.701072	2.8	5	5.0091
3	7	1.006286	2.5	18	18.125
6	3	1.070964	5	10	9.9219
9	3	0.810219	7	10	10.043
3	9	1.768514	2.7	40	41.119
2	7	1.097926	1.8	15	15.514
2	9	0.958327	1.7	20	20.413
5	9	0.478252	2.7	20	20.028
4	2	1.12689	3.2	7	6.9948
4	4	0.713533	3.2	8	7.9459
4	8	0.91582	3.3	20	19.828
4.5	9	0.710958	3	25	25.018
2.5	9	0.3401	2.2	5	5.0064
5	7	0.529525	3.8	12	12.041
5	9	1.30796	4	40	39.867
2.5	10	0.867646	2.1	20	20.181
4.5	10	1.027884	3.7	30	29.752
5	4	1.916133	4.3	24	24.384
5	10	0.905594	3.9	30	29.803
6	10	0.805722	4.5	30	29.977
6.5	10	0.452357	3.1	25	24.763
4.5	10	0.395901	2	20	20.061
10	4	1.052254	5	30	30.156
3	10	0.593473	2	20	20.013
2.5	10	0.618378	1.7	20	19.931

3	10	0.657484	2.5	15	14.858
7	3	0.716452	5.4	8	8.029
7	6	1.054521	5.7	22	21.913
7	7	0.371009	5.8	8	7.9331
8	7	2.143786	7	50	49.674
8	8	1.689877	7.5	30	30.013
9	8	1.900035	7	70	69.517
9	9	0.841116	7.7	25	25.168
8	4	3.419684	7.4	40	41.392
9	10	2.529361	8	85	84.564
10	8	1.028664	6	50	50.082
5	10	1.099075	4.6	22	21.911
7	10	1.808016	6	60	59.577
8	10	2.110436	7	70	69.566
10	6	1.121588	7	35	35.067
10	10	1.80164	8	80	79.425
10	10	3.411529	9.3	100	101.46

Referring to Table 2, the results of the comparison show that the discharges calculated by the traditional method and proposed method (Equation (7)) are very close to each other. The developed equation is an explicit equation which can be used directly to calculate the flow discharge through submerged slide gates in a much easier manner compared to the traditional method in which two nonlinear equations must be solved simultaneously. Hence, the developed equation can be used in the design of submerged slide gates directly due to its simplicity and high accuracy.

## References

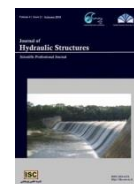
1. Henry, H. R. (1950). Discussion on "Diffusion of submerged jets," by Albertson, M. L. et al., Trans. Am. Society Civil Engrs., 115, 687.
2. Rao, G., Rajaratnam, N. (1963). "The submerged hydraulic jump," Proc. Am. Soc. Civil Engineers, 89(1), 139.
3. Rajaratnam, N. and Subramaniya, K. (1967). "Flow equation for sluice gates. J. Irrig. Drainage Eng., ASCE, 93:167-186.
4. Rajaratnam, N. (1977). "Free flow immediately below sluice gates," J. Hydraul. Eng. ASCE, 103(3): 345-351.
5. Garbrecht, G. (1977). "Discussion of discharge computation at river control structures." J. Hydr. Div., 104(12), 1481-1484.
6. Swamee, P. K. (1992). "Sluice gate discharge equations," J. Irrig. Drainage. Eng., 118: 57-60.
7. Swamee, P. K. (1988). "Generalized rectangular weirs equations," J. Hydraul. Eng., ASCE 114: 945-949.
8. Ferro, V. (2000). "Simultaneous flow over and under the gate," J. Irrig. and Drainage Eng., ASCE, 126(3): 190-193.
9. Negam, A. M., A. A. El-Saiad and O. K. Saleh (1997). "Characteristics of combined flow over weirs and below submerged gates," Proc. of Al-Mansoura Eng., 2 and Intl. Conf., (MEIC' 97), Egypt.

10. Negam, A. M. (2002). "Combined free flow over the weir and below Gates," J. Hydraul. Res., IAHR, 40(3): 359-365.



© 2018 by the authors. Licensee SCU, Ahvaz, Iran. This article is an open access article distributed under the terms and conditions of the Creative Commons Attribution 4.0 International (CC BY 4.0 license) (<http://creativecommons.org/licenses/by/4.0/>).





## Effect of rice husk ash on the swelling pressure of bentonite soil stabilized with lime in the presence or lack of sulfate

Mohammad Siros Pakbaz<sup>1</sup>  
Saber Seyedalizadeh Ganji<sup>2</sup>

### Abstract

Lime is an effective substance to decrease the swelling of expansive soils. The effective use of lime as a stabilizing agent in the presence of sulfate under some circumstances has been questioned due to the formation of ettringite. In this research, the effect of the addition of rice husk ash (RHA) on the swelling pressure of a bentonite soil (B) modified with lime (L) and calcium sulfate or gypsum (G) was investigated. Nine groups of twin compacted samples, namely, bentonite soil (B), B + L (3% by dry weight), B+3%L+ 5%G, B+3%L+RHA (5, 10 and 15% by dry weight, respectively) and B+3%L+5%G+RHA (5,10 and 15%, respectively), were prepared and tested immediately for 1-D constant volume swelling pressure measurements. Similar groups of samples were prepared and tested after 7 and 28 days of curing. The results indicated the effect of RHA in decreasing the magnitude of swelling pressure in comparison with untreated and treated soil without RHA.

**Keywords:** Rice husk, Lime, Sulfate, Expansive soil, Swelling pressure.

Received: 01 July 2018; Accepted: 21 September 2018

### 1. Introduction

The stabilization of expansive clay soils with cementitious materials such as ordinary Portland cement and lime has been practiced over the past six decades (e.g. [1-8]). The decrease in swelling potential of treated soils with lime is due to the flocculation of soil particles as a result of exchanging  $\text{Ca}^{2+}$  cations with other cations present on the surface of the clay minerals, which causes a reduction in tendency for double layer expansion. The second reason for the decrease in swelling potential upon blending lime or cement with expansive soils is due to pozzolanic reactions that occur with time between silicates and aluminates that are detached from the surface of clay minerals and calcium ions present in the solution. The silicates and aluminates are dissociated from the clay mineral surfaces when under alkaline conditions

<sup>1</sup> Department of Civil engineering. Faculty of Engineering, Shahid Chamran University of Ahvaz , Iran, Pakbaz\_m@scu.ac.ir (**Corresponding author**)

<sup>2</sup> Department of Civil engineering. Faculty of Engineering, Shahid Chamran University of Ahvaz , Iran, saberganji@gmail.com

(pH>12) in the presence of lime or cement in excess of 3% of the soil dry weight [9].

Occasionally, the use of lime or cement for treating expansive soils rich in sulfate-bearing minerals has caused more expansion. This expansion is due to the formation and subsequent hydration of minerals ettringite and / or thaumasite. The  $\text{Ca}^{2+}$  ions in the calcium-based stabilizers participate with alumina released from clay minerals and with sulfate in the presence of water to form ettringite and/or thaumasite [10-17]. Pakbaz and Keshani [18] showed that the presence of 5 to 10% of gypsum caused the initial generation of higher magnitudes of swelling pressure compared with those of untreated bentonite soil and bentonite soil treated with 3% of lime.

In several countries such as Iran, India, and Thailand, there are many agricultural waste materials produced, such as rice husk (RH) that are mostly dumped or used as fuel. Rice husk is produced during the milling process of rice and consists approximately 22% of the weight of the rice (Rice Market Monitor, FAO) [19]. The production of RH amounts to approximately 742 million tons annually (<http://www.ricehuskash.com>). The RH that remains after burning at  $650^{\circ}\text{C}$  consists mainly of silica dioxide ( $\text{SiO}_2$ ), which is very reactive with lime (e.g. [20-22]). The reactivity of RHA toward lime is strongly dependent on the temperature at which the ash is produced [23]. They have shown that RHA is most reactive with lime when burned at  $500^{\circ}\text{C}$ . They also indicated that RHA free from cationic impurities showed a higher reactivity. In fact, Real et al. [24] showed that when RH was leached with HCl before burning at  $600^{\circ}\text{C}$ , the remaining ash was approximately 260 times finer than when it was not leached. The authors also indicated that the leaching of RH before burning produces the remaining ash that is free from cationic impurities, which make the RHA coarser when they are present.

Muntohar and Hantoro [22] showed that increases in the plastic and liquid limits of the expansive soil modified with lime increases the RHA content, whereas a decrease in the liquid limit and an increase in the plastic limit occurred when RHA was added to natural soil. The reason for the increase in limit values may be due to the porous nature of the RHA particles, as reported by Viet-Thin-An [25]. Muntohar and Hantoro [22] also showed a decrease in the swelling pressure of soil stabilized with lime with the addition of RHA.

The practical application of the magnitude and time rate of the swelling pressure for clay shale was addressed by Mesri et al. [26]. The effect of lime on the swelling pressure of an expansive bentonite soil in the presence of sulfate has been studied by Pakbaz and Keshani [18]. The effect of RHA as a pozzolan has not been tested in the presence of lime and sulfate together before in expansive clays. In this research, the effect of RHA on the swelling pressure of lime-treated bentonite soil in the presence of sulfate is studied. Three different percentages of RHA together with lime and gypsum are mixed with bentonite soil to investigate the effect of RHA.

## 2. Materials and methods

### 2.1. Bentonite soil

Bentonite used in this research was supplied from Kashan Doreen factory in Iran. For better mixing, bentonite was first passed through a No. 40 US sieve before it was tested according to the ASTM D4318-10e1 [27] procedure for determining the Atterberg Liquid and Plastic Limits, which were measured to be 179% and 36%, respectively. The chemical compositions of bentonite are summarized in Table 1.

**Table 1 Bentonite chemical composition**

Compound	$\text{SiO}_2$	$\text{Al}_2\text{O}_3$	$\text{Fe}_2\text{O}_3$	$\text{K}_2\text{O}$	$\text{CaO}$	$\text{MgO}$	$\text{SO}_3$	$\text{P}_2\text{O}_5$	$\text{TiO}_2$	L.O.I
%	60.26	10.8	2.45	0.84	1.23	1.32	0.46	0.1<	0.17	2.2



## 2.2. Lime

The lime used in this research was industrial hydrated lime. The chemical compositions of lime is shown in Table 2. The lime was passed through a No. 200 US sieve before mixing with the soil.

**Table 2 Lime chemical composition**

Compound	$C_a(OH)_2$	MgO	L.O.I
%	93.27	0.81	5.92

## 2.3. Gypsum (calcium sulfate)

The gypsum used in this research was obtained from Semnan gypsum factory located at Semnan industrial city in north east Iran. This material has the lowest solubility but is the most common sulfate present in most natural soils. The chemical composition of gypsum is shown in Table 3.

**Table 3. Gypsum chemical composition**

Compound	$SiO_2$	$Al_2O_3$	$Fe_2O_3$	CaO	MgO	$SO_3$	L.O.I
%	0.7	0.26	0.11	38.55	0.26	55.68	4.44

## 2.4. Rice husk ash (RHA)

In this research, the rice husk was obtained directly from rice farms located in Mazandaran Province in northern Iran. The rice husk was burned in two stages before mixing with soil. In the first stage, it was burned in the open space for approximately 40 min. Then, to burn the remaining carbon from the ashes, the remaining ashes were collected and placed in an electric kiln at a temperature of 650°C and maintained for 90 min. The grain size distribution of RHA after the burning process showed that most of the RHA particles remained on the No. 200 US sieve ( $d_{85}=0.35\text{mm}$ ;  $d_{50}=0.15\text{mm}$  and  $d_{15}=0.074\text{mm}$ ). The initial preliminary tests to examine the effect of RHA size on reactivity during hydration and pozzolanic reactions showed that the RHA particles that were ball milled and passed through the No. 200 US sieve before mixing with soil were more effective in decreasing the swelling pressure of bentonite than those particles that remained on the No. 200 US sieve. Therefore, it was decided that for all tests, the above procedure for the preparation of RHA particles before mixing was to be followed. However, it is recognized that ball milling of RHA may not be economical for field applications. Pre-leaching of RH before burning at a burning temperature of approximately 500°C may be an appropriate method for obtaining RHA with a much higher surface area [23,24]. The chemical compositions of RHA is shown in Table 4.

**Table 4. Rice husk ash Chemical composition**

Compound	$SiO_2$	La&Lu	MnO	$P_2O_5$	$SO_3$	MgO	CaO	$K_2O$	$Fe_2O_3$	$Al_2O_3$	L.O.I
%	83.0	>1	0.17	5.6	0.34	2.0	1.5	3.8	2.0	0.27	1.28

## 2.5. Preparation of samples

To compare the results of the swelling pressure tests and to observe the effect of RHA on different samples, several series of samples were prepared according to the following procedure. All samples were mixed and compacted at the respective optimum water content to maximum dry density according to the standard proctor compaction procedure. For each series of samples, three groups of samples were prepared. One group was measured for swelling pressure immediately after the mixing process. The other two groups were tested after 7 and 28 days of curing. After compaction, the latter group of samples was wrapped in plastic bags and maintained at room temperature under 100% humidity for the required curing period. A total of 9 series of samples, namely, B, B+3%L, B+3%L+5%G, B+3%L+(5,10, and 15%)RHA, and B+3%L+5%G+(5,10, and 15%)RHA was tested without curing and a total of 16 series of samples was tested after 7 and 28 days of curing. In each group, 2 similar samples were tested, and the average results were reported.

The cured and uncured compacted samples were trimmed into consolidation rigid rings that were 70 mm in diameter and 20 mm in height before placing in an oedometer and mounting the samples in a consolidation front loading device for constant volume swelling pressure testing. The constant volume swelling pressure tests were performed according to the ASTM D4546-96 standard [28]. According to this standard, the purpose is to find the pressure needed to apply to the sample in order to maintain the original height of sample after inundation.

## 3. Results and discussions

### 3.1. Effect of RHA on the compaction curves

Figures 1 and 2 show the effect of RHA on the compaction curves of treated bentonite with lime and lime + gypsum. In general, RHA caused a decrease in the maximum dry density and an increase in optimum water content of treated bentonite samples. The decrease in maximum dry density was approximately 4-9% that may be due to the reduced specific gravity of the RHA particles compared with that of the treated bentonite. The increase in the optimum water content was approximately 25-36%, which may be due to the porous nature of the RHA particles, as mentioned earlier.

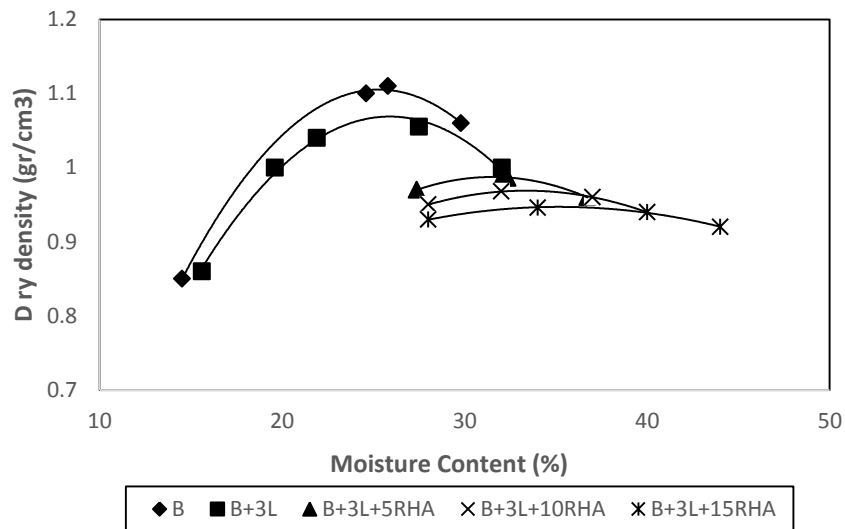


Figure 1. Effect of the RHA on compaction curve of soil stabilized with lime

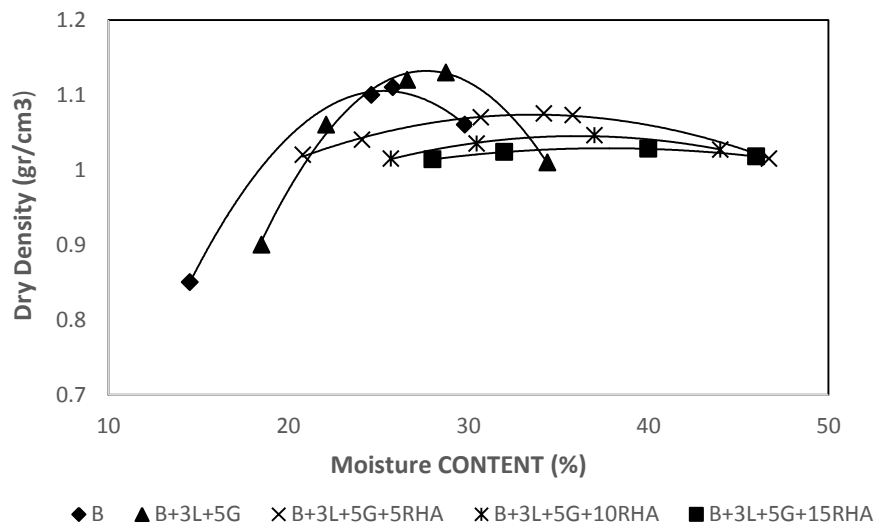
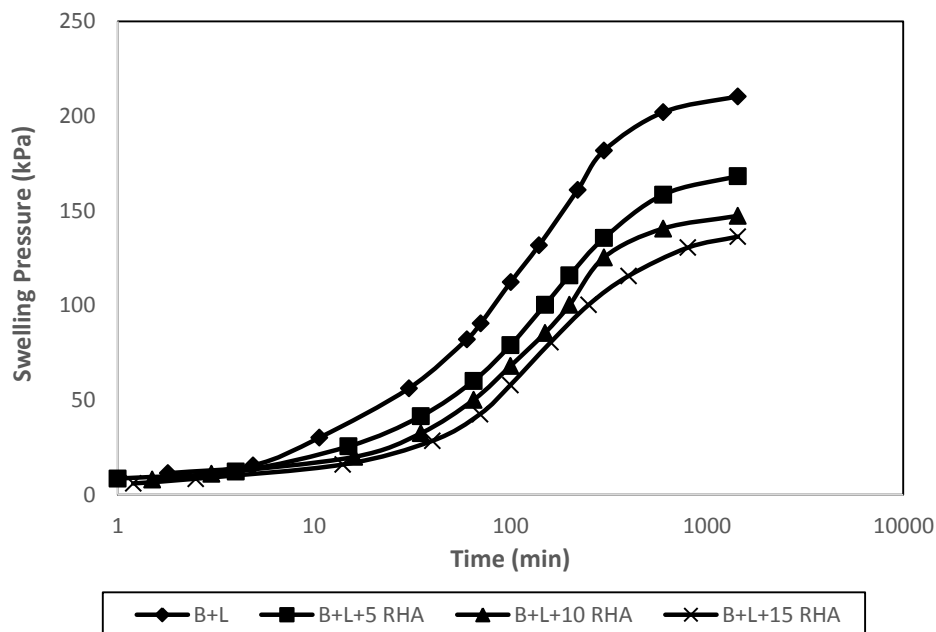


Figure 2. Effect of RHA on compaction curve of the soil stabilized with lime in the presence of sulfate

### 3.2. Effect of rice husk ash on the swelling pressure of B+3%L

Figure 3 shows the effect of RHA on the swelling pressure of lime-treated bentonite soil tested immediately after mixing and compaction with no curing period. The swelling pressure decreased with an increasing amount of RHA from 210 kPa to 168, 147 and 136 kPa for 5, 10 and 15% RHA, respectively (Table 5). These results mean that the addition of RHA has caused an approximately 20 to 35% decrease in the swelling pressure of lime-treated bentonite soil. This decrease in swelling pressure with no curing period is due to the increase in void ratios (higher optimum water content and lower maximum dry density) caused by the presence of RHA in

samples as well as to a reduced tendency for double layer expansion as the result of the addition of RHA.



**Figure 3. The effect of RHA on swelling pressure of soil stabilized with lime measured immediately after mixing**

Figure 4 shows the effect of RHA on the swelling pressure of lime-treated bentonite soil after a 7-day curing period. The swelling pressure of lime-treated bentonite soil after 7 days of curing was 150 kPa, which decreased to 100, 82 and 51 kPa for RHA contents of 5, 10, and 15%, respectively (Table 5); a decrease of approximately 33 – 66%. This decrease in swelling pressure of lime-treated bentonite soil was due to the additional cementing effect of chemical products of pozzolanic reactions that occurred between lime and RHA.

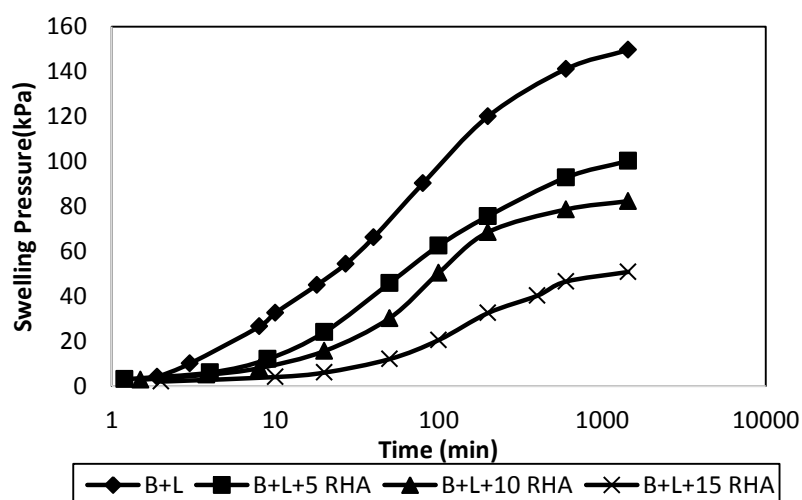


**Figure 4. The effect of RHA on swelling pressure of soil stabilized with lime after 7 days of curing .**

Fig. 5 shows the effect of the curing period on the swelling pressure of B+3%L+ 15%RHA

samples. A decrease of 63-82% for curing periods of 7 and 28 days was observed compared to samples with no curing period (see also Table 5).

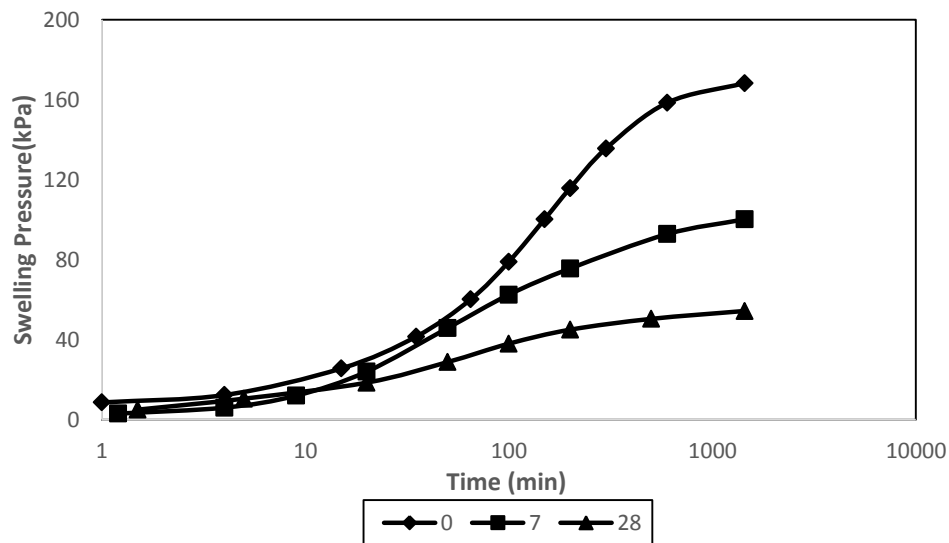


Figure 5. Effect of curing time on swelling pressure of soil stabilized with 3% of lime and 15% of RHA

Table 5 summary of final swelling pressures measured (in kPa)

Samples	Uncured	7days Curing	28days Curing
B pure	367	-	-
B + 3% L	210	149	91
B + 3% L + 5% RHA	168	100	54
B + 3% L + 10% RHA	147	82	40
B + 3% L + 15% RHA	136	51	25
B + 3% L + 5% G	267	124	39
B + 3% L + 5% G + 5%RHA	200	74	30
B + 3% L + 5% G + 10%RHA	183	66	18
B + 3% L + 5% G + 15%RHA	166	57	11

### 3.3. EFFECT OF RHA ON THE SWELLING PRESSURE OF B+3%L+5%G

Fig. 6 shows the swelling pressures of B+3%L+5%G without and with RHA at different contents with no curing period. The results indicate that the sample of B+3%L+5%G with no RHA showed a higher swelling pressure than that of sample B+3%L. The higher swelling pressure may be due to the formation of ettringite. However, the addition of RHA to this group of samples caused a decrease in the swelling pressure. The swelling pressures for this group of samples were measured to be 200, 183 and 166 kPa for RHA contents of 5, 10 and 15%, respectively, (see also Table 5) which means a decrease of 25 – 37% compared with the samples with no RHA. The decrease in the swelling pressure in this case may be due to a higher water content and void ratio for these samples as well as a lower tendency for an expansion of the double layer as a result of the presence of RHA. When the values of the swelling pressure for the B+3%L+5%G+RHA samples with no curing are compared with those for the samples of B+3%L+RHA (see Table 5), the effect of both ettringite formation and a reduced void ratio for the former samples may be responsible for the higher values of the former group. According to

Table 5, curing periods of 7 and 28 days caused further decrease in swelling pressure of approximately 40 to 72% for these samples compared with those of the samples without RHA. In this case, a further decrease in the swelling pressure with curing may be due to the cementing effect of additional chemical products generated as a result of pozzolanic reactions that have occurred between the RHA and lime.

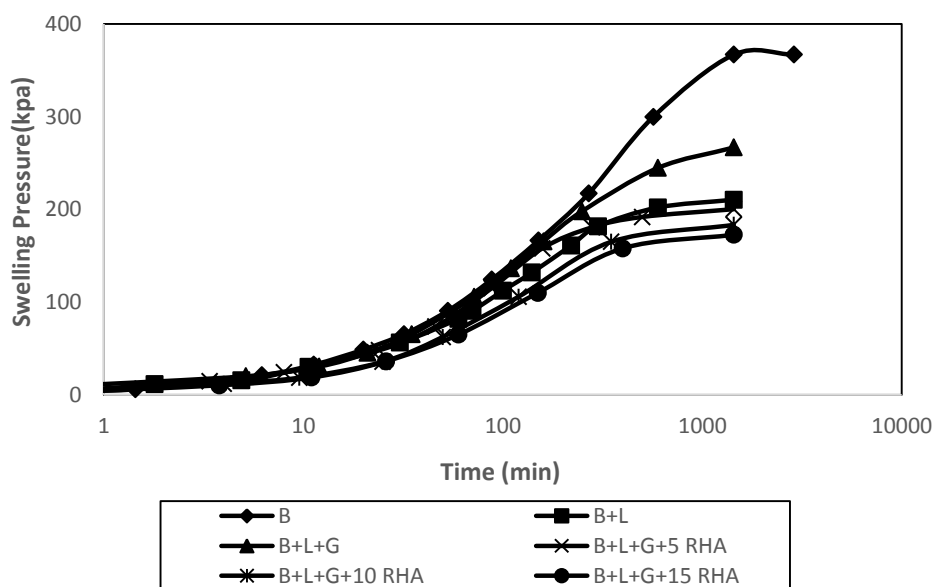


Figure 6. Effect of RHA on swelling pressure of lime treated soil in the presence of sulfate with no curing

#### 4. Conclusions

The following conclusions are reached with regard to soil index properties, compaction characteristics and value of constant volume swelling pressure after examinations of different groups of bentonite soil mixtures with 3% of lime + 5% of gypsum and 5, 10 and 15% of rice husk ash.

1. The addition of RHA to soil stabilized with lime lowered the maximum dry density and increased the optimum moisture content.
2. The addition of gypsum to soil stabilized with lime increased the maximum dry density and decreased the optimum moisture content. The addition and increasing the amount of RHA to the stabilized soil with lime and gypsum decreased the maximum dry density and increased the optimum moisture content.
3. The rice husk ash particles that passed through the No. 200 US sieve were more effective in reducing swelling pressure of bentonite than those remaining on the No. 200 US sieve. A more economical procedure for reducing the size of RHA is preleaching with acid before the burning process.
4. Rice husk ash is a suitable additive to reduce the swelling pressure. The addition of RHA to stabilized soil with lime decreased the swelling pressure. The optimal

amount for stabilized soil with lime and RHA is to add 15% RHA during 7 days of curing.

5. Rice husk ash is a suitable additive to lower the detrimental effect of sulfate presence in lime-treated expansive soil.

## References

1. Slater, D. E. (1983). "Potential Expansive Soils in Arabian Peninsula", *Journal of Geotechnical Engineering*, Vol. 109, 5, 744-746.
2. Day, R. W. (1992). "Swell Versus Saturation for Compacted Clay", *Journal of Geotechnical Engineering*, Vol. 118, No. 8, 1272-1278.
3. Osinubi, K. J. (2006). "Influence of Compactive Efforts on Lime-Slag Treated Tropical Black, Clay", *Journal of Materials in Civil Engr.* Vol. 18, No. 2, 175-181.
4. Bin, S.; Zhibin, L.; Yi, C.; and Xiaoping, Z. (2007). "Micropore Structure of Aggregates in Treated Soils", *Journal of Material in Civil Engr.* Vol. 19, No. 1, 99-104.
5. Peethamparan, S. and Olek, J. (2008). "Study of the Effectiveness of Cement kiln Dust in Stabilizing Na-Montmorillonite Clay", *Journal of Materials in Civil Engr.* Vol. 20, No. 2, 137-146.
6. Madhyannapu, R. S. and Puppala A. J. (2014). "Design and Construction Guidelines for Deep Soil Mixing to Stabilize Expansive Soil", *Journal of Geotechnical and Geoenviron. Engr.*, Vol. 140, No. 9.
7. Elkady, T. Y.; Al-Mahbashi, A. M.; and Al-Refea, T. O. (2015). "Stress Dependent Soil-Water Characteristic Curves of Lime – Treated Expansive Clay", *Journal of Materials in Civil Engr.* Vol. 27, No. 3.
8. Thyagaraj, T.; Thomas, S. R.; and Das, A. P. (2017). "Physico – Chemical Effect on Shrinkage Behavior of Compacted Expansive Clay." *International Journal of Geomechanics*, Vol. 17, No. 2.
9. Mitchell, J. K. (1981). "Soil Improvement State of the Art report". *Proc. 10th int. conf. on Soil Mechanics and Foundation Engr.* 4, 509-565.
10. Mitchell, J. K. (1986). "Practical Problems from Surprising Soil Behavior." *J. of Geotech. Geoenviron. Engng. Division*, 112 (3): 259-289.
11. Mitchell, J. K., Dermatas, D. (1992). "Clay Soil Heave Caused by Lime-Sulfate Reactions". *ASTM STP 1135: Innovations and Uses for Lime*, Philadelphia, 1992.
12. Petry, T. M., and Little, D. N. (1992). "Update on Sulfate-Induced Heave in Treated Clays: Problematic Sulfate Levels". In *Transportation Research Record 1362*, TRB, National Research Council, Washington, DC, 1992, 51.
13. Petry, T. M. (1994). "Studies of Factors Causing and Influencing Localized Heave of Lime Treated Clay Soils (Sulfate Induced Heave)". *U.S. Army Corps of Engineers, Waterways Experiment Station, Vicksburg, MS*.
14. Dermatas, D. (1995). "Ettringite-induced Swelling in Soils": *State-of-the-Art. Appl. Mech. Rev.* 48(10), 659-673.

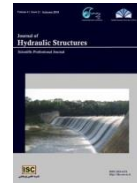


15. Puppala, A. J.; Intharasombat, N. and Vempati, R. K. (2005). "Experimental studies on Ettringite induced heaving in soils ", J. of Geotech. And Geoenviron engng, Vol. 131, Issue 3.
16. Little, D.N., Nair, S., (2009). "Recommended Practice for Stabilization for Sulfate Rich Subgrade Soils." National Highway Cooperative Research Program, Transportation Research Board of the National Academies.
17. Little, D.N.; Nair, S.; and Herbert, B. (2010). "Addressing Sulfate-Induced Heave in Lime Treated Soils." J. Geotech. Geoenviron. Eng., 2010, 136(1): 110-118.
18. Pakbaz, M.S. and Keshani, A. (2017). "Evaluation of Time rate of swelling pressure development due to the presence of sulfate in clayey soils stabilized with lime". International Journal of Geomates, Vol. 12, No. 32, 161-165.
19. Rice market monitor. FAO. <<http://www.fao.org/economic/est/publications/rice-publications/rice-market-monitor-rmm/en/>> FAO (accessed 19.05.14).
20. Mehta, P.K. (1977), "Properties of blended cements, cements made from rice husk ash," Journal of American Concrete Institute, 74, 440-442.
21. Mehta, P.K. (1979). "The chemistry and technology of cements made from rice husk ash," Proceedings UNIDO/ESCAP/RCTT Workshop on Rice-Husk Ash Cement, Peshavar, Pakistan, 113-122.
22. Muntohar , A. S. and Hantoro, G.. (2000), "Influence of Rice Husk Ash and Lime on Engineering Properties of a clayee subgrade," Mhtml:file:///A: /Rice Husk Ash and Lime.
23. James and Rao (1986). "Reactivity of Rice Husk Ash", Cement and Concrete Research, Vol. 16, 296-302.
24. Real, C.; Alcala, M. D.; and Criado, J. M. (1996). "Preparation of Silica from Rice Husks", J. Am. Ceram.Soc., 79 (8), 2012-2016.
25. Viet-Thien-An, V., Robler, C.,Danh-Dai, B. and Horst-Michael, L. (2014) , "Rice husk ash as both pozzolanic admixture and internal curing agent in ultra-high performance concrete," Cement & Concrete Composites, 53, 270–278.
26. Mesri, G., Pakbaz, M. C. and Cepeda-Diaz, A.F. (1994). "Meaning, Measurement and Field Application of Swelling Pressure of Clay Shales." Geotechnique, 44(1), 129-145.
27. ASTM. (2010). "Standard Test Methods for Liquid Limit, Plastic Limit, and Plasticity Index of Soils." ASTM D4318-10e1, West Conshohocken, PA.
28. ASTM. (1996). "Standard Test Methods for One-Dimensional Swell or Settlement Potential of Cohesive Soils." ASTM D4546-96, West Conshohocken, PA.



© 2018 by the authors. Licensee SCU, Ahvaz, Iran. This article is an open access article distributed under the terms and conditions of the Creative Commons Attribution 4.0 International (CC BY 4.0 license) (<http://creativecommons.org/licenses/by/4.0/>).





## Characteristic Based Split Finite Element for Unsteady Dam-Break Problem

Javad Parsa<sup>1</sup>

### Abstract

In this paper, an efficient numerical model for solution of the two-dimensional unsteady dam-break problem is described. The model solves the shallow water equations through Characteristic-Based Split (CBS) finite element method. The formulation of the model is based upon the fractional time step technique primarily used in the finite difference method for the incompressible Navier-Stokes equations. In addition to well-known advantages of the finite element discretization in introducing complex geometries and making accurate results near the boundaries, the CBS utilizes interesting advantages. These include the ability of the method to simulate both compressible and incompressible flows using the same formulation. Improved stability of the CBS algorithm along with its capability to simulate both sub- and super-critical flows are other main advantages of the method. These useful advantages of the algorithm introduce the CBS as a unique procedure to solve fluid dynamics problems under various conditions. Since dam-break problem has principally a high non-linear nature, the model is verified firstly by modeling one-dimensional problems of dam-break and bore formation problems. Furthermore, application of the model to a two-dimensional hypothetical dam-break problem shows the robustness and efficiency of the procedure. Despite the high non-linearity nature of the solved problems, the computational results, compared with the analytical solutions and reported results of other numerical models, indicate the favorable performance of the used procedure in modeling the dam-break problems.

**Keywords:** Characteristic-Based Split finite element, shallow water, dam-break, bore.

Received: 9 December 2018; Accepted: 25 December 2018

### 1. Introduction

The computation of unsteady flows is required for the prediction of flood waves in rivers, flows generated by failure of dams and flow conditions in the vicinity of hydraulic structures [1-3]. Numerical models have been introduced as suitable alternatives to other form of flow simulations such as experimental studies [4,5]. Indeed, numerical models have utilized as an essential predictive tool to assess the risks associated with the failure of the hydraulic structures [5,6]. In the recent

---

<sup>1</sup> Water Engineering Department, Faculty of Agriculture, University of Tabriz, Tabriz, Iran, jparsa@tabrizu.ac.ir (Corresponding author)



decades, one-dimensional numerical models have been extensively used to simulate the unsteady dam-break problem. Relatively accurate description of the dam-break problem in real situations needs to use two-dimensional models [7,8]. Accuracy of the dam-break simulation results from these models is adequate for engineering applications. Modeling of two-dimensional unsteady flow during breaking a dam is more complicated than one-dimensional one because of need for efficient solver routines and the inclusions of suitable boundary conditions. Complexity of these computations is mainly due to occurrence of both sub-critical and super-critical flows after breaking a dam.

Shallow water equations are non-linear first-order hyperbolic partial differential equations. The hyperbolic nature of these equations creates remarkable difficulties in the numerical solutions. The solutions of this type of equations obtained by numerical procedures are often discontinuous regardless of whether the initial conditions are smooth or highly fluctuating [9]. Since the equations have the non-linear character, their analytical solutions are possible in very simplified one-dimensional situations and therefore, these equations are to be solved numerically for practical problems.

Numerical experiments, however, show that most of numerical procedures fail if high non-linearity occurs in the flow field. For instance, it is well-known that simple and direct finite element forms usually fail for shallow water problems due to instability which results in severe oscillations of the solution [10]. Similar to making use of stabilizers in the finite difference context, stabilization procedures have been introduced into some finite element formulations permitting the use of the original discretization schemes. The Characteristic-Based Split, hereafter also denoted as CBS, algorithm is one of the most suitable finite element based numerical techniques for shallow water equations that utilizes the stabilization mechanism. This method utilizes both advantages of characteristics method for hyperbolic partial differential equations and nodal exact results of Galerkin weighted residual method for self-adjoint problems.

The Characteristic-Based Split algorithm and its interesting advantages are presented in detail in many earlier studies [10-22]. Here, a brief summary on the algorithm is given. The CBS algorithm is based on the original Chorin split [23] and also has similarities with the projection method widely used in compressible flow modeling. Based upon the Chorin technique, the discretization of the equations in the time advancement consists of two or more steps. The numerical behavior of the equations is affected using this splitting technique and the simpler sub-problems are achieved [14]. The velocity correction step is the key point in the CBS algorithm. The CBS algorithm makes use of Galerkin method along the characteristics for advection-dominated problems with a velocity correction stage. Using Characteristic-Galerkin procedure, the velocities are computed in two steps. Firstly, an intermediate velocity field is computed after elimination of the pressure type terms from the momentum equations. The pressure is obtained in the next step by solving the continuity equation that utilizes the intermediate velocity field determined in the previous step. A Laplacian form of the continuity equation is used making the use of Galerkin space discretization optimal. In the final step, the computed pressure type term is used to modify the velocity field. Some remarkable advantages of the algorithm for modeling of shallow water problems can be summarized as follows. Firstly, the stability of the algorithm is on the basis of the current velocity rather than the wave celerity leading to more stability of the method. Secondly, the standard Galerkin procedure is applied along the characteristics because of the splitting of the pressure type terms. The use of Characteristic-based Galerkin discretization and splitting of the pressure type terms, have made the CBS algorithm a unified approach to deal with both compressible and incompressible fluid flows and sub-critical and super-critical flows in water engineering problems, as well [16,17].

This paper presents the formulation of the Characteristic-Based Split finite element method for

the shallow water equations and its application to the simulation of the dam failure and bore formation. The Characteristic-Based Split finite element method has been never applied for dam break problem, especially for two-dimensional dam break.

The rest of the paper is structured as follows. The shallow water equations are reviewed in the first section. This is followed by the finite element formulation making use of the Characteristic-Based Split method. Numerical examples including two one-dimensional examples of a bore formation and a dam-break problem and a two-dimensional dam-break problem are discussed in the fourth section. The paper concludes with the concluding remarks in the last section.

## 2. Mathematical model

Modeling flow hydrodynamics in shallow water bodies requires the prediction of water depth and depth integrated velocities in both  $x$  and  $y$  directions. In the derivation of shallow water equations from Navier-Stokes equations, some assumptions are necessary. The constant density of fluid, hydrostatic pressure distribution and making use of suitable free surface and boundary conditions are of the assumptions required for derivation of shallow water equations [6]. A schematic figure of the basic situation is shown in Figure 1.

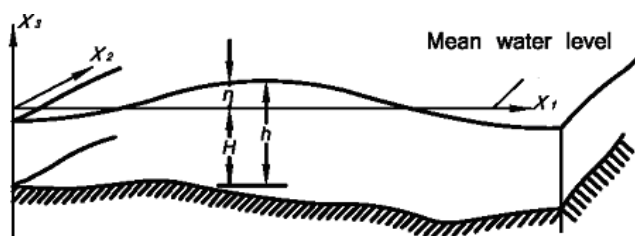


Figure 1. Schematic representation of the geometric setting.

The conservative form of the shallow water equations in Cartesian coordinate system can be written as [16,17,22]:

$$\frac{\partial h}{\partial t} + \frac{\partial U_i}{\partial x_i} = 0 \quad (1)$$

$$\frac{\partial U_i}{\partial t} + \frac{\partial F_{ij}}{\partial x_j} + \frac{\partial p}{\partial x_i} + S_i = 0 \quad (2)$$

where  $i, j = 1, 2$ , the vector of  $U$  is  $U_i = hu_i$ ,  $h$  is the water depth,  $u_i$  is the  $i^{\text{th}}$  component of the averaged velocity over the depth;  $F_{ij}$  is the  $i^{\text{th}}$  component of the  $j$  flux vector and the pressure type term  $p$  is given by:

$$p = \frac{1}{2} g (h^2 - H^2) \quad (3)$$

where  $H$  is the bathymetry elevation measured with respect to an arbitrary horizontal reference level. As shown in Figure 1, the water depth,  $h$ , is the water surface elevation with respect to the bathymetry and can be computed by  $h = H + \eta$ . The variable  $\eta$  denotes the free surface elevation in regard to an arbitrary horizontal reference level. Finally,  $S_i$  is the  $i^{\text{th}}$  component of a source vector, which can be expressed as:

$$S_i = -g(h-H)\frac{\partial H}{\partial x_i} + g\frac{n^2 u_i |u|}{h^{\frac{4}{3}}} + r_i - \tau_i \quad (4)$$

The source terms in equation (4) are obtained by depth integration. The terms in this equation include the slope of bottom, the friction of bottom (Manning formula), the force of Coriolis and wind tractions  $\tau_i$ . Here  $r_i = -f U_j$  where  $f$  denotes the Coriolis factor.

### 3. Numerical model

Using the concept of characteristics in temporal discretization of the shallow water equations, equations (1) and (2), arrived at the following equations [16]:

$$\left(\frac{1}{c^2}\right)^n \Delta p = -\Delta t \left[ \frac{\partial U_i^n}{\partial x_i} + \theta_1 \frac{\partial(\Delta U_i)}{\partial x_i} \right] \quad (5)$$

$$\Delta U_i = -\Delta t \left[ \frac{\partial F_{ij}}{\partial x_j} + S_i \right]^n + \frac{\Delta t^2}{2} \left[ u_k \frac{\partial}{\partial x_k} \left( \frac{\partial F_{ij}}{\partial x_j} + S_i \right) \right]^n - \Delta t \frac{\partial p^{n+\theta_2}}{\partial x_i} \quad (6)$$

in which:

$$\frac{\partial p^{n+\theta_2}}{\partial x_i} = (1-\theta_2) \frac{\partial p^n}{\partial x_i} + \theta_2 \frac{\partial p^{n+1}}{\partial x_i} - (1-\theta_2) \frac{\Delta t}{2} u_k \frac{\partial}{\partial x_k} \left( \frac{\partial p^n}{\partial x_i} \right) \quad (7)$$

where  $(0 \leq \theta_1, \theta_2 \leq 1)$ ,  $(k=1, 2)$ , the incremental variables  $\Delta p$  and  $\Delta U_i$  are the increments of the variables over a time step  $\Delta t$  and  $c$ , the long waves celerity, is related to  $p$  with the depth of water by:

$$c^2 = \frac{dp}{dh} = gh \quad (8)$$

The method is completed by omitting  $\Delta U_i$  in the equation (5) by computing the divergence of equation (6) and replacing the obtained equations into equation (5). The following 'self-adjoint' type equation for the variable  $p$  is resulted in:

$$\frac{1}{c^2} \frac{\Delta p}{\Delta t} - \theta_1 \theta_2 \frac{\partial}{\partial x_i} \frac{\partial(\Delta p)}{\partial x_i} = -\frac{\partial}{\partial x_i} \left( U_i^n + \theta_1 \Delta U_i^* \right) + \theta_1 \Delta t \frac{\partial}{\partial x_i} \frac{\partial p^n}{\partial x_i} \quad (9)$$

The 'intermediate' variable  $\Delta U_i^*$  computed explicitly. It denotes the first two terms in square brackets of equation (6). Calculation of the pressure type variable and the depth averaged velocity at the time  $(n+1)\Delta t$ ,  $p^{n+1}$  and  $U_i^{n+1}$ , is conducted through the following steps: first, the intermediate variable  $\Delta U_i^*$  is computed, then the incremental pressure term  $\Delta p$  is calculated and at the final step, the intermediate velocities are corrected to attain the final velocity values, i.e. the complete momentum equation (6). The equations (6), (7) and (9) are performing the time discretization along the characteristics. A backward approximate integration gives the mentioned equations with extra convection stabilizers (the second bracket terms in right-hand side of equation (6)). These stabilization terms are consistent and extirpate the oscillations due to highly convective flows [10].

### 3.1. Spatial discretization

The spatial discretization of the equations obtained during the mentioned three steps is stated here. The first two terms on the right-hand side of equation (6) are discretized using the Gauss–Green theorem and the standard Galerkin technique as follows:

$$\begin{aligned} \int_{\Omega} N_u^l \Delta U_i^* d\Omega = \Delta t \left[ - \int_{\Omega} N_u^l \frac{\partial F_{ij}}{\partial x_j} d\Omega - \int_{\Omega} N_u^l (S_i) d\Omega \right. \\ \left. - \frac{\Delta t}{2} \int_{\Omega} \frac{\partial}{\partial x_k} (N_u^l u_k) \frac{\partial F_{ij}}{\partial x_j} d\Omega + \frac{\Delta t}{2} \int_{\Omega} N_u^l u_k \frac{\partial (S_i)}{\partial x_k} d\Omega \right. \\ \left. + \frac{\Delta t}{2} \int_{\Gamma} N_u^l u_k \frac{\partial F_{ij}}{\partial x_j} n_k d\Gamma \right]^n \end{aligned} \quad (10)$$

in which  $\Omega$  denotes the solution domain bounded by  $\Gamma$ ,  $N_u^l$  and  $N_r^l$  represent the standard weighting function for U and S in node  $l$  and  $n_k$  is the  $k^{th}$  component of the outward normal vector of the boundary of computational domain. The right-hand side of equation (10) is computed at time  $t^n$ .

Making use of the wave celerity definition in equation (8), the pressure type term is computed in terms of  $h$ . The standard Galerkin technique along with the Gauss–Green theorem are applied to equation (9) and the following discretized equation results:

$$\begin{aligned} \int_{\Omega} N_h^l \Delta h d\Omega + \theta_1 \theta_2 \Delta t^2 \int_{\Omega} \frac{\partial N_h^l}{\partial x_i} \hat{c}^2 \frac{\partial (\Delta h)}{\partial x_i} d\Omega = \\ - \Delta t \int_{\Omega} N_u^l \frac{\partial U_i^n}{\partial x_j} d\Omega + \theta_1 \Delta t \int_{\Omega} \frac{\partial N_u^l}{\partial x_i} \Delta U_i^* d\Omega \\ - \theta_1 \Delta t^2 \int_{\Omega} \frac{\partial N_h^l}{\partial x_i} (c^2)^n \frac{\partial h^n}{\partial x_i} d\Omega \\ - \theta_1 \Delta t \int_{\Gamma} N_u^l \Delta U_i^* n_i d\Gamma \\ + \theta_1 \Delta t^2 \int_{\Gamma} N_h^l \left( (c^2)^n \frac{\partial h^n}{\partial x_i} + \theta_2 \hat{c}^2 \frac{\partial (\Delta h)}{\partial x_i} \right) n_i d\Gamma \end{aligned} \quad (11)$$

in which  $\hat{c}$  is the averaged wave celerity over the time step  $\Delta t$  and  $(c^2)^n$  is calculated at time  $t^n$ . The velocity field correction as the final step, is written by considering equation (6). After making use of Galerkin procedure and some appropriate manipulations of the second-order term of equation (6), its spatial discretized form becomes as:

$$\begin{aligned}
\int_{\Omega} N_u^l \Delta U_i d\Omega &= \Delta t \int_{\Omega} N_u^l \frac{\Delta U_i^*}{\Delta t} d\Omega - (1 - \theta_2) \Delta t \int_{\Omega} N_h^l (c^2)^n \frac{\partial h^n}{\partial x_i} d\Omega \\
&\quad - \theta_2 \Delta t \int_{\Omega} N_h^l (c^2)^{n+1} \frac{\partial h^{n+1}}{\partial x_i} d\Omega \\
&\quad - (1 - \theta_2) \frac{\Delta t^2}{2} \int_{\Omega} \frac{\partial N_h^l}{\partial x_k} u_k \left( (c^2)^n \frac{\partial h^n}{\partial x_i} \right) d\Omega \\
&\quad - (1 - \theta_2) \frac{\Delta t^2}{2} \int_{\Omega} N_h^l \frac{\partial u_k}{\partial x_k} \left( (c^2)^n \frac{\partial h^n}{\partial x_i} \right) d\Omega \\
&\quad + (1 - \theta_2) \frac{\Delta t^2}{2} \int_{\Gamma} N_h^l u_k \left( (c^2)^n \frac{\partial h^n}{\partial x_i} \right) d\Gamma
\end{aligned} \tag{12}$$

### 3.2. Boundary conditions

Several boundary conditions of different types and their implementations have been described in many references, e.g. [17,21,25-30]. The implementation of the boundary conditions in the methodology of CBS is similar to that in other schemes. To implement the boundary conditions in the methodology of CBS, no special conditions are imposed for the computation of the  $\Delta U_i^*$ . In equation (11) two last terms are the normal components of momentum which are computed of order  $\Delta t$ . The velocity components normal to the wall and open boundaries are defined by modifying step for these type of boundary conditions [16,17,21].

### 3.3. Final discrete form and time integration

The following steps are performed to arrive at the final form of numerical procedure [8]:

- i. *Computation of the intermediate variable*: The following spatial approximations are used in equation (10) for this step:

$$\begin{aligned}
U_i^n &= N_u^l . U_i^{l(n)} \\
\Delta U_i^* &= N_u^l . \Delta U_i^{*l} \\
h^n &= N_h^l . h^{l(n)} \\
H &= N_h^l . H^l
\end{aligned} \tag{13}$$

- ii. *Pressure computation step*: The calculation of  $h$  is carried out using equation (17) and based on the following spatial discretization:



$$\begin{aligned}
h^n &= N_h^l \cdot h^{l(n)} \\
\Delta h &= N_h^l \cdot \Delta h^l \\
U_i^n &= N_u^l \cdot U_i^{l(n)} \\
\Delta r &= N_u^l \cdot \Delta r^l
\end{aligned} \tag{14}$$

- iii. *Momentum correction step*: The correction is established by equation (12) and the following approximations are used to equation (12) to carry out the correction of the momentum of flow:

$$\begin{aligned}
h^n &= N_h^l \cdot h^{l(n)} \\
h^{n+1} &= N_h^l \cdot h^{l(n+1)} \\
\Delta U_i^n &= N_u^l \cdot \Delta U_i^l \\
\Delta U_i^* &= N_u^l \cdot \Delta U_i^{*l}
\end{aligned} \tag{15}$$

The stability of computation of  $\Delta U_i^*$  is conditional. The simplified stability criterion in one-dimensional state can be represented by  $\Delta t_{crit} \leq \varepsilon L / |u|$ , where  $L$  is the smallest dimension of element and the values of  $\varepsilon$  for consistent and lumped mass matrices are 1/3 and 1, respectively. The second and third steps of the method can be computed explicitly or semi-implicitly based on the chosen values for  $\theta_1$  and  $\theta_2$ . For the fully explicit solution ( $\theta_2 = 0$ ), the limit of stability finds equal to the explicit solutions and the procedure will be similar to the Taylor–Galerkin method [17,21]. When a semi-implicit solution is chosen ( $0.5 \leq \theta_1 \leq 1$  and  $0.5 \leq \theta_2 \leq 1$ ), the limit of stability for the defined CBS procedure is characterized by the computation of intermediate momentum.

## 4. Results and discussion

The performance of the described algorithm on shallow water problems is evaluated by some numerical experiments. To achieve this aim, the following benchmark problems are solved in this paper. In these problems, the uniform meshes which include the triangular linear elements are used.

In what follows, two set of problems are given. The first set deals with the flows in pseudo-one-dimensional situation. The second set is two-dimensional one. These problems include the formation of shock waves by advancing the solution which are good tests for demonstrating the capability of the scheme in modeling the severe natural hydraulic problems.

### 4.1. One-dimensional problems

As the first application of the described scheme, the classical Stoker test case is studied. In this case, the one-dimensional breaking of a dam over a wet bed is considered. Stoker's exact solution [29] to the one-dimensional dam break is the superimposition of up-going rarefaction and down-going shock waves connected by a middle zone with a constant depth and a constant velocity (see, e.g., [31]). To execute this test, a dam lies at the middle of a rectangular flat channel and it is assumed that the dam fails instantaneously. Because of discontinues initial

conditions and transition of flow from sub-critical to super-critical, it represents a severe test which has highlighted problems with a number of numerical schemes. The computational domain comprises of a  $100 \times 1 \text{ m}^2$ . The water is initially at rest in the reservoir and tillage and the initial water depths are:

$$h(x,0) = \begin{cases} 2 \text{ m} & \text{if } x < 50 \text{ m} \\ 1 \text{ m} & \text{if } x \geq 50 \text{ m} \end{cases} \quad (16)$$

The gravity acceleration is assumed to be  $g = 9.8 \text{ m/sec}^2$ . The discretized domain involves  $100 \times 8$  triangular linear elements having same sizes. Suddenly, the dam removed and the computation of flow over the whole domain started using  $\Delta t = 0.1 \text{ sec}$ .

The obtained results for water surface elevations and longitudinal velocities along the entire domain after collapsing the dam for 2.5 sec, 5 sec and 7.5 sec are shown in Figures 2 and 3 and they are compared favorably with analytical solution reported in [29]. As shown in these figures, the numerical results agree very well with those from analytical solutions. It is clear that the flow velocities and shock wave fronts advancing in downstream have been modeled accurately. Compared with the exact solution, overshoots occurs around the shock wave, together with an oscillation close to the rarefaction wave. The wave front clearly agree with the exact solution, and the main differences between the exact solution and the numerical results are localized just close to the discontinuities.

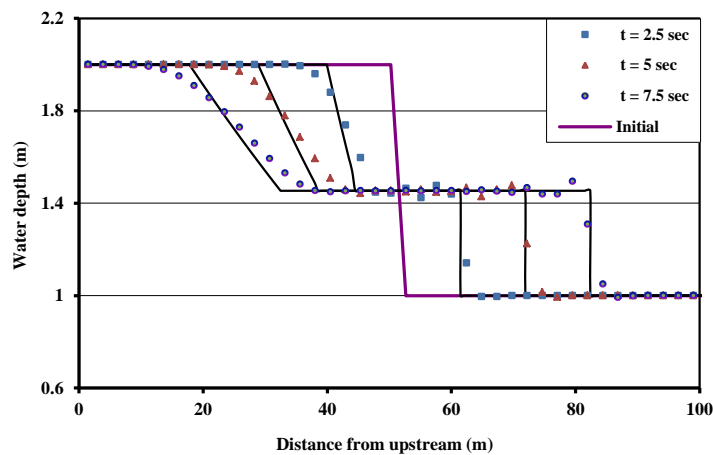
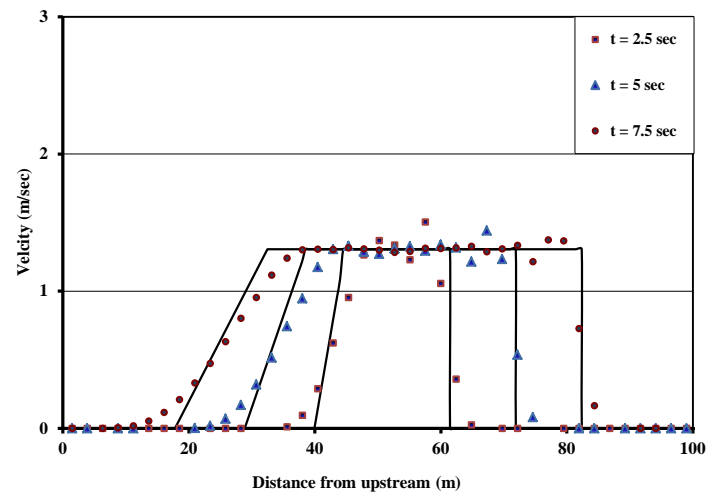


Figure 2. Comparison of the model results with the analytical solution for dam break problem.



**Figure 3. Longitudinal velocities along the entire domain compared with the analytical solution.**

The problem of bore formation and propagation along a rectangular flat channel is the second test studied here. The depth of 1 m and velocity of 1 m/sec along the entire channel are given as the initial conditions. Boundary conditions are imposed as the flow velocity of 1 m/sec in the upstream and a sinusoidal rising water elevation with period of 120 sec in the downstream boundary of the channel. After  $t = 30$  sec the total water depth is imposed as 3 m at this boundary. This situation illustrates that a bore forms and then propagates in upstream direction. In order to solve the problem, a rectangular flat channel with the length of 200 m and width of 1 m is considered. The whole domain decomposes to  $200 \times 8$  triangular elements and the model is executed using time step  $\Delta t = 0.1$  sec. The results obtained for water surface profiles and velocities during the bore propagation are shown in Figures 4 and 5. As seen, the wave fronts are well modeled and very small oscillations just occur close to the discontinuities. Comparison of the results shown in Figures 4 and 5 with those of reported in literature, e.g. [22], indicates that they have been employed coarser meshes to avoid the oscillations while the shocks were modeled milder. It is a common practice that the accurate modeling of a shock always produces some oscillations in its vicinity due to the omitting of higher order terms in the discretization process of the governing equations. In the other words, the steeper shock, the more oscillatory solution. However, the obtained results are well comparable with those of reported in [22]. The superiority of the CBS technique is its ability to model the shocks accurately with less oscillation.

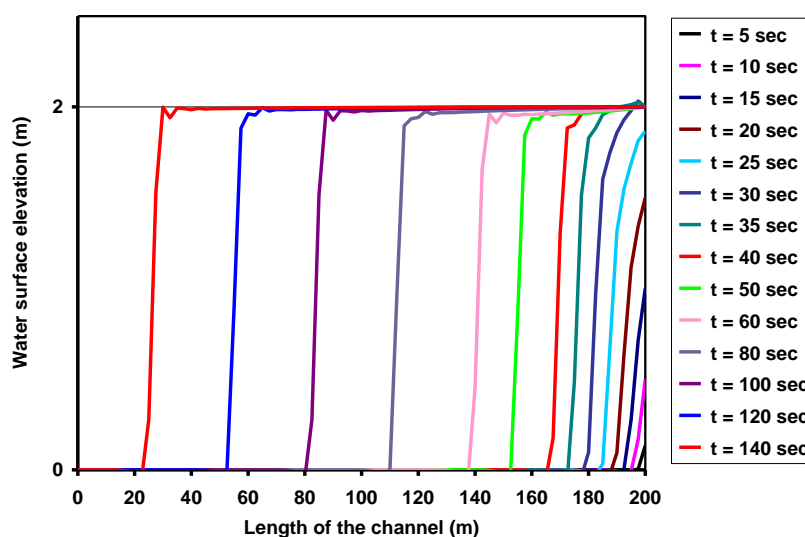


Figure 4. Water profiles along the channel due to bore propagation.

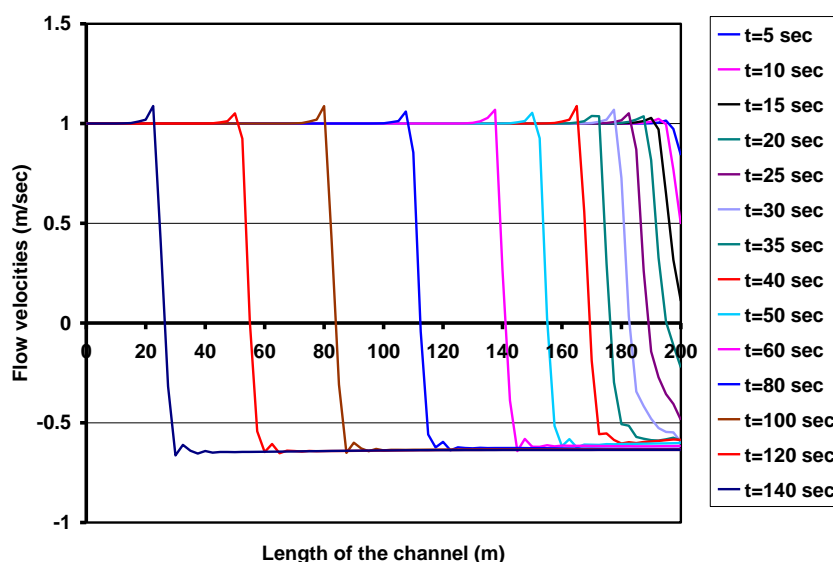


Figure 5. Flow velocities along the channel due to bore propagation.

#### 4.2. Two-dimensional problems

A partial breaking of a dam over a wet bed which described in [9,30,32-34] is used to examine the shock capturing capability of the shallow water models. In this benchmark problem, the solution domain is a  $200 \times 200 \text{ m}^2$  flat rectangular domain with an asymmetric break. The whole domain is divided into  $40 \times 80$  triangular elements with the same sizes. The dam thickness is  $5 \text{ m}$  in the direction of flow and the asymmetrical breaking part of dam has  $75 \text{ m}$  width. This breaking part is located in distance of  $95 \text{ m}$  from the right-hand side of the domain. Additional details of the domain are shown in Figure 6. The water depths inside the reservoir and in the tillage are  $10 \text{ m}$  and  $5 \text{ m}$ , respectively. By collapsing the dam, the water

moves toward the tillage. The flow field is computed numerically for 19 *sec* after the dam collapse. After breaking the dam, downstream traveling positive waves and upstream traveling negative waves are produced. The flow conditions were computed for  $t = 7.2$  *sec* after the dam failure. At time  $t = 7.2$  *sec*, the bore is well developed in the central portion of the tillage and the wave front has reached the left-hand bank of the domain.

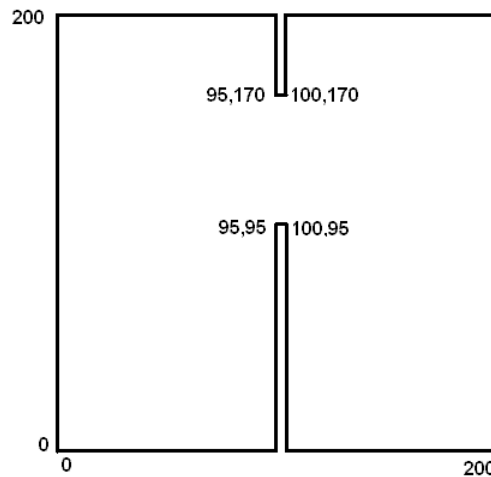


Figure 6. Geometry of the computational domain for partial dam-break.

Since no analytical solution is available for this problem, the results are compared with the reported ones by another numerical scheme in [32]. The numerical results is close to the results of aforementioned research. The results are presented in Figures 7 and 8 and compared with the solutions reported in [32]. In Figure 7, water surface elevations, presented as perspective plot of water surface, are compared with the result reported in [32]. The other comparison is carried out for water elevation contours in Figure 8. As shown in these Figures, the obtained results are in good agreement with those of previous works.

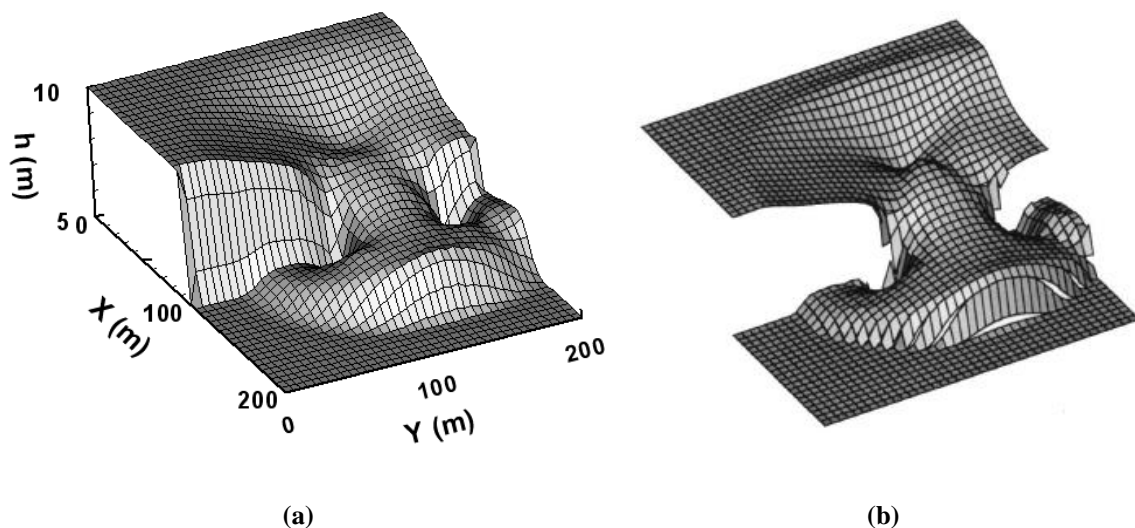


Figure 7. Water surface profiles for partial dam-break at  $t = 7.2$  *sec*

(a) Obtained by the model and (b) Reported in [32].

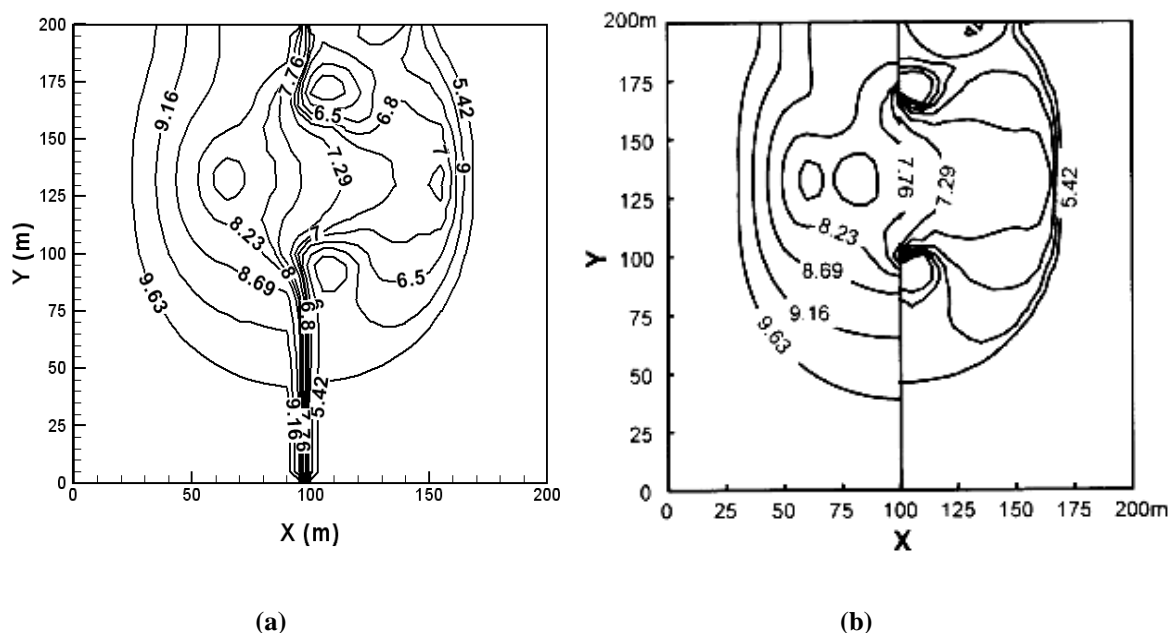


Figure 8- Water elevation contours for partial dam-break at  $t = 7.2$  sec  
(a) obtained by the model and (b) reported in [32].

## 5. Conclusions

The CBS finite element model was presented for the solution of the two-dimensional dam-break problem. The described CBS finite element model has some significant features. Its stability is based on the flow velocity instead of the celerity which is especially useful for modeling the long term problems. The improved stability of the CBS algorithm along with its capability in simulating both sub- and super-critical flows are considered as main advantages of the method. Due to the highly non-linear nature of the dam-break problem, the model was verified using both one-dimensional and two-dimensional hypothetical dam-breaking. In spite of the high non-linearity in these problems, the comparison of the computational results with the analytical solutions and reported results of other numerical models, indicated the favorable performance of the used procedure in modeling the dam-break problems. As an important result, the described model can safely be used as an efficient tool for modeling other complicated free surface hydraulic problems. Based on the results of the presented test cases which indicated the high performance of the CBS finite element method, the model can be used for natural dam-break problems in different situations.

## Acknowledgment

The author should like to thank Prof. Pablo Ortiz for his valuable helps on the CBS coding of shallow water equations. Also, special thanks to Dr. Mohammad H. Afshar for his useful helps and comments on the manuscript.

## References

1. Wu G, Yang Zh, Zhang K, Dong P, Lin Y, (2018). A Non-Equilibrium Sediment Transport Model for Dam Break Flow over Moveable Bed Based on Non-Uniform Rectangular Mesh. *Water*, pp:10(5): 1-22.
2. Kocaman S, Ozmen-Cagatay H, (2015). Investigation of dam-break induced shock waves impact on a vertical wall. *Journal of Hydrology*, pp:525: 1–12.
3. Zheng XG, Pu JH, Chen RD, Liu XN, Shao SD, (2016). A Novel Explicit-Implicit Coupled Solution Method of SWE for Long-term River Meandering Process Induced by Dam break. *Journal of Applied Fluid Mechanics*, pp:9(6): 2647-2660.
4. Seyedashraf O, Mehrabi M, Akhtari AA, (2018). Novel approach for dam break flow modeling using computational intelligence. *Journal of Hydrology*, pp:559: 1028–1038.
5. Fang Q, Tang Ch, Chen Zh, Wang Sh, Yang T, (2019). A calculation method for predicting the run out volume of dam-break and non-dam-break debris flows in the Wenchuan earthquake area. *Geomorphology*, pp:327: 201–214.
6. Issakhov A, Zhandaulet Y, Nogaeva A, (2018). Numerical simulation of dam break flow for various forms of the obstacle by VOF method. *International Journal of Multiphase Flow*, pp:109 : 191–206.
7. Erpicum S, Dewals BJ, Archambeau P, Pirotton M, (2010). Dam break flow computation based on an efficient flux vector splitting. *Journal of Computational and Applied Mathematics*, pp:234: 2143–2151.
8. Sun X, Zhang J, Ren X, (2012). Characteristic-Based Split (CBS) Finite Element Method for Incompressible Viscous Flow with Moving Boundaries. *Engineering Applications of Computational Fluid Mechanics*, pp:6(3): 461-474.
9. Zoppou C, Roberts S, (2000). Numerical solution of the two-dimensional unsteady dam-break. *Applied Mathematical Modeling*, pp:24 (7):457-475.
10. Nithiarasu P, Zienkiewicz OC, (2000). On stabilization of the CBS algorithm: Internal and external time steps. *International Journal for Numerical Methods in Engineering*, pp:48:875-880.
11. Baggio, G. A. P., Silva, J. B. C. (2016). Tridimensional flow simulation with finite element stabilized by CBS scheme. *Proceedings of the XXXVII Iberian Latin-American Congress on Computational Methods in Engineering*, Brasília, DF, Brazil, November 6-9.
12. Douglas J, Russell TF, (1982). Numerical methods for convection-dominated diffusion problems based on combining the method of characteristics with finite element or finite difference procedures. *SIAM Journal of Numerical Analysis*, pp:19:871-885.

13. Jiang C, Zhang Z, Han X, Liu G, Lin T, (2018). A cell-based smoothed finite element method with semi-implicit CBS procedures for incompressible laminar viscous flows. *International Journal for Numerical Methods in Fluids*, pp:86:20-45.
14. Morandi-Cecchi M, Venturin M, (2006). Characteristic-based split (CBS) algorithm finite element modeling for shallow waters in the Venice lagoon. *International Journal for Numerical Methods in Engineering*, pp:66:1641-1657.
15. Ortiz P, (2012). Non-oscillatory continuous FEM for transport and shallow water flows. *Computer Methods in Applied Mechanics and Engineering*, pp:223:55–69.
16. Ortiz P, Zienkiewicz OC, Szmelter J, (2006). Hydrodynamics and transport in estuaries and rivers by the CBS finite element method. *International Journal for Numerical Methods in Engineering*, pp:66:1569-1586.
17. Ortiz, P., Zienkiewicz, O. C., Szmelter, J. (2004). CBS finite element modeling of shallow water and transport problems. *European Congress on Computational Methods in Applied Sciences and Engineering*, pp. 1–14.
18. Parsa, J., Afshar, M. H. (2006). CBS finite element model for shallow water problems. 7<sup>th</sup> International Conference on Coasts, Ports and Marine Structures, Book of abstract, pp. 32, Tehran, Iran, November 27-29.
19. Wang D, Tham LG, Shui Q, (2013). Dam-break model with Characteristic-Based Operator-Splitting Finite Element Method. *Computer Modeling in Engineering and Science*, pp:91(5):355-376.
20. Zienkiewicz OC, Nithiarasu P, Codina R, Vazquez M, Ortiz P, (1999). An efficient and accurate algorithm for fluid mechanics problems: The characteristic based split procedure. *International Journal of Numerical Methods in Fluids*, pp:31:359–392.
21. Zienkiewicz OC, Ortiz P, (1995). A split characteristic based finite element model for the shallow water equations. *International Journal for Numerical Methods in Fluids*, pp:20:1061–1080.
22. Zienkiewicz O.C., Taylor R.L., *The finite element method: Volume 3: Fluid dynamics*, Butterworth Heinemann, pp.218–228, 2000.
23. Chorin A, (1968). Numerical solution of the Navier Stokes equations. *Mathematics of Computation*, pp:22:745–762.
24. Daubert A, Graffe O, (1967) Quelques aspects des écoulements presque horizontaux a deux dimensions en plan et nonpermanents application aux estuaries. *La Houille Blanche*, pp:8:847-860.
25. Verboom G., Stelling G., Officier M., *Boundary conditions for the shallow water equations: Engineering Applications of Computational Hydraulics*, Vol.1, Pitman, London, 1982.

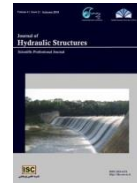


26. Ortiz P, (2004). Finite elements using a plane wave basis for scattering of surface water waves. *Philosophical Transactions of the Royal Society of London, Series A*, pp:362:1-16.
27. Ortiz P, Sanchez E, (2001). Improved partition of unity finite element model for diffraction problems. *International Journal for Numerical Methods in Engineering*, pp:50:2727-2740.
28. Labadie G., Dalsecco S., Latteaux B., Resolution des equations de Saint Venant par une methode de elements finis, EDF Report HE/41/82, 1982.
29. Stoker J.J., Water waves: The mathematical theory with application, Interscience Publication, John Wiley & Sons, Inc., New York, 1957.
30. Alcrudo F, Garcia-Navarro P, (1993). A high-resolution Gudnov-type scheme in finite volumes for the 2-D shallow water equations. *International Journal for Numerical Methods in Fluids*, pp:16(6):489-505.
31. Hervouet J.M., Hydrodynamics of Free Surface Flows: Modelling with the Finite Element Method, Wiley, London, 2007.
32. Fagherazzi S, Rasetarinera P, Hussaini MY, Furbish DJ, (2004). Numerical solution of the dam-break problem with a discontinuous Galerkin method. *Journal of Hydraulic Engineering*, pp:130(6):532-539.
33. Fennema RJ, Chaudhry MH, (1990) Explicit methods for 2D transient free-surface flows. *Journal of Hydraulic Engineering*, pp:116(8):1013-1034.
34. Biscarini C, Francesco SDi, Manciola P, (2010). CFD modelling approach for dam break flow studies. *Hydrology and Earth System Sciences*, pp:14: 705–718.



© 2018 by the authors. Licensee SCU, Ahvaz, Iran. This article is an open access article distributed under the terms and conditions of the Creative Commons Attribution 4.0 International (CC BY 4.0 license) (<http://creativecommons.org/licenses/by/4.0/>).





## **Boundary Integral Equations for Quasi-Static Unsaturated Porous Media**

Ehsan Jabbari<sup>1</sup>  
Mazda Behnia<sup>2</sup>

### **Abstract**

One of the principal criteria for development of the boundary element method (BEM) in porous media is derivation of the required fundamental solutions in the boundary integral equations (BIE). Furthermore, setting up the governing BIEs based on the governing partial differential equations (PDE) is another challenge in solving a physical phenomenon using BEM. In this regard, the governing BIEs for unsaturated porous media have been developed using the available derived fundamental solutions. In this research, a perturbation type approximation is exploited for developing a system of BIEs for the quasi-static unsaturated porous media with moderate variations in its properties. Nevertheless, the fundamental solutions of the medium with constant properties are applied. The method produces two sets of equations with constant parameters instead of the original equations. Besides, the required boundary conditions have been formulated. This type of BIEs is essential to be used in the BEM for unsaturated porous media as the fundamental solutions for a medium with coordinates dependent properties is not available so far. The resulted introduced BIEs may be used directly in a BEM numerical model for an unsaturated porous media in one, two or three dimensional conditions.

**Keywords:** Unsaturated porous media, Boundary Integral Equation, Fundamental Solutions, Quasi-Static, Perturbation.

Received: 8 December 2018; Accepted: 25 December 2018

### **1. Introduction**

Unsaturated soil, as a prevailing medium that surrounds most of the structures, has been of great interest during four past decades. Therefore, a considerable number of researches have been devoted to modeling its characteristics. The Biot's theory is often used as a mathematical model for the dynamic behavior in saturated soils. Its application to unsaturated soil problems is

---

<sup>1</sup> Department of Civil Engineering, University of Qom , Qom, Iran ,ehsan.jabbari@gmail.com  
(Corresponding author)

<sup>2</sup> Department of Civil Engineering, University of Qom , Qom, Iran, m.azizkhani78@gmail.com



possible under certain sets of conditions [1]. The Biot's theory has been extended to nearly saturated porous media by Aifantis and Wilson and Aifantis for the quasi-static case, however, there are several other theories for partially saturated media or media with more phases [2].

BIE methods are among the most efficient numerical methods which depends strongly on finding the fundamental solutions of the governing homogenous PDEs, especially in the BEM. Therefore, many efforts have been devoted on finding the fundamental solutions for different cases of the problem. The first set of fundamental solutions for saturated media has been introduced by Cleary [3]. Then, several researches have been published on the fundamental solutions for different phenomena of saturated porous media such as deformation and heat conduction. In contrast, the fundamental solutions for unsaturated media have been published recently. Gatmiri and Jabbari derived the first static and quasi-static fundamental solutions of the problem in both Laplace and time domains [4], [5]. Later, Maghoul et al. presented coupled thermo-hydro-mechanical fundamental solutions for the same quasi-static loading condition of the unsaturated soil for two and three-dimensional time domains [6]. Ashayeri et al. introduced fundamental solutions for the dynamic problem in both 2D and 3D cases. A similar problem has been studied by Li and Schanz [7]. Ghorbani et al [8] studied the non-linear behavior of the solid skeleton of the soil in the analysis of multiphase unsaturated soils when subjected to both static and dynamic loading. Igumnov et al [9] considered wave propagation in fully and partially saturated porous media with examples of two-components and three-components. Igumnov et al [10] deduced the solution of a finite one-dimensional column with Neumann and Dirichlet boundary conditions based on the theory of mixture.

More capabilities of the BEM may be realized when the required fundamental solutions to be available. Unfortunately, it is not always the case, instantly, for inhomogeneous soils, where the fundamental solutions have been derived only in a few very particular cases e.g. when the Poisson's ratio is equal to 0.25 [11]. In the absence of the required fundamental solution the bothering problems of the BEM such as domain integrals on the domain will arise.

In unsaturated porous media, the state variables are the stress tensor, air and water pressures that change spatially, so a nonhomogeneous medium must be considered. In such a case, the boundary elements method seems to be ineffective. In detail, for the quasi-static case of the porous media the fundamental solutions in hand, which have been found for a homogeneous medium, are not efficient. Also, the assumptions that have been considered for finding the fundamental solutions for other media do not appear useful here e.g. when the Poisson's ratio is constant or when the variation of the state variables is a predefined pattern. Hence, in this paper, two boundary equation sets have been developed for the problem, when the parameters of the medium are varied slightly near a mean value. The first set concerned with a medium that has constant parameters and the second considers the effects of variation of the parameters. The toll was the appearance of a secondary set of equations which should be resolved. These sets of equations must be applied to make a BEM model. Additionally, more accuracy may be desired when large variations in the medium handled by employing the multi-region technique.

In this paper the governing equations are briefly reviewed. Then changes in different parameters of the medium are found in terms of the changes of the state parameters and the governing equations are rewritten using this perturbed type of parameters. Then the integral equations have been developed and the boundary conditions are revised for the effects of the changes in state parameters. Finally, two sets of boundary integral equations have been constituted up which employ the fundamental solutions of the homogeneous medium.

## 2. Governing Equations

The effective stress of the matrix of a porous medium may be written in terms of the displacements and pressures of fluid. For an elastic isotropic medium, the constitutive equations are [12]:

$$(\sigma_{ij} + \delta_{ij}P^a) = \lambda \delta_{ij} u_{k,k} + \mu (u_{i,j} + u_{j,i}) + \delta_{ij} D_s (P^a - P^w) \quad (1)$$

Where  $\lambda$  and  $\mu$  are the Lamé's coefficients for the skeleton,  $P^a$  and  $P^w$  are the gas (air) and the liquid (water) phase pressures, respectively, and  $D_s$  is the isotropic Biot's coefficient for the fluid phase [12]. For a nonlinear elastic material, the equations may be linearized by the incremental form as [4]:

$$d(\sigma_{ij} + \delta_{ij}P^a) = D_{ijkl} d\varepsilon_{kl} + \delta_{ij} D_s (dP^a - dP^w) \quad (2)$$

The parameters in eq. (1) are functions of the state variables, but in the incremental form (eq. (2)) they are functions of the spatial coordinates.

The momentum balance equation for the medium with the constitutive equation (2) and ignoring accelerations (to model the quasi-static case) of distinct phases could be written as [4]:

$$(\lambda + \mu) du_{j,i} + \mu du_{i,j} - \delta_{ij} (1 - D_s) dP^a - \delta_{ij} D_s dP^w = 0 \quad (3)$$

The mass of medium does not play any role in the incremental equation because it does not change, besides, the acceleration has been dropped. Furthermore, we can replace the saturation ratio for  $D_s$  to find a simpler equation [13].

The saturation ratio, like every other parameter of the medium, is governed by the state variables. But we use a simple one which only needs for the suction [14] (a complete form could be seen in [9]):

$$Sr = \alpha + \beta \text{Log}(P^a - P^w) \quad (4)$$

In this equation,  $Sr$  stands for the saturation ratio,  $\alpha$  and  $\beta$  are constants.

For investigation of the mass balance of distinct phases a moving control volume attached to the solid skeleton has been considered that ensures the mass balance of the solid phase, but balance of other phases should be certified. Assumption of the incompressibility of the liquid phases let replacing the balance of volume equations for the balance of masses:

$$\frac{\partial}{\partial t} (n(1 - Sr)) + q_{i,i}^a = 0 \quad (5)$$

$$\frac{\partial}{\partial t} (nSr) + q_{i,i}^w = 0 \quad (6)$$

Where  $q_i^\alpha$  denotes the fluid volume fluxes ( $\alpha = a \text{ or } w$ ). It should be noted that the solution of air in the water has been ignored here, which may restrict application of these equations. However, in the case of constant ratio of dissolved air, they could be said by getting the mixture of water and dissolved air as the liquid phase. Equation (4) is needed in the incremental form which reveals the increment of the saturation ratio in terms of the increments of the state variables:

$$dSr = \beta \frac{(dP^a - dP^w)}{(\hat{P}^a - \hat{P}^w)} \quad (7)$$

Where  $\hat{P}^a$  and  $\hat{P}^w$  stand for the pressures of air and water in the last step, respectively.

Darcy's law has been exploited to evaluate the fluxes and then the continuity equation for gas

and liquid phases could be written as [4]:

$$-\left(\frac{K^w}{\gamma^w} dP^w\right)_{,i} + Srd\dot{u}_{i,i} + \frac{\beta\hat{n}}{(\hat{p}^a - \hat{p}^w)} (d\dot{P}^a - d\dot{P}^w) = 0 \quad (8)$$

$$-\left(\frac{K^w}{\gamma^w} dP^w\right)_{,i} + Srd\dot{u}_{i,i} + \frac{\beta\hat{n}}{(\hat{p}^a - \hat{p}^w)} (d\dot{P}^a - d\dot{P}^w) = 0 \quad (9)$$

Where the dot stands for a temporal derivation. Equations (3), (8) and (9) form the governing equations of the problem.

The Laplace transform is a perfect and usual tool for solving such a problem [12], [4], [3]. The following equations are achieved after applying the Laplace transform on the governing equations and assuming the parameters of the medium to be constants:

$$c_{11}d\tilde{u}_{j,ij} + c_{12}d\tilde{u}_{i,jj} + c_{13}d\tilde{P}_{,i}^a + c_{14}d\tilde{P}_{,i}^w = 0 \quad (10)$$

$$c_{21}d\tilde{u}_{i,i} + c_{22}d\tilde{P}^a + c_{23}d\tilde{P}_{,ii}^a + c_{24}d\tilde{P}^w = 0 \quad (11)$$

$$c_{31}d\tilde{u}_{i,i} + c_{32}d\tilde{P}^a + c_{33}d\tilde{P}_{,ii}^w + c_{34}d\tilde{P}^w = 0 \quad (12)$$

In which the tiled mark ( $\sim$ ) stands for the Laplace domain variables. In addition, for an incremental model, the initial conditions are assumed to be zero. The  $c_{ij}$  coefficients are:

$$\begin{aligned} c_{11} &= (\lambda + \mu) \\ c_{12} &= \mu \\ c_{13} &= -(1 - Sr) \\ c_{14} &= -Sr \\ c_{21} &= s(1 - Sr) \\ c_{22} &= -c_{24} = -c_{32} = c_{34} = \frac{-s\beta\hat{n}}{(\hat{P}^a - \hat{P}^w)} \\ c_{23} &= -\frac{K^a}{\gamma^a} \\ c_{31} &= sSr \\ c_{33} &= -\frac{K^w}{\gamma^w} \end{aligned} \quad (13)$$

The spatial variations of the state variables cause the parameters of the media to experience some spatial variations. Nevertheless, only the fundamental solutions are developed for constant parameters and are not applicable directly here. For using these fundamental solutions, it has been assumed that the state variables change slightly in the domain:

$$\frac{\sigma'_{ij}(x)}{P^c(0)} = \frac{\sigma'_{ij}(0)}{P^c(0)} + \varepsilon\theta_{\sigma_{ij}}(x) \quad (14)$$

$$\frac{P^a(x)}{P^c(0)} = \frac{P^a(0)}{P^c(0)} + \varepsilon\theta_a(x) \quad (15)$$

$$\frac{P^w(x)}{P^c(0)} = \frac{P^w(0)}{P^c(0)} + \varepsilon \theta_w(x) \quad (16)$$

In these equations  $\varepsilon$  is a constant in some trivial size and  $\theta_\alpha(x)$ ;  $\alpha = \sigma'_{ij}, a, w$  are functions of the coordinates which show the distribution of the variables. These functions are of order one ( $O(1)$ ) and cannot violate the assumption of slight changes in the state variables. The effective stress field is shown by  $\sigma'(x)$  and the pressure fields of fluids are denoted by  $P^a(x)$  and  $P^w(x)$  for air and water, respectively. In equations (14) to (16) the fields of the state parameters have been revealed in terms of their value in the origin and the ratio of their variation to the value of the suction at the origin. The origin should be chosen properly to satisfy these equations and the domain could be divided to distinct regions, if necessary.

The suction pressure could be considered as a function of the saturation ratio [14] and its value for some types of soils could be very large. Therefore, the relative changes of the suction could be small (see eq. (7)). Additionally, the resistance to the air flow is very small that the air pressure could be assumed equal to the atmosphere pressure at all points of the system or, at least, vary slightly [13]. Consequently, equations (15) and (16) could be claimed. The ratio of the variations of the effective stress and the suction pressure has been assumed small, so, equation (14) could be written.

The variations in the parameters affect the solution which could be assessed using multi variable Taylor's series. Here, only the first orders have been considered and the results are:

$$\begin{aligned} du_i \left( x, \frac{\sigma'_{ij}(x)}{P^c(0)}, \frac{P^a(x)}{P^c(0)}, \frac{P^w(x)}{P^c(0)} \right) &= du_i \left( x, \frac{\sigma'_{ij}(0)}{P^c(0)}, \frac{P^a(0)}{P^c(0)}, \frac{P^w(0)}{P^c(0)} \right) \\ &+ \varepsilon \left( \frac{\partial du_i}{\partial(\sigma'_{ij}/P^c(0))} \theta_{\sigma'_{ij}} + \frac{\partial du_i}{\partial(P^a/P^c(0))} \theta_{P^a} + \frac{\partial du_i}{\partial(P^w/P^c(0))} \theta_{P^w} \right) \\ &= du_{i0}(x) + \varepsilon du_{i1}(x) \end{aligned} \quad (17)$$

$$dP^a \left( x, \frac{\sigma'_{ij}(x)}{P^c(0)}, \frac{P^a(x)}{P^c(0)}, \frac{P^w(x)}{P^c(0)} \right) = dP^a_0(x) + \varepsilon dP^a_1(x) \quad (18)$$

$$dP^w \left( x, \frac{\sigma'_{ij}(x)}{P^c(0)}, \frac{P^a(x)}{P^c(0)}, \frac{P^w(x)}{P^c(0)} \right) = dP^w_0(x) + \varepsilon dP^w_1(x) \quad (19)$$

There is a perturbation type expansion, which approximates the solutions of the equations as a combination of solutions for the medium with constant parameters including a small perturbation. This result could be a premium assumption in other perturbation method equations such as in [15] and [16].

In appendix A, it has been shown that all other parameters could be written in the form of equation (20). Namely, for a typical parameter F:

$$F \left( x, \frac{\sigma'_{ij}(x)}{P^c(0)}, \frac{P^a(x)}{P^c(0)}, \frac{P^w(x)}{P^c(0)} \right) = F(0)(1 + \varepsilon \theta_F(x)) \quad (20)$$

Where  $F(0)$  is the value of the typical parameter  $F$  in the origin and  $\theta_F$  is a normalized function of coordinates to account the spatial changes of factor  $F$ .

Using the coordinate dependent parameters in the governing equations, computing the derivatives and then ignoring the second and higher orders of  $\varepsilon$  lead to a new set of equations based on  $\varepsilon$  and the theta functions. These equations could be separated into two sets, one consists of the terms without  $\varepsilon$  (or with  $\varepsilon^0$ ) and the other has the terms with  $\varepsilon$  (or with  $\varepsilon^1$ ) named zero and first order equations, respectively. The zero order equations are related to an imagined medium constant parameters which could be found at the origin and the other set reflects the effects of derivatives of the parameters when  $\varepsilon$  has not been vanished. They are as follow:

The zero order equations:

$$(\lambda(0) + \mu(0))d\tilde{u}_{0,jj} + \mu(0)d\tilde{u}_{0,i,jj} - (1 - Sr(0))d\tilde{P}^a_{0,i} - Sr(0)d\tilde{P}^w_{0,i} = 0 \quad (21)$$

$$-K^a(0)d\tilde{P}^a_{0,ii} + s(1 - Sr(0))d\tilde{u}_{0,i} - s\frac{\beta n(0)}{P^c(0)}(d\tilde{P}^a_{0,i} - d\tilde{P}^w_{0,i}) = 0 \quad (22)$$

$$-K^w(0)d\tilde{P}^w_{0,ii} + sSr(0)d\tilde{u}_{0,i} + s\frac{\beta n(0)}{P^c(0)}(d\tilde{P}^a_{0,i} - d\tilde{P}^w_{0,i}) = 0 \quad (23)$$

In which  $P^c$  stands for the suction pressure  $P^a - P^w$  and  $P^c(0)$  is its value in the origin and both are in the earlier time step.

The first order equations:

$$(\lambda(0) + \mu(0))d\tilde{u}_{1,jj} + \mu(0)d\tilde{u}_{1,i,jj} - (1 - Sr(0))d\tilde{P}^a_{1,i} - Sr(0)d\tilde{P}^w_{1,i} = \tilde{F}_i \quad (24)$$

$$-K^a(0)d\tilde{P}^a_{1,ii} + s(1 - Sr(0))d\tilde{u}_{1,i} - s\frac{\beta n(0)}{P^c(0)}(d\tilde{P}^a_{1,i} - d\tilde{P}^w_{1,i}) = \tilde{F}^a \quad (25)$$

$$-K^w(0)d\tilde{P}^w_{1,ii} + sSr(0)d\tilde{u}_{1,i} + s\frac{\beta n(0)}{P^c(0)}(d\tilde{P}^a_{1,i} - d\tilde{P}^w_{1,i}) = \tilde{F}^w \quad (26)$$

In which the right-hand side values are:

$$\tilde{F}_i = -\lambda(0)(\theta_{\lambda}d\tilde{u}_{0,i,jj} + \theta_{\lambda,i}d\tilde{u}_{0,j,j}) - \mu(0)(\theta_{\mu}(d\tilde{u}_{0,i,jj} + d\tilde{u}_{0,j,ij}) + \theta_{\mu,j}(d\tilde{u}_{0,i,j} + d\tilde{u}_{0,j,i})) - Sr(0)(\theta_{Sr}dP^c_{0,i} + \theta_{Sr,i}dP^c_{0,i}) \quad (27)$$

$$\tilde{F}^a = -sSr(0)\theta_{Sr}d\tilde{u}_{0,i} + K^a(0)(\theta_{K^a}d\tilde{P}^a_{0,ii} + \theta_{K^a,i}d\tilde{P}^a_{0,i}) + s\frac{\beta n(0)}{P^c(0)}(\theta_n - \theta_{P^c})(d\tilde{P}^a_{0,i} - d\tilde{P}^w_{0,i}) \quad (28)$$

$$\tilde{F}^w = -sSr(0)\theta_{Sr}d\tilde{u}_{0,i} + K^w(0)(\theta_{K^w}d\tilde{P}^w_{0,ii} + \theta_{K^w,i}d\tilde{P}^w_{0,i}) - s\frac{\beta n(0)}{P^c(0)}(\theta_n - \theta_{P^c})(d\tilde{P}^a_{0,i} - d\tilde{P}^w_{0,i}) \quad (29)$$

Where the values that denoted with (0) (such as  $\lambda(0)$ ) have been measured at the origin and at the earlier step. In addition, the zero order solution values (for example  $du_{0,i}$ ) are known values when the first order equations are going to be solved. The computational procedure has been illustrated in Fig. 1.

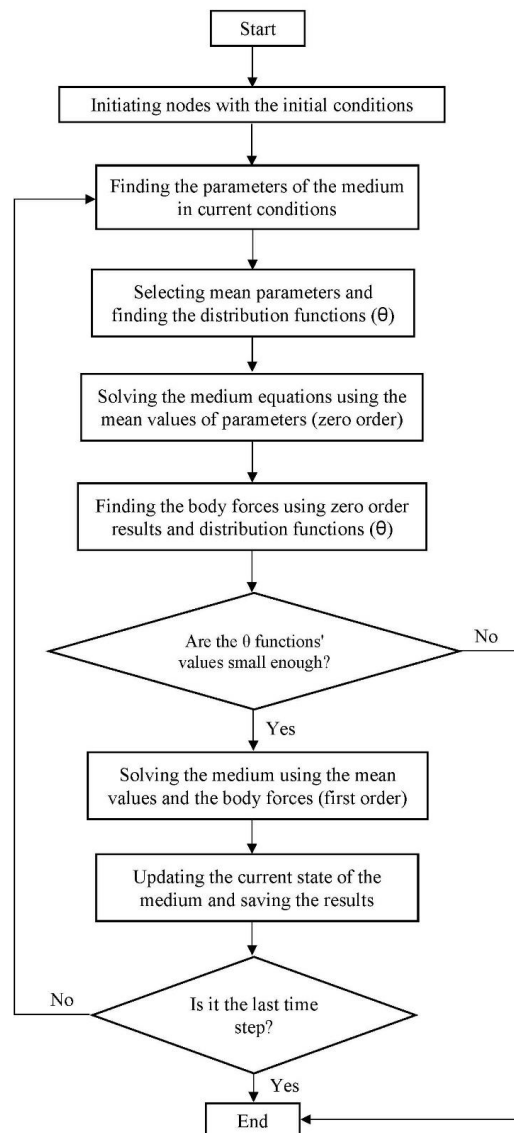


**Figure 1: The Flowchart of the computational algorithm.**

### 3. Boundary conditions

The boundary conditions are necessary for a set of differential equations to be solved. The governing differential equations system has been replaced with two new sets of differential equations so two sets of boundary conditions are needed. Here, the boundary conditions have been restricted to the Dirichlet and the Neumann types. Though, the extension to the mixed type is easy.

The zero order equations should satisfy the Dirichlet type boundary conditions of the problem. Consequently, the first order equations need to satisfy the homogeneous version of this type of boundary conditions.

For the Neumann type boundary conditions, especially when some parameters of the medium are needed (for instance, when the boundary condition has stipulated a non-zero value for the



discharge) the local value of parameters are needed. Once more, it has been assumed that the zero order equations which emulate the response of a homogeneous medium, should meet the boundary conditions when the parameters found from such a medium. Thus, the first order equations need a new set of boundary conditions to omit the error caused by the boundary conditions of the zero order equations. It causes a new set of boundary conditions that has been developed here. The following boundary condition may be assumed:

$$dq_w = \bar{q}_w \text{ on } \Gamma_1 \quad (30)$$

which may be written as:

$$-\frac{K_w(0)}{\gamma_w} (1 + \varepsilon \theta_{K^w}) (dP0^w + \varepsilon dP1^w)_{,i} n_i = d\bar{q}_w \text{ on } \Gamma_1 \quad (31)$$

$$-\frac{K_w(0)}{\gamma_w} dP0_{,i}^w n_i = dq_w(0) = d\bar{q}_w \text{ on } \Gamma_1 \quad (32)$$

$$dP1_{,i}^w n_i = -\theta_{K^w} dP0_{,i}^w \text{ on } \Gamma_1 \quad (33)$$

Where the first boundary condition (eq. (32)) has been satisfied by zero order equations and the last one (eq. (33)) should be satisfied by the first order equations. This new type of boundary conditions, together with the first order equations could be solved now.

#### 4. Boundary Integral Equations

A set of boundary integral form of the governing equations is crucial for implementing the BEM. After finding the weak form of the equations in the weighted residual method, two distinct strategies are available to achieve a set of boundary integral equations. Some methods have been found by taking the weight functions as fundamental solutions of the governing equations [17], [18]. This procedure is named the convolution method [19]. The other strategy uses the fundamental solutions of the adjoint operator of the main problem. Such a strategy which could be seen in [20] and [6] is known as the correlation method [19]. Then the desired boundary integral equations may be found by choosing the collocation points on the boundaries.

Later, two sets of equations were derived which lead to various parts of the solution as they have been defined in (17) to (19). These equations are stipulated in (21) to (23) and (24) to (26) but, it could be seen that the equations are similar, but the boundary conditions are different. Therefore, a set of equation should be investigated, and a set of matrices will be needed for both equation sets. Although, the right-hand side of the equations need to be prepared distinctly for each set of equations.

The details of the conversion of the set of differential equations could be found in [12], where a set of dynamic type of the problem has been converted to a set of convolution type boundary integral equations. After dropping the acceleration terms of the equations and changing some constants with their counterpart in the current problem we have [12] :

$$\begin{aligned} & s \int_{\Gamma} \left( d\tilde{T}_i \hat{u}_i - \tilde{T}_i d\tilde{u}_i \right) d\Gamma + \int_{\Gamma} \left( \hat{\tilde{P}}^a d\tilde{Q}^a - d\tilde{P}^a \hat{\tilde{Q}}^a \right) d\Gamma + \int_{\Gamma} \left( \hat{\tilde{P}}^w d\tilde{Q}^w - d\tilde{P}^w \hat{\tilde{Q}}^w \right) d\Gamma \\ & - s \int_{\Omega} \left( \hat{\tilde{b}}_i d\tilde{u}_i \right) d\Omega + \int_{\Omega} \left( d\tilde{P}^a \hat{\tilde{\gamma}}^a - \hat{\tilde{P}}^a d\tilde{\gamma}^a \right) d\Omega + \int_{\Omega} \left( d\tilde{P}^w \hat{\tilde{\gamma}}^w - \hat{\tilde{P}}^w d\tilde{\gamma}^w \right) d\Omega \\ & = \int_{\Omega} \left( s\tilde{F}_i \hat{\tilde{u}}_i + F_a \hat{\tilde{P}}^a + F_w \hat{\tilde{P}}^w \right) d\Omega \end{aligned} \quad (34)$$

where:

$$\hat{\hat{T}}_i = \left( \lambda(0) \delta_{ij} \hat{\hat{u}}_{k,k} + \mu(0) (\hat{\hat{u}}_{i,j} + \hat{\hat{u}}_{j,i}) - (1 - Sr(0)) \hat{\hat{P}}^a - Sr(0) \hat{\hat{P}}^w \right) n_j \quad (35)$$

$$\hat{\hat{Q}}^a = -K^a(0) \hat{\hat{P}}_{,j}^a n_j \quad (36)$$

$$\hat{\hat{Q}}^w = -K^w(0) \hat{\hat{P}}_{,j}^w n_j \quad (37)$$

The right-hand side domain integral is equal to zero for zero order equations, but it should be found for first order equations where  $\tilde{F}_\alpha$  could be found in equations (27) to (29).

To have a time domain reciprocal integral, an inverse Laplace transform should be implemented. So, all products change to the convolution products:

$$\begin{aligned} & \int_{\Gamma} (dT_i \times \hat{u}_i - \hat{T}_i \times d\tilde{u}_i) d\Gamma + \int_{\Gamma} (\hat{P}^a \times dQ^a - dP^a \times \hat{Q}^a) d\Gamma \\ & \quad + \int_{\Gamma} (\hat{P}^w \times dQ^w - dP^w \times \hat{Q}^w) d\Gamma \\ & - \int_{\Omega} (\hat{b}_i \times du_i) d\Omega + \int_{\Omega} (dP^a \times \hat{\gamma}^a - P^a \times d\hat{\gamma}^a) d\Omega + \int_{\Omega} (dP^w \times \hat{\gamma}^w - \hat{P}^w \times d\gamma^w) d\Omega \quad (38) \\ & = \int_{\Omega} (\hat{F}_i \times \hat{u}_i + F_a \times \hat{P}^a + F_w \times \hat{P}^w) d\Omega \end{aligned}$$

To have a boundary integral equation some domain integrals should be omitted except for the right-hand side domain integral. So, it is needed to  $d\gamma^w = d\gamma^a = 0$  which removes the bothering domain integrals.

Now the case  $\hat{b}_i = \delta(x)H(t)$  and  $\hat{\gamma}^a = \hat{\gamma}^w = 0$  will be considered in which  $H(t)$  stands for the Heaviside step function and  $\delta(x)$  is the Dirac Delta function. The fundamental solutions and related traction and fluxes are specified with a hat symbol. These replacements change (22) to:

$$\begin{aligned} & \int_{\Gamma} (dT_i \times \hat{u}_i - \hat{T}_i \times d\tilde{u}_i) d\Gamma + \int_{\Gamma} (\hat{P}^a \times dQ^a - dP^a \times \hat{Q}^a) d\Gamma \\ & \quad + \int_{\Gamma} (\hat{P}^w \times dQ^w - dP^w \times \hat{Q}^w) d\Gamma \quad (39) \\ & - \int_{\Omega} (\hat{F}_i \times \hat{u}_i + F_a \times \hat{P}^a + F_w \times \hat{P}^w) d\Omega = du_i \end{aligned}$$

Same procedure for  $\hat{\gamma}^a = \delta(x)\delta(t)$  and then  $\hat{\gamma}^w = \delta(x)\delta(t)$  will results:

$$\begin{aligned} & \int_{\Gamma} (dT_i \times \hat{u}_i - \hat{T}_i \times d\tilde{u}_i) d\Gamma + \int_{\Gamma} (\hat{P}^a \times dQ^a - dP^a \times \hat{Q}^a) d\Gamma \\ & \quad + \int_{\Gamma} (\hat{P}^w \times dQ^w - dP^w \times \hat{Q}^w) d\Gamma \quad (40) \\ & - \int_{\Omega} (\hat{F}_i \times \hat{u}_i + F_a \times \hat{P}^a + F_w \times \hat{P}^w) d\Omega = dP^a \end{aligned}$$

$$\begin{aligned}
& \int_{\Gamma} (dT_i \times \hat{u}_i - \hat{T}_i \times d\tilde{u}_i) d\Gamma + \int_{\Gamma} (\hat{P}^a \times dQ^a - dP^a \times \hat{Q}^a) d\Gamma \\
& + \int_{\Gamma} (\hat{P}^w \times dQ^w - dP^w \times \hat{Q}^w) d\Gamma \\
& - \int_{\Omega} (\dot{F}_i \times \hat{u}_i + F_a \times \hat{P}^a + F_w \times \hat{P}^w) d\Omega = dP^w
\end{aligned} \quad (41)$$

Now equations (36), (37) and (38) form a set of boundary integral equations. Having fundamental solutions in hand, a standard time domain BEM procedure could be started here for  $du_i$ ,  $dP^a$  and  $dP^w$  to be found on the boundaries and then on the domain points. This procedure should be done for both zero and first order equations. Besides, after implementing the boundary conditions, the right-hand side of the first order equations is involved with the first and second order partial derivatives of the zero order solutions on the domain. It could be a weighty extra step, but it might be removed by calculation of enough data in zeroth order step and using the interpolation functions and derivations according to techniques that have been used in meshless methods [21].

The other choice to have a reciprocity type of boundary integral equations is a correlation type boundary integral equation which could be found in the dynamic version of the problem in hand [8]. After omitting the acceleration terms and converting the equal parameters name, it leads to:

$$\begin{aligned}
& \int_{\Gamma} (d\tilde{T}_i \tilde{u}_i - \tilde{T}_i d\tilde{u}_i) d\Gamma - \int_{\Gamma} (\hat{P}^a d\tilde{Q}^a - d\tilde{P}^a \hat{Q}^a) d\Gamma - \int_{\Gamma} (\hat{P}^w d\tilde{Q}^w - d\tilde{P}^w \hat{Q}^w) d\Gamma \\
& = \int_{\Omega} (\tilde{F}_i \hat{u}_i + F_a \hat{P}^a + F_w \hat{P}^w) d\Omega
\end{aligned} \quad (42)$$

This equation could be transformed to a boundary integral equation in which  $\tilde{u}_i$ ,  $\tilde{P}^a$  and  $\tilde{P}^w$  are the fundamental solutions of the adjoint operator of which leads to the governing equations. The tractions induced by the fundamental solutions could be found as:

$$\hat{T}_i = \left( \lambda(0) \delta_{ij} \tilde{u}_{k,k} + \mu(0) (\tilde{u}_{i,j} + \tilde{u}_{j,i}) + (1 - Sr(0)) \tilde{P}^a + Sr(0) \tilde{P}^w \right) n_j \quad (43)$$

$$\hat{Q}^a = K^a(0) \tilde{P}_{,j}^a n_j \quad (44)$$

$$\hat{Q}^w = K^w(0) \tilde{P}_{,j}^w n_j \quad (45)$$

These yield to the following boundary integral equations:

$$\begin{aligned}
& \int_{\Gamma} (dT_i \times \hat{u}_i - \hat{T}_i \times d\tilde{u}_i) d\Gamma - \int_{\Gamma} (\hat{P}^a \times dQ^a + dP^a \times \hat{Q}^a) d\Gamma \\
& - \int_{\Gamma} (\hat{P}^w \times dQ^w + dP^w \times \hat{Q}^w) d\Gamma \\
& - \int_{\Omega} (F_i \times \hat{u}_i + F_a \times \hat{P}^a + F_w \times \hat{P}^w) d\Omega = du_i
\end{aligned} \quad (46)$$

$$\begin{aligned} & \int_{\Gamma} (dT_i \times \hat{u}_i - \hat{T}_i \times d\tilde{u}_i) d\Gamma - \int_{\Gamma} (\hat{P}^a \times dQ^a + dP^a \times \hat{Q}^a) d\Gamma \\ & - \int_{\Gamma} (\hat{P}^w \times dQ^w + dP^w \times \hat{Q}^w) d\Gamma \end{aligned} \quad (47)$$

$$\begin{aligned} & - \int_{\Omega} (F_i \times \hat{u}_i + F_a \times \hat{P}^a + F_w \times \hat{P}^w) d\Omega = dP^a \\ & \int_{\Gamma} (dT_i \times \hat{u}_i - \hat{T}_i \times d\tilde{u}_i) d\Gamma - \int_{\Gamma} (\hat{P}^a \times dQ^a + dP^a \times \hat{Q}^a) d\Gamma \\ & - \int_{\Gamma} (\hat{P}^w \times dQ^w + dP^w \times \hat{Q}^w) d\Gamma \end{aligned} \quad (48)$$

$$- \int_{\Omega} (F_i \times \hat{u}_i + F_a \times \hat{P}^a + F_w \times \hat{P}^w) d\Omega = dP^w$$

Obviously, the right-hand side of equation (42) is equal to zero for the zero-order solution, but like the convolution type integrals for the first order equations, they should be calculated when the zero-order solution has been found.

## 5. Numerical Example

In order to show the effects of the introduced body force, a 3D model has been defined with  $7 \times 11 \times 7$  m with the data found from a real clay sample. The medium has been consolidated under its weight for a long time, so the initial conditions could be found using the properties of the soil including the special gravity and saturation ratio which varies from 50% in the surface to 64% in the depth of 7 m. A 10KN point load has been applied to the semi-infinite model and the zero order equations has been solved for a time step equal to 8640 seconds (0.1 day). Then the distribution of the characteristic parameters of the medium and finally the extra body force has been found and demonstrated. It is important to note that a small part of the medium needs extra attention for the first order solution which saves the main advantage of the boundary elements method to solve the problems in infinite and semi-infinite regions.

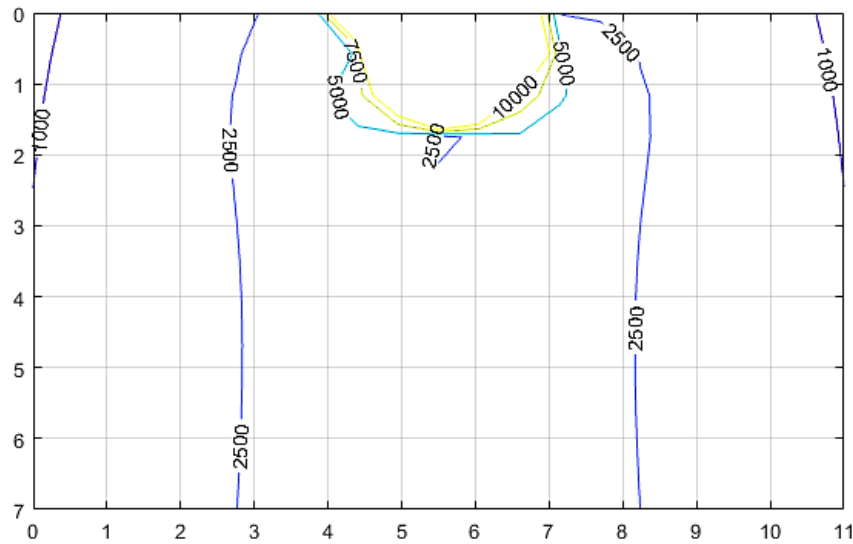


Figure 2: The body force distribution under 10 kN point load after 8640 seconds.

## 6. Conclusion

The unsaturated porous media experience an inhomogeneous condition during loading and deformation. Therefore, the complex and problem dependent changes in the parameters of the media make it impossible to derive the required fundamental solutions for the BIEs to be constituted. In this regard, a new formulation has been introduced for the medium that experiences a slight change in the parameters using the fundamental solutions of a homogeneous porous medium. It has been shown that the variation in the parameters of the medium could be found in terms of the variation of the state parameters. In addition, the considered variations are of the same order of variations of the state parameters. Then, a first order perturbation expansion has been employed for converting the set of equations with coordinates' dependent parameters to two sets of equations with constant parameters. This procedure requires the fundamental solutions of the problem to be derived while the parameters are constant, which consequently necessitates extra efforts, including two times of the standard BEM procedure, assessment of the second order derivatives of the solutions of the zero order equations and some domain integrals. Therefore, using the introduced BIEs and fundamental solutions for the unsaturated porous media, one can prepare the BEM numerical model, verify and compare the results with other numerical methods.

## Nomenclature:

- $x$  : position vector
- $\sigma_{ij}$  : the stress tensor
- $u_i$  : displacement in direction  $i$
- $\lambda$  : Lamé's constant for the skeleton
- $\mu$  : Lamé's constant for the skeleton
- $p^a$  : gas (air) phase pressure
- $p^w$  : liquid (water) phase pressure

$D_s$	: the isotropic Biot's coefficient for the fluid phase
$D_{ijkl}$	: the elasticity coefficients
$S_r$	: saturation ratio
$\alpha$	: constant in saturation ratio
$\beta$	: constant in saturation ratio
$K^\alpha$	: coefficients of permeability for air and water
$K$	: Bulk modulus for the skeleton
$E$	: Young modulus for the skeleton
$\gamma$	: specific weight
$n$	: porosity of soil
$n_j$	: the normal vector
$\delta(x)$	: the Dirac delta function
$H(t)$	: the Heaviside step function
$s$	: the Laplace's transformation parameter
$\varepsilon$	: symbol for small values
$\theta_\alpha(x)$	: distribution function for parameter $\alpha$
$\hat{T}_i$	: traction induced by the fundamental solutions in the Laplace's transformation space
$\hat{Q}^\alpha$	: flux of phase $\alpha$ , induced by the fundamental solutions in the Laplace's transformation space
$c_{ij}$	: intermediate coefficients
$q_i^\alpha$	: the fluid volume fluxes for air and water

## References

1. I. D. Moldovan and T. D. Cao, "Hybrid-Trefftz Displacement Finite Elements for Elastic Unsaturated Soils," *International Journal of Computational Methods*, vol. 11, no. 2, p. 1342005, 2014.
2. M. Schanz, "Poroelastodynamics: Linear Models, Analytical Solutions, and Numerical Methods," *Applied mechanics reviews*, vol. 62, no. 3, p. 030803, 2009.
3. M. P. Cleary, "Fundamental solutions for a fluid-saturated porous solid.," *International Journal of Solids and Structures*, vol. 13, no. 9, pp. 785-806, 1977.
4. B. Gatmiri and E. Jabbari, "Time-domain Green's functions for unsaturated soils. Part I: Two-dimensional solution," *International Journal of Solids and Structures*, vol. 42, no. 23, pp. 5971-5990, 2005.
5. B. Gatmiri and E. Jabbari, "Time-domain Green's functions for unsaturated soils. Part II: Three-dimensional solution," *International Journal of Solids and Structures*, vol. 42, no. 23, pp. 5991-6002, 2005.

6. P. Maghoul, B. Gatmiri and D. Duhamel, "Boundary integral formulation and two-dimensional fundamental solutions for dynamic behavior analysis of unsaturated soils," *Soil Dynamics and Earthquake Engineering*, vol. 31, no. 11, pp. 1480-1495, 2011.
7. M. Schanz and P. Li, "Wave propagation in a 1-D partially saturated poroelastic column," *ZAMM-Journal of Applied Mathematics and Mechanics*, vol. 81, no. S3, pp. 591-592, 2001.
8. Ghorbani, J., M. Nazem, and J. P. Carter. "Numerical modelling of multiphase flow in unsaturated deforming porous media." *Computers and Geotechnics* 71 (2016): 195-206.
9. Igumnov, L. A., S. Yu Litvinchuk, A. N. Petrov, and A. A. Ipatov. "Numerically Analytical Modeling the Dynamics of a Prismatic Body of Two-and Three-Component Materials." In *Advanced Materials*, pp. 505-516. Springer, Cham, 2016.
10. Igumnov, L. A., A. N. Petrov, and I. V. Vorobtsov. "One-dimensional wave propagation in a three phase poroelastic column." *Key Engineering Materials* 685 (2016).
11. H. Wang and Q.-H. Qin, "Boundary integral based graded element for elastic analysis of 2D functionally graded plates," *European Journal of Mechanics-A/Solids*, vol. 33, pp. 12-13, 2012.
12. I. Ashayeri, M. Kamalian and M. Jafari, "Transient Boundary Integral Equation of Dynamic Unsaturated Poroelastic Media," in *Geotechnical Earthquake Engineering and Soil Dynamics IV*, 2008.
13. O. C. Zienkiewicz, Y. Xie, B. A. Schrefler, A. Ledesma and N. Bicanic, "Static and dynamic behaviour of soils: a rational approach to quantitative solutions. II. Semi-saturated problems," in *Proceedings of the Royal Society of London A: Mathematical, Physical and Engineering Sciences*, 1990.
14. D. G. Fredlund and H. Rahardjo, *Soil Mechanics for Unsaturated Soils*, John Wiley & Sons, 1993.
15. O.E. Lafe and H.-D. Cheng, "A perturbation boundary element code for steady state groundwater flow in heterogeneous aquifers," *Water Resources Research*, vol. 23, no. 6, pp. 1079-1084, 1987.
16. K. Sato and R. N. Horn, "Perturbation boundary element method for heterogeneous reservoirs: Part 1-Steady-state flow problems," *SPE Formation Evaluation*, vol. 8, no. 04, pp. 306-314, 1993.

17. I. Ashayeri, M. Kamalian, M. K. Jafari and B. Gatmiri, "Analytical 3D transient elastodynamic fundamental solution of unsaturated soils," *International Journal for Numerical and Analytical Methods in Geomechanics*, vol. 35, no. 17, pp. 1801-1829, 2011.
18. K.-V. Nguyen and B. Gatmiri, "Numerical implementation of fundamental solution for solving 2D transient poroelastodynamic problems," *Wave motion*, vol. 44, no. 3, pp. 137-152, 2007.
19. K. Wapenaar and J. Foklema, "Reciprocity theorems for diffusion, flow and waves," *TRANSACTIONS-AMERICAN SOCIETY OF MECHANICAL ENGINEERS JOURNAL OF APPLIED MECHANICS*, vol. 71, no. 1, pp. 145-150, 2004.
20. P. Li and M. Schanz, "Time domain boundary element formulation for partially saturated poroelasticity," *Engineering Analysis with Boundary Elements*, vol. 37, no. 11, pp. 1483-1498, 2013.
21. S. N. Atluri and T. Zhu, A new meshless local Petrov-Galerkin (MLPG) approach in computational mechanics, vol. 22, Computational mechanics, 1998.
22. B. Gatmiri, P. Delage and M. Cerrolaza, "UDAM: A powerful finite element software for the analysis of unsaturated porous media," *Advances in Engineering Software*, vol. 29, no. 1, pp. 29-43, 1998.

## Appendix A

It has been claimed that any variation in the parameters of the medium could be found in terms of variations of the state parameters. In this appendix it has been explained for different parameters. A dimensionless type of the state parameters could be defined:

$$\frac{P^a(x)}{P^c(0)} = \frac{P^a(0)}{P^c(0)} + \varepsilon \theta_a(x) \quad (\text{A-1})$$

$$\frac{P^w(x)}{P^c(0)} = \frac{P^w(0)}{P^c(0)} + \varepsilon \theta_w(x) \quad (\text{A-2})$$

$$\frac{\sigma'_{ij}(x)}{P^c(0)} = \frac{\sigma'_{ij}(x) - P^a(x)}{P^c(0)} = \frac{\sigma'_{ij}(x)}{P^c(0)} + \varepsilon \theta_\sigma(x) \quad (\text{A-3})$$

$$\frac{P^c(x)}{P^c(0)} = \frac{P^a(x) - P^w(x)}{P^c(0)} = \frac{P^a(0)}{P^c(0)} + \varepsilon \theta_a(x) - \frac{P^w(0)}{P^c(0)} - \varepsilon \theta_w(x) \quad (\text{A-4})$$

$$= 1 + \varepsilon (\theta_a(x) - \theta_w(x)) = 1 + \varepsilon \theta_c(x)$$

The state surface for the void ratio is [22]:



$$\frac{1+e(x)}{1+e(0)} = \exp(B(x)) \quad (\text{A-5})$$

Where:

$$B(x) = \frac{1}{(1-m)K_b P_{atm}^{1-m}} \left( a\sigma'(x) + bP^c(x) \left( 1 - \frac{\sigma'(x)}{\sigma_e} \right) \right)^{1-m} \quad (\text{A-6})$$

In which  $a$ ,  $b$ ,  $m$ ,  $K_b$  and  $P_{atm}$  are materials constants. Using (A-1) to (A-3) in (A-6):

$$B(x) = \frac{P^c(0)}{(1-m)K_b P_{atm}^{1-m}} \times \left( a \frac{\sigma'(0)}{P^c(0)} + b \left( 1 - \frac{\sigma'(0)}{\sigma_e} \right) + \varepsilon \left( a\theta_\sigma(x) + b \left( \theta_c(x) \left( 1 - \frac{\sigma'(0)}{\sigma_e} \right) \right) - \frac{P^c(0)}{\sigma_e} \theta_\sigma(x) \right) \right)^{1-m} \quad (\text{A-7})$$

Finally, using Taylor's expansion and dropping the infinitesimal terms, then replacing the result in (A-5):

$$1+e(x) = (1+e(0))(1+\varepsilon\theta_B(x)) \quad (\text{A-8})$$

$$\theta_B(x) = (m-1) \left( a\theta_\sigma(x) + b \left( \theta_c(x) \left( 1 - \frac{\sigma'(0)}{\sigma_e} \right) \right) - \frac{P^c(0)}{\sigma_e} \theta_\sigma(x) \right) \left( a \frac{\sigma'(0)}{P^c(0)} + b \left( 1 - \frac{\sigma'(0)}{\sigma_e} \right) \right)^{-m} \quad (\text{A-9})$$

The relationship between  $e$  and  $n$  (porosity) results in a similar equation for  $n$ :

$$n(x) = n(0)(1+\varepsilon\theta_n(x)) \quad (\text{A-10})$$

$$\theta_n(x) = \theta_B(x) \frac{1-n(0)}{n(0)} \quad (\text{A-11})$$

The water retention curve could be used to derive a similar equation for the saturation ratio:

$$Sr(x) = Sr(0)(1+\varepsilon\theta_{Sr}(x)) \quad (\text{A-12})$$

$$\theta_{Sr}(x) = \frac{\beta\theta_c(x)}{Sr(0)} \quad (\text{A-13})$$

Where  $\beta$  has been used to express the saturation ratio in terms of suction.

The air and water permeability could be explained in the same form:

$$K_a(x) = K_a(0)(1+\varepsilon\theta_{K_a}(x)) \quad (\text{A-14})$$

$$\theta_{K_a}(x) = E_k \left( \theta_B(x) \frac{1+e(0)}{e(0)} - \theta_{Sr}(x) \frac{Sr(0)}{1-Sr(0)} \right) \quad (\text{A-15})$$

$$K_w(x) = K_w(0)(1 + \varepsilon \theta_{K_w}(x)) \quad (\text{A-16})$$

$$\theta_{K_w}(x) = 3.5 \theta_B(x) \frac{Sr(0)}{1 - Sr_u} \quad (\text{A-17})$$

The constants have been defined later in the paper.

The tangential elastic module could be evaluated using the Kondner's hyperbolic law for unsaturated soils [22]:

$$E_t(x) = (E_e(x) + E_s(x))(1 - R_f S(x)) \quad (\text{A-18})$$

$$S(x) = \frac{\sigma_1 - \sigma_3}{(\sigma_1 - \sigma_3)_{ult}} = S(0) (1 + \varepsilon \theta_s(x)) \quad (\text{A-19})$$

$$E_e(x) = K P_{atm} \left( \frac{\sigma_3}{P_{atm}} \right)^n \quad (\text{A-20})$$

$$E_s(x) = m_1 P^c \quad (\text{A-21})$$

$$E_t(x) = E_t(0) (1 + \varepsilon \theta_{E_t}(x)) \quad (\text{A-22})$$

$$\theta_{E_t}(x) = \frac{n E_e(0)}{E_e(0) + E_s(0)} \theta_{\sigma_3}(x) + \frac{E_s(0)}{E_e(0) + E_s(0)} \theta_c(x) - \frac{R_f S(0)}{1 - R_f S(0)} \theta_s(x) \quad (\text{A-23})$$

The bulk module could be found using the Kondner's hyperbolic law and the state surface which has been stipulated previously [22]:

$$K(x) = \frac{K_b}{P_{atm}^{1-m} \left( a - \frac{b}{\sigma_e} P^c(x) \right)} B(x)^m \quad (\text{A-24})$$

Using the spatial assessment for  $B$  and  $P^c$  and omitting the terms that includes second and higher orders of  $\varepsilon$  leads to:

$$K(x) = K(0)(1 + \varepsilon \theta_K(x)) \quad (\text{A-25})$$

$$\theta_K(x) = \frac{m \left( a \theta_{\sigma_e}(x) + b \left( \theta_c(x) \left( 1 - \frac{\sigma'(0)}{\sigma_e} \right) \right) - \frac{P^c(0)}{\sigma_e} \theta_{\sigma_e}(x) \right)}{\left( a \frac{\sigma'(0)}{P^c(0)} + b \left( 1 - \frac{\sigma'(0)}{\sigma_e} \right) \right)} + \frac{b P^c(0)}{\sigma_e \left( a - \frac{b P^c(0)}{\sigma_e} \right)} \theta_c(x) \quad (\text{A-26})$$

Finally using the known relations to convert the bulk and the elastic moduli to the Lamé's coefficients leads to:

$$\lambda(x) = \lambda(0) (1 + \varepsilon \theta_{\lambda}(x)) \quad (\text{A-27})$$

$$\theta_{\lambda}(x) = \frac{3K(0) \left( -6K(0)E_t(0)\theta_{E_t}(x) + (E_t(0)^2 - 6K(0)E_t(0) + 27K(0)^2) \theta_K(x) \right)}{(9K(0) - E_t(0))^2} \quad (\text{A-28})$$

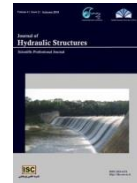
$$\mu(x) = \mu(0) (1 + \varepsilon \theta_{\mu}(x)) \quad (\text{A-29})$$

$$\theta_{\mu}(x) = \frac{3K(0) E_t(0) (9K(0) \theta_{E_t}(x) - E_t(0) \theta_K(x))}{(9K(0) - E_t(0))^2} \quad (\text{A-30})$$



© 2018 by the authors. Licensee SCU, Ahvaz, Iran. This article is an open access article distributed under the terms and conditions of the Creative Commons Attribution 4.0 International (CC BY 4.0 license) (<http://creativecommons.org/licenses/by/4.0/>).





## Evaluating performance of meta-heuristic algorithms and decision tree models in simulating water level variations of dams' piezometers

Rezvan Salajegheh<sup>1</sup>  
Amin Mahdavi-Meymand<sup>2</sup>  
Mohammad Zounemat-Kermani<sup>3</sup>

### Abstract

Monitoring the seepage, particularly the piezometric water level in the dams, is of special importance in hydraulic engineering. In the present study, piezometric water levels in three observation piezometers at the left bank of Jiroft Dam structure (located in Kerman province, Iran) were simulated using soft computing techniques and then compared using the measured data. For this purpose, the input data, including inflow, evaporation, reservoir water level, sluice gate outflow, outflow, dam total outflow, and piezometric water level, were used. Modeling was performed using multiple linear regression method as well as soft computing methods including regression decision tree, classification decision tree, and three types of artificial neural networks (with Levenberg-Marquardt, particle swarm optimization, PSO, and harmony search learning algorithms, HS). The results of the present study indicated no absolute superiority for any of the methods over others. For the first piezometer the ANN-PSO indicates better performance (correlation coefficient,  $R=0.990$ ). For the second piezometer ANN-PSO shows better results with  $R=0.945$ . For the third piezometers MLR with  $R=0.945$  and ANN-HS with  $R=0.949$  indicate better performance than other methods. Furthermore, Mann-Whitney statistical analysis at confidence levels of 95% and 99% indicated no significant difference in terms of the performance of the applied models used in this study.

**Keywords:** Data driven models; dam surveillance; soft computing, heuristic algorithms, dam engineering.

Received: 8 December 2018; Accepted: 26 December 2018

### 1. Introduction

Seepage is one of the major issues in various engineering levees and dams, so that in most of

<sup>1</sup> Department of Civil Engineering, Baft Branch, Islamic Azad University, Baft, Iran.

<sup>2</sup> Department of Water Engineering, Shahid Bahonar University of Kerman, Kerman, Iran

<sup>3</sup> Department of Water Engineering, Shahid Bahonar University of Kerman, Kerman, Iran. Email address: zounemat@uk.ac.ir, orcid.org/0000-0002-1421-8671. (**Corresponding author**)



the cases, the problems related to these structures are associated, either directly or indirectly, with seepage; therefore, monitoring and identifying the seepage behavior play important role in the safety and security of the engineering levees and dams [1-3]. Piezometric devices installed and used in certain sections of the dam to measure the seepage based on water level. In relation to monitoring and investigating the issue of seepage, numerous studies have been conducted to date, most of which have been focused on investigating the seepage rate and seepage monitoring in different sections of dams [4]. Although concrete dams are considered impenetrable, they have been encountering serious seepage-related problems due to their specific construction conditions [2]. In practice, in order to monitor seepage, some piezometers are improvised in certain parts of the dam [5, 6].

In addition, some other physical methods (drilling boreholes and using dye trace test) as well mathematical models and numerical methods can be also used to identify the seepage path and solve the seepage path problems [7].

In recent decades, regarding the successful application of data-based methods for simulating various kinds of engineering problems, the soft computing methods have been widely used for solving the dam engineering problems. Several studies have evaluated the performance of these methods in predicting the dam location variation, dam section optimization, and fracture in arch dams [1].

In order to predict water level in piezometers, Tayfur et al. [8] used ANN, and considered the upstream and downstream water levels as the input data. Gholizadeh and Seyedpoor [9] used neural network and PSO (particle swarm optimization) and GA (genetic algorithm) to show the impact and importance of soft computing in achieving the optimal arch dam design geometry, which can provide stability of the dam against natural pressures.

Zhou et al. [5] used a compound method, consisted of orthogonal design (OD), ANN, FE, and GA, for modelling the leakage and seepage problems. Zhou et al. [5] used BPNN (back-propagation neural network) to depict the implicit map of environmental parameters in order to investigate the impermanent seepage flow's response at dam monitoring points. Stojanovic et al. [10] presented a self-tuning system for dam behavior modelling based on ANN with genetic algorithm (ANN/GA) compared to MLR, the results of which implied superiority of the ANN-GA method over other methods. Xiang et al. [4] used PSO algorithm to optimize the seepage model parameters, the results of which indicated the higher precision and accuracy of this method compared to previous statistical methods.

Nourani et al. [11] used neural network and ANFIS (adaptive network-based fuzzy interference system) to investigate contamination concentration over time in porous environments. Studies have shown that the complexity of the underground water flow and transmission of contamination have caused the use of black box methods, such as neural networks and ANFIS.

The present study is aimed to simulate the water level in piezometers of Jiroft double-curvature arch dam in Kerman province, Iran, using three samples of MLP artificial neural networks (with Levenberg-Marquardt training algorithm as well as PSO and HS algorithms), and to compare the results obtained from the MLR, classification decision tree, and regression decision tree methods. To best of the authors' knowledge, assessing the performance of classification regression tree, regression decision tree, ANN-PSO and ANN-HS to predicting the water level in piezometers has not been studied in past researches. Hence, the application of these soft computing models is the novelty and the contribution of this study.

## 2. Materials and methods

### 2.1. Case study and dataset

Jiroft dam is a double-curvature arch concrete dam operated in 1991, which is located in the study zone of Hamun-e-Jaz Murian at the central basin and is fed by Halilriver in the northeast of the Jiroft city in the narrow valley of Narab (Figure 1). This dam has been constructed with the aim of generating electricity and supplying the water requirement of agricultural and environmental sectors; besides, it is also used as a secondary target for supplying drinking water. The electricity generation capacity of this dam is 80 GW, and it features reservoir volume of 336 m<sup>3</sup>, dam height of 128 m, height above its foundation of 132 m, crest length of 250 m, and lake length of 12 km; also, the spillway is of middle and surface sluice type [12].

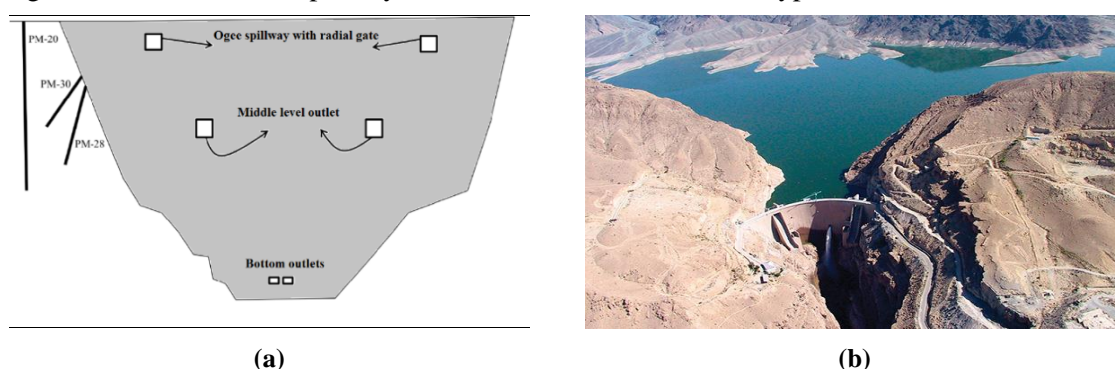


**Figure 1. (a) Aerial image of Jiroft double-curvature arch concrete dam in Kerman province, Iran; (b) Schematic image of cross section of dam and location of piezometers used in this study, which are situated at left bank retain wall in the body and rock (rock is the foundation) of the dam.**

Jiroft dam has about 22 and 19 piezometers in the right and left banks, respectively. We could access to the data of three of these piezometers (see Figure 1). So, in order to model the water level behavior caused by seepage in Jiroft concrete dam, the data related to the piezometers 20, 28, and 30 situated at the left bank retain wall was used. Piezometer 20 is located at the abutment (support), and piezometers 28 and 30 are situated in the dam body. The obtained data on the water level of the piezometers were used as the output parameter of each model. The water level in these piezometers was measured once a month since 1994 to 2001; also, the input vector of each model was developed based on the monthly data, including evaporation rate from water surface (mm), reservoir inflow (m<sup>3</sup>/s), reservoir water level (m), sluice gate outflow rate (MCM), Intake outflow (MCM), as well as total outflow rates (MCM) in the given period. It should be noted that the reservoir inflow and evaporation rates were taken from the nearest station to the dam site (Kenrouye Station) at a 12km distance. The number of datasets for each piezometer is 192.

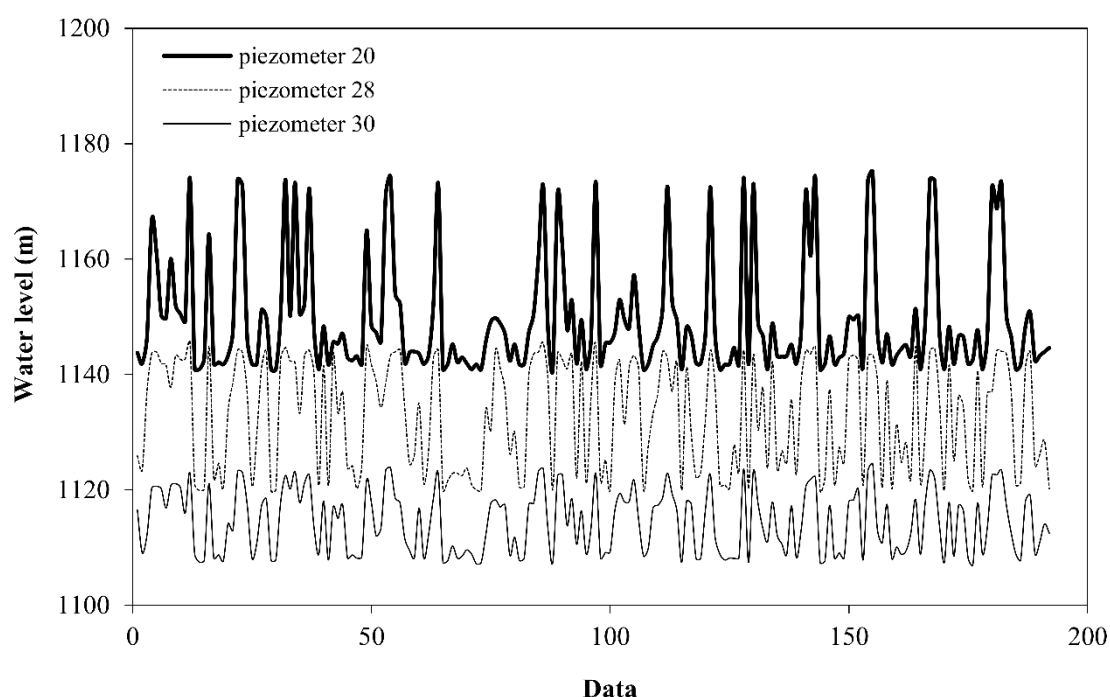


**Figure 2. Historical variations of water level in the three studied piezometers in this research.**

Figure 2 shows the historical variations of water level in the three piezometers. As could be expected from the location of piezometers (see Figure 1), the average values of surface water level in Piezometer 20 is more than the other two piezometers. Also total variations in Piezometer 28 is less than the other two piezometers. In this study the hold-out method is used as the method of sampling. In this respect, datasets are divided into two categories of training (80%) and testing (20%) phases for modelling implementation. Training data are used for the learning process of the models, while testing data are used to evaluate the performance of the models. A summary of the statistical characteristics of the measurement data of the output vector (reservoir water level variations) and input vector is provided in Tables (1) and (2).

**Table 1- Statistical analysis of piezometers' water level data used in the present study**

Piezometer	Max (m)	Min (m)	Ave (m)	SD	CV	SK
20	1175.1	1140.9	1149.657	10.235	0.008	1.472
28	1145.55	1119.84	1132.954	9.442	0.00	-0.150
30	1124.48	1107.07	1114.459	5.473	0.004	0.175

**Table 2 - Statistical analysis of input parameters of data driven models**

Parameter	Max	Min	Ave	SD	CV	SK
Input discharge to the reservoir (m <sup>3</sup> /s)	150.769	0.038	8.111	17.871	2.203	4.500
Evaporation (mm)	541	54.5	264.480	136.429	0.515	0.175
Water level of the reservoir (m)	1183.52	1120.99	1153.845	17.669	0.015	0.216
Sluice gate outflow rate (MCM)	110.75	0	5.222	20.520	3.929	4.457
Intake outflow(MCM)	28.94	0	6.180	5.219	0.844	1.420
Total outflow rate(MCM)	461.498	0.942	24.255	49.598	2.044	6.268

## 2.2 Data driven models used in this study

### 2.2.1 MLR model

Multiple (multivariate) linear regression is a method in which two or more independent variables contribute to the variations of a variable, and is one of the most effective prediction methods; thus, it is widely used in researches that are aimed to investigate and predict a specific phenomenon. In such researches, regarding the independent variables, a regression relation is extracted, based on which the dependent variable is predicted. The general form of the equation is as follows [1, 10]:

$$WL = \beta_0 + \beta_1 u_1 + \beta_2 u_2 + \dots + \beta_N u_N \quad (1)$$

where, WL stands for the piezometer's water level (dependent parameter) and  $\beta_i$  represents coefficients of the independent parameters and is estimated by sum of square error, and  $u_i$  indicates the input variable vector [13].

### 2.2.3 Decision tree models

A decision tree represents a structure in which the leaves indicate classes (categories), and the branches indicate combinations of the attributes resulting in these classes. Decision trees classify the samples by sorting them in the tree from the root toward leaf nodes. Each internal node in the tree tests an attribute of the sample, and each branch coming out of that node corresponds to a possible value for that attribute. Each leaf node represents a class. Each sample begins from the root and after testing the attribute in this node, moves in the corresponding branch with regard to the attribute, and finally is placed in an appropriate class. This process is repeated regressively for each sub tree. The regression is completed when further separation is not useful anymore or a classification cannot be applied to all the samples existing in the obtained subset [14, 15].

Decision trees are capable to generate attributes from the relations in a dataset, which are perceivable for human and can be used for classification and prediction. Decision trees are divided into four main groups, including classification trees, regression trees, classification-regression trees, and cluster trees. In the present study, two types of these trees, namely classification and regression trees are used [15-17].

#### 2.2.3.1 Regression decision tree (RDT)

Regression decision trees were first introduced by Breiman et al. [14] as a statistical model. These trees are based on the regression divisions of the training data in groups of similar cases.



The output of a medium decision tree is the observed output variable in each group. When there is more than one predictor, the best separator (distinction) point is calculated for each of them, and the factor resulting in the highest error reduction rate is selected; therefore, the inappropriate (irrelevant) predictors are automatically eliminated by the algorithm, so that error reduction for a separator in a low-importance predictor will be generally less than that in a more useful one. Other dominant characteristics of the regression decision trees include [17] : they are robust against outliers, require little data preprocessing, can handle numerical and categorical predictors, and are appropriate for modelling nonlinear relations, as well as interaction among predictors.

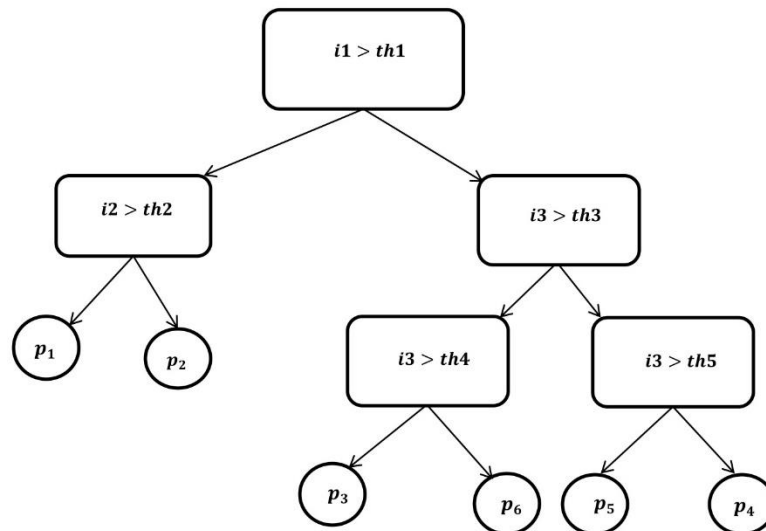


Figure 3. Schema of structure of a regression decision tree

Figure 3 shows a profile of a regression decision tree [15] . In order to improve precision of prediction, it calculates the re-substitution error, test sample error, and cross-validation error. The error is estimated by applying the data used for determining the structure of the predictor  $p$  and is calculated as the MSE (mean square error).

$$E(p) = \frac{1}{N} \sum_{i=1}^N (u_i - p(v_i))^2 \quad (2)$$

Where,  $(u_i, v_i)$  indicates training samples, and  $i=1,2,3,\dots,N$  is divided into  $K$  subsamples in order to estimate the re-substitution error of sample  $X$  with size of  $N$ . Also,  $X_1, X_2, \dots, X_K$  with approximate size of  $N_1, N_2, \dots, N_K$  from  $X-X_K$  subsamples are used for making the predictor  $p$ . Finally, this error of the sample  $X_K$  is calculated using the following formula:

$$E^{cv}(P) = \frac{1}{N_k} \sum_k \sum_{(u_i, v_i) \in X_k} (v_i - p^{(k)}(u_i))^2 \quad (3)$$

Where,  $(p^k u_i)$  is calculated from the subsample  $x-x_k$ . The test sample error is divided into subsamples  $x_1$  and  $x_2$  with size of  $N_1$  and  $N_2$ , and then is calculated using the following formula:

$$E^{ts}(p) = \frac{1}{N_2} \sum_{(u_i, v_i) \in X_2}^N (v_i - p_{ui})^2 \quad (4)$$

where,  $x_2$  is a subsample that is not used in the prediction structure.

Finally, the output of each decision tree is calculated via the following formula:

$$R(t) = \frac{1}{N_w(t)} \sum_{i \in t} w_i f_i (u_i - \bar{v}(t))^2 \quad (5)$$

Where,  $N_w(t)$  is the weight of data at  $t$ ,  $w_i$  is the value of the weighting variable for case  $i$ ,  $f_i$  is the value of the frequency variable,  $v_i$  is the value of the response variable, and  $\bar{v}(t)$  is the weighted mean for node  $t$ .

### 2.2.3.2 Classification decision tree (CDT)

Classification decision trees are used to predict discrete data (Figure 4). In order to have a better classification tree, the classification process must have error freedom as much as possible. This means that final nodes of the tree should be as homogenous as possible regarding the predicted variable. For this purpose, a step-wise algorithm creates an optimal classification of the training data, in which both categorical and prediction variables are known and clear. At each step, all of the possible branches are tested and compared based on each explanatory variable. And finally, the selected branch introduces the optimal subset [16, 18, 19].

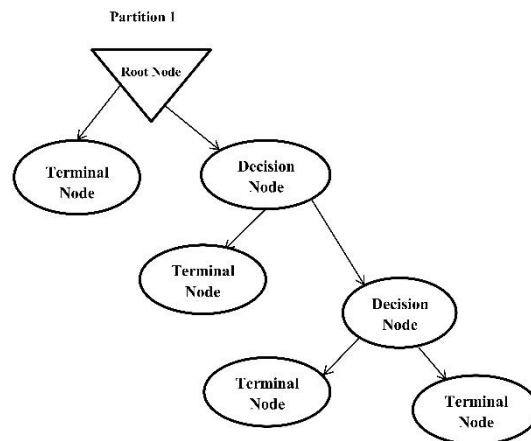


Figure 4. Schema of a classification decision tree

Since various indices and methods have been proposed so far for determining the decision tree, accordingly various algorithms have been introduced as well, the most important of which is CART (classification and regression tree) algorithm that has been designed for quantitative variables, but meanwhile it can be used for any type of variable. This algorithm was first introduced by Breiman et al. [14]. In this algorithm, various indices are used as criteria for selecting the variables. One of these indices is the Gini Index (GI), the advantage of which over other indices is its higher computation speed. In the present study, the CART algorithm and GI were used for classifying and predicting the water level in piezometers [19].

$$GINI_{split} = \sum_{i=1}^2 \frac{N_i}{N} GINI_i \quad (6)$$

$$GINI_i = \sum_{j=1}^k (1 - p_j^2) \quad (7)$$

Where,  $GINI_i$  is the GINI index of the child node  $i$ ,  $N_i$  is the number of samples at the child node  $i$ ,  $N$  is the number of samples at the parent node,  $P_j$  is the probability of class  $j$  at node  $i$ , and  $k$  is the number of classes.

### 2.2.3 Artificial neural networks (ANNs)

ANNs, with considerable ignorance, can be called the electronic models of the human brain's neural structure. In fact, the aim of creating a software neural network is, rather than simulating the human brain, to create a mechanism for solving the engineering problems inspired by the behavioral pattern of biological networks. These networks are capable to distinguish between the input patterns; thus, they can be used in a wide range of complex problems, including recognition of patterns, nonlinear models, classifications, etc. ANNs are divided into two main groups, namely recurrent networks, in which the loop occurs, and feed-forward neural networks, the structure of which lacks loops. Selecting the network's structure depends on the learning algorithm used for training of the network. A specific type of neural networks, known as FNN 3-layer neural network, has been widely used for solving many of the civil engineering and water engineering problems[1 , 20].

#### 2.2.3.1 Back propagation feed forward neural network

There are various types of neural networks, the most important of which is the back propagation feed forward neural networks (BPFNN). Similar to other types of neural network, FNNs are composed of simple components, which are called neurons. Neurons are located in layers, and neurons of the adjacent layers are interconnected to each other via connectors of an independent unit (synapses), which transfer the information from one neuron to other ones. The input data are stored in neurons of the first layer (input layer), and the outputs are displayed by neurons of the last layer (output layer). All the layer located between the input and output layers are known as the hidden layers (Honric, 1991).

The activation function is associated with layers, and its role is to scale and classify the output data of the layers. The most common types of activation functions include linear and sigmoid types. The linear activation functions are represented by the following general form:

$$f(y) = y \quad (8)$$

Two common types of sigmoid activation functions, which are used in these networks, include hyperbolic tangent function and logistic function.

$$f(0) = \frac{1}{1 + e^{-y}} \quad (9)$$

$$f(y) = \frac{1 - e^{-y}}{1 + e^y} \quad (10)$$

The output of a neuron in the hidden layers can be such as the following pattern:

$$\text{Output} = f(y) \quad (11)$$

Where  $y = \sum_{i=1}^k w_i x_i + b$ ,  $x_1, x_2, \dots, x_k$  are the input signals,  $w_1, w_2, \dots, w_k$  are the neurons' weights and  $b$  is the bias component. Figure (5) shows an FNN with 3 layers and  $S$  neurons in the input layer. The inputs are  $x=(x_1, x_2, \dots, x_k)$ , which are collected at the hidden nodes along with weights. At the nodes, first, the signal is collected and then a nonlinear function is applied (e.g. hyperbolic tangent); finally, the output  $y$  appears under a linear function at the output nodes.

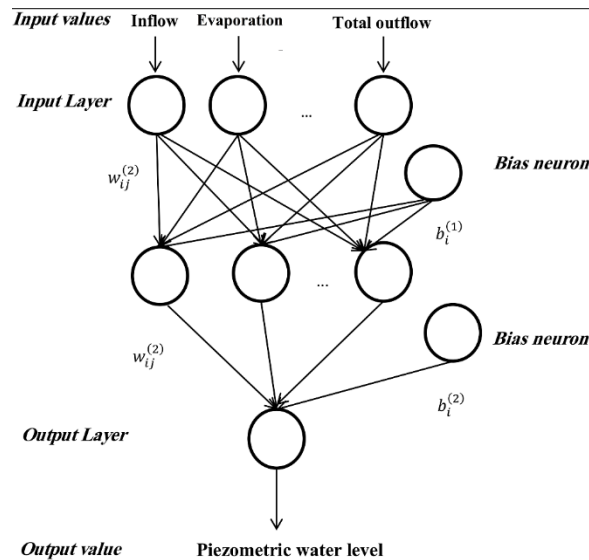


Figure 5. Three-layer neural network used in the present study

$$y = \sum_{i=1}^k w_{ij}^{(2)} \frac{1}{1 + e^{-(\sum_{j=1}^s x_j w_{ij}^{(1)} + b_i^{(1)})}} + b_i^{(2)} \quad (12)$$

where,  $s$  is the number of inputs,  $k$  is the number of hidden neurons,  $x_j$  indicates  $j$  input elements,  $w_{ij}^{(1)}$  is the weight of the first layers between  $i$  hidden neurons and  $j$  inputs,  $w_{ij}^{(2)}$  is the weight of the second layer between  $i$  hidden neurons and the output neuron,  $b_i^{(1)}$  is the base weight for  $i$  hidden neurons, and  $b_i^{(2)}$  is the base weight for the output neurons [1,21].

## 2.2.4 Optimization methods

Optimization is indeed a method for utilizing the linear and nonlinear capability of the formulas in order to solve a wide range of problems and analyze the solutions [22]. In the present study, in order to optimize the weight values of the neurons of the ANN, the Levenberg-Marquardt mathematical optimization method as well as PSO and HS meta-heuristic optimization methods was used.

### 2.2.4.1 Levenberg-Marquardt mathematical algorithm

Levenberg-Marquardt algorithm is a method to find the minimum of a multivariate nonlinear

function, which is used as a standard method for solving the least square problem for nonlinear functions. It is widely used in FNNs in order for reducing the errors by point reduction of the error curve's slope [23-25].

Due to its effective role in accurate calculation of the weights' error, this algorithm has been considered and investigated as the most well-known and prominent training structure, and is currently used for generalizing the delta rule (variations) in nonlinear activation functions and multi-layer networks. In Marquardt algorithm, the error function is minimized, while the size of the computational steps is small; accordingly, in order to reassure accuracy of the linear approximations, this objective was accomplished by the following modified error function [22].

$$E = \frac{1}{2} \left( e_{(j)} + \frac{\partial e_k}{\partial w_i} (w_{(j+1)} - w_{(j)}) \right)^2 + \lambda (w_{(j+1)} - w_{(j)})^2 \quad (13)$$

Where,  $\lambda$  is the parameter representing the step size, the minimum error, with regard to  $w_{(j+1)}$  is expressed as following:

$$W_{(j+1)} = W_{(j)} - (Z^T Z + \lambda I)^{-1} Z^T e_j \quad (14)$$

High values of  $\lambda$  cause declination of the standard gradient, and its lower value inclines toward Newton method.

#### 2.2.4.2 PSO algorithm

PSO algorithm was created by Kennedy & Eberhart [26] based on the collective movement of birds or a group of fish. PSO is an optimization sample capable to model the human population for processing the science, which is rooted in two main components of methodology, namely artificial life (such as groups of birds, schools of fish) and evolutionary counting (evolutionary computations). PSO algorithm is based on the assumption of the potential of movement in a space full of high-speed particles toward the optimal solution. It is a populated search method for optimizing the nonlinear functions [27]. Furthermore, PSO extracts the best cooperation status, and uses it for optimizing the engineering problems. The particles simply follow the set of predetermined roles. PSO calculates the particles based on the performance capability, and then selects the particle with the best solution. The particle with best capability is selected as the trainer; subsequently, all the particles are trained by the selected particles. No two particles are similar, and instead they utilize other particles' attributes to improve their own performance [28].

For each particle, two values of position and speed is defined, which are modeled by a location vector and a speed vector, respectively. These particles move repeatedly in the n-dimensional space of the problem. Dimensions of the problem are determined by the number of parameters of the problems. The general form of the algorithm's equation is represented below [29]:

$$v_{ij}(t'+1) = wv_{ij}(t') + c_1\gamma_1(p_{ij}(t') - x_{ij}(t')) + c_2\gamma_2(p_{gi}(t') - x_{ij}(t')) \quad (15)$$

$$x_{ij}(t'+1) = x_{ij}(t') + v_{ij}(t'+1) \quad (16)$$

Where  $j$  is the number of dimensions,  $i$  is the number of particles,  $t'$  is the number of repetitions,  $w$  is the inertia weight,  $\gamma_1$  and  $\gamma_1$  are random numbers in the range of  $[0,1]$ ,  $c_1$  and  $c_2$  are constant acceleration in the range of  $[0,2]$ , and  $v_{ij}$  is usually limited to a certain range.

$v_{ij} \in [-v_{max}, v_{max}]$ , and if the search space is limited to  $[-x_{max}, x_{max}]$ , then  $v_{max} = kx_{max}$  with  $0.1 \leq k \leq 1$ . Also,  $p_{ij}(t) - x_{ij}(t)$  represents the distance between the current location and optimal location of the  $i^{th}$  particle, and  $p_{ij}(t) - x_{ij}(t)$  indicates the distance between the current location and the optimal location of the  $i^{th}$  particle in the group.

#### 2.2.4.3 HS (harmony search) algorithm

Harmony search, which is a heuristic algorithm imitating the musicians' structure for finding the best harmony, is widely used for solving the complex problems that cannot be solved by old methods. It has several advantages over previous optimization methods. It applies the last absolute mathematical features such as differentiability, continuity, and convexity [30]. According to the definition presented by Geem et al. [31], the HS algorithm is based on the minimum mathematical requirements and begins from probable random search; therefore, it does not require much secondary information. The vector introduces the final solution with regard to all the resulted vectors.

In HS algorithm, the musician looks for the best harmony that has been arranged aesthetically. Accordingly, the optimizer algorithms look for the best status with regard to the objective function. Each musician is associated with the decision variable, and the musical instruments' beats are sorted based on the importance of the decision variable. The musical harmony at a certain time is associated with the leader vector in a certain repetition. The hearer's enjoyment is the final objective (output of the harmony). Furthermore, just like the stepwise improvement of the musical harmony, the solution vector in the algorithm moves toward the optimal solution in each repetition [32].

Each musician has three options: (1) playing each pitch based on his own memory, (2) playing something similar to the given music, and (3) playing a new or random note. These explanations are generally expressed by the following formula [33]:

$$x_{new} = x_{old} + b_p \times (2rand - 1) \quad (17)$$

$$x(i) = x_{min}(i) + (x_{max}(i) - x_{min}(i)) \times rand \quad (18)$$

Where,  $x_{new}$  is the new solution after a certain beat,  $x_{old}$  is the solution from memory of harmony,  $rand \in [0,1]$ ,  $b_p$  is the bandwidth vector,  $i$  is equal to 3, and  $x_{min}(i)$  and  $x_{max}(i)$  are the minimum and maximum values of  $i$ , respectively.

### 3. Implementing and executing the model

#### 3.1 Preparing data

To prepare the data, the entire data were divided into two groups, namely training data (80%) and test data (20%). The input data, including inflow, reservoir water level, sluice gate outflow, intake flow rate, dam total outflow were used to predict the piezometric water level. It should be noted that in order to challenge the models in the previous data unavailability conditions, simulation was performed based on merely the data of each month; since, in case of desirable evaluation of the models, it would be possible to use them for any time period regardless of the physical performance and historical data of the dam's piezometers and merely based on the input data of that month.

### 3.2 Evaluating model's performance

In the present study, in order for evaluating the performance of the used models, several statistical indices, including MSE (mean square error), MAE (mean absolute error), and RMSE (root mean square error), and correlation coefficient (R) were used.

$$R = \frac{\sum_{i=1}^{N_o} (y_i - \bar{y})(m_i - \bar{m})}{\sqrt{\sum_{i=1}^{N_o} (y_i - \bar{y})^2 \sum_{i=1}^{N_o} (m_i - \bar{m})^2}} \quad (19)$$

$$MSE = \frac{1}{N_o} \sum_{i=1}^{N_o} (y_i - m_i)^2 \quad (20)$$

$$MAE = \frac{1}{N_o} \sum_{i=1}^{N_o} |y_i - m_i| \quad (21)$$

$$RMSE = \sqrt{\frac{1}{N} \sum_{i=1}^{N_o} (y_i - m_i)^2} \quad (22)$$

where,  $y_i$  and  $m_i$  represent the network's output and measured data for  $i$  elements, respectively, and  $\bar{y}$  and  $\bar{m}$  represent the mean of parameters, and  $N_o$  indicates the number of them.

### 3.3 Setting up the models

In the present study, in order to predict the water level in piezometers 20, 28, and 30, the 3-layer neural network, regression decision tree, classification decision tree, and multivariate linear regression were used. Precision of any model is directly dependent on the input parameters; therefore, the input parameters included the monthly gathered data, including: evaporation, inflow, reservoir water level, sluice gate outflow, outflow, dam total outflow, and read water level of piezometers. The training data were considered as the basis of modelling for all the models. In order for modelling using neural networks, several neural networks with different architectures were taken into consideration. By considering different numbers of neurons in the network, the best state of the network was identified. Finally, by considering three neurons in the middle layer, the intended neural network was built, and performance of different transmission functions was compared. The neural network's parameters (weights and biases) were optimized using LM, PSO and HS algorithms. By initiating the weights and biases, the final values of these coefficients were extracted using the above-mentioned algorithms, and then these extracted values were used for modelling the neural network. The results obtained for different transmission function, considering three neurons in the middle layer, were evaluated so that these methods can be compared in the same conditions. In order for modelling via classification and regression decision trees, the intended models were constructed using the training data as the inputs; then, the performance of these models was evaluated using the test data.

## 4. Results and discussion

Investigating the results obtained from modelling the ANNs shows that in terms of simulation all the three piezometers, the neural network with 5 neurons exhibited the best performance. However, performance of the transmission function in the hidden and output layers was different for each piezometer, the results of which are summarized in Table (3).



**Table 3- Results of modelling ANN-LM in order to simulate water level variations of piezometers of Jiroft Dam**

Piezometer	ANN-LM	Train				Test			
		MSE (m <sup>2</sup> )	MAE (m)	RMSE (m)	R	MSE (m <sup>2</sup> )	MAE (m)	RMSE (m)	R
20	Tansig-Tansig	2.593	1.227	1.610	0.987	7.321	1.805	2.706	0.967
	Tansig-Logsig	2.646	0.982	1.627	0.987	4.113	1.580	2.028	0.988
	<b>Logsig-Tansig</b>	<b>2.712</b>	<b>1.016</b>	<b>1.647</b>	<b>0.987</b>	<b>4.077</b>	<b>1.667</b>	<b>2.019</b>	<b>0.991</b>
	Logsig-Logsig	1.964	0.872	1.401	0.990	10.029	1.656	3.167	0.960
28	Tansig-Tansig	5.596	1.589	2.365	0.968	20.565	3.550	4.535	0.911
	Tansig-Logsig	3.695	1.372	1.922	0.979	21.132	3.492	4.597	0.918
	<b>Logsig-Tansig</b>	<b>3.251</b>	<b>1.151</b>	<b>1.803</b>	<b>0.982</b>	<b>16.542</b>	<b>3.040</b>	<b>4.067</b>	<b>0.921</b>
	Logsig-Logsig	4.579	1.466	2.139	0.974	19.887	3.336	4.459	0.897
30	Tansig-Tansig	1.010	0.711	1.005	0.983	7.4383	2.063	2.727	0.918
	Tansig-Logsig	0.956	0.730	0.978	0.984	7.009	1.970	2.647	0.921
	<b>Logsig-Tansig</b>	<b>1.046</b>	<b>0.746</b>	<b>1.023</b>	<b>0.982</b>	<b>6.780</b>	<b>2.035</b>	<b>2.604</b>	<b>0.935</b>
	Logsig-Logsig	1.129	0.792	1.063	0.981	7.863	2.051	2.804	0.922

For the piezometer 20, the transmission function log sigmoid for the hidden layer tan sigmoid for the output layer exhibited the best performance; however, for the piezometer 28, the transmission function of tan sigmoid for both hidden and output layers had the best performance. Besides, in the piezometer 30, again both hidden and output layers with transmission function tan sigmoid had the best solutions. Since the use of 3 neurons in the hidden layer in the neural network resulted in the best performance, in the combination of the neural network with PSO and HS algorithm, 3 neurons were used in the hidden layer as well, the results of which are presented in Tables (4) and (5). Here, again the transmission functions of the hidden and output layers were different for each piezometer. In the neural network-PSO algorithm combination, piezometer 20 with transmission function of tan sigmoid for the hidden layer and log sigmoid for the output layer, piezometer 28 with log sigmoid transmission function for both hidden and output layers, and piezometer 30 with tan sigmoid transmission function for both layers exhibited the best performance. Moreover, in the combination of the neural network with HS algorithm, piezometer 20 with transmission function of tan sigmoid in the hidden layer and log sigmoid in the output layer, piezometer 28 with tan sigmoid transmission function for both hidden an output layers, and piezometer 30 transmission function of log sigmoid for the hidden layer and tan sigmoid for the output layer had the best solutions.



**Table 4- Results of combining ANN-PSO in order to simulate water level variations of piezometers of Jiroft Dam**

Piezometer	ANN-PSO	Train				Test			
		MSE (m <sup>2</sup> )	MAE (m)	RMSE (m)	R	MSE (m <sup>2</sup> )	MAE (m)	RMSE (m)	R
20	Tansig-Tansig	4.926	1.567	2.219	0.976	3.614	1.494	1.901	0.991
	<b>Tansig-Logsig</b>	<b>4.621</b>	<b>1.300</b>	<b>2.149</b>	<b>0.977</b>	<b>2.533</b>	<b>1.194</b>	<b>1.592</b>	<b>0.990</b>
	Logsig-Tansig	9.422	2.275	3.069	0.953	8.796	2.355	2.966	0.974
	Logsig-Logsig	4.739	1.457	2.177	0.977	3.965	1.477	1.991	0.992
28	Tansig-Tansig	4.599	1.421	2.145	0.974	13.455	2.898	3.668	0.938
	Tansig-Logsig	4.721	1.473	2.173	0.973	16.013	3.105	4.002	0.913
	Logsig-Tansig	5.701	1.656	2.387	0.968	14.379	3.090	3.792	0.930
	<b>Logsig-Logsig</b>	<b>5.611</b>	<b>1.511</b>	<b>2.369</b>	<b>0.968</b>	<b>11.549</b>	<b>2.736</b>	<b>3.398</b>	<b>0.945</b>
30	<b>Tansig-Tansig</b>	<b>3.475</b>	<b>1.424</b>	<b>1.864</b>	<b>0.956</b>	<b>3.253</b>	<b>1.374</b>	<b>1.803</b>	<b>0.948</b>
	Tansig-Logsig	3.505	1.486	1.872	0.943	3.626	1.432	1.904	0.942
	Logsig-Tansig	3.043	1.389	1.745	0.949	3.412	1.444	1.847	0.945
	Logsig-Logsig	2.922	1.361	1.709	0.952	3.329	1.386	1.824	0.948

**Table 5- Results of combining ANN-HS in order to simulate water level variations of piezometers of Jiroft Dam**

Piezometer	ANN-HS	Train				Test			
		MSE (m <sup>2</sup> )	MAE (m)	RMSE (m)	R	MSE (m <sup>2</sup> )	MAE (m)	RMSE (m)	R
20	Tansig-Tansig	8.997	2.212	2.999	0.955	7.928	2.297	2.815	0.965
	<b>Tansig-Logsig</b>	<b>12.459</b>	<b>2.230</b>	<b>3.529</b>	<b>0.946</b>	<b>4.479</b>	<b>1.599</b>	<b>2.116</b>	<b>0.988</b>
	Logsig-Tansig	16.502	2.767	4.062	0.933	5.909	1.929	2.431	0.975
	Logsig-Logsig	9.584	2.272	3.095	0.953	5.171	1.833	2.274	0.981
28	<b>Tansig-Tansig</b>	<b>6.051</b>	<b>1.709</b>	<b>2.459</b>	<b>0.967</b>	<b>11.399</b>	<b>2.465</b>	<b>3.376</b>	<b>0.933</b>
	Tansig-Logsig	4.731	1.513	2.175	0.974	14.659	3.044	3.829	0.934
	Logsig-Tansig	6.839	1.905	2.615	0.962	12.510	2.749	3.537	0.931
	Logsig-Logsig	7.794	1.948	2.792	0.958	16.840	3.370	4.104	0.927
30	Tansig-Tansig	2.593	1.226	1.610	0.960	5.381	1.689	2.319	0.919
	Tansig-Logsig	2.118	1.195	1.455	0.965	3.638	1.572	1.907	0.949
	<b>Logsig-Tansig</b>	<b>3.311</b>	<b>1.369</b>	<b>1.819</b>	<b>0.951</b>	<b>3.107</b>	<b>1.385</b>	<b>1.763</b>	<b>0.949</b>
	Logsig-Logsig	2.754	1.181	1.659	0.956	5.010	1.833	2.238	0.932

Based on the results obtained from the two classification and regression decision trees, it was

concluded that the regression decision tree had the best performance for all three piezometers (Table 6).

The results obtained from all methods are summarized in Table (6). The results shown for all methods calculated statistical parameters are at the suitable level, which implies that all soft computing technics predict water levels with high accuracy.

**Table 6- Comparing the performance of all the applied methods used in this study**

Piezometer	MODEL	Train				Test			
		MSE (m <sup>2</sup> )	MAE (m)	RMSE (m)	R	MSE(m <sup>2</sup> )	MAE (m)	RMSE (m)	R
20	<b>ANN-PSO</b>	<b>4.621</b>	<b>1.300</b>	<b>2.149</b>	<b>0.977</b>	<b>2.533</b>	<b>1.194</b>	<b>1.592</b>	<b>0.990</b>
	ANN-HS	12.459	2.230	3.529	0.946	4.479	1.599	2.116	0.988
	ANN-LM	2.712	1.016	1.647	0.987	4.077	1.667	2.019	0.991
	CDT	72.471	4.464	8.513	0.736	94.884	5.993	9.740	0.577
	RDT	4.725	0.887	2.173	0.976	13.987	1.767	3.739	0.948
	MLR	25.145	4.024	5.014	0.869	22.898	3.652	4.785	0.898
28	ANN-PSO	5.611	1.511	2.369	0.968	11.549	2.736	3.398	0.945
	<b>ANN-HS</b>	<b>6.051</b>	<b>1.709</b>	<b>2.459</b>	<b>0.967</b>	<b>11.399</b>	<b>2.465</b>	<b>3.376</b>	<b>0.933</b>
	ANN-LM	3.251	1.151	1.803	0.982	16.542	3.040	4.067	0.921
	CDT	22.438	2.753	4.736	0.908	41.285	4.842	6.425	0.784
	RDT	2.049	0.913	1.431	0.988	16.973	2.353	4.119	0.903
	MLR	12.372	2.946	3.517	0.928	19.802	3.801	4.449	0.884
30	ANN-PSO	2.922	1.361	1.709	0.952	3.329	1.386	1.803	0.948
	<b>ANN-HS</b>	<b>3.311</b>	<b>1.369</b>	<b>1.819</b>	<b>0.951</b>	<b>3.107</b>	<b>1.385</b>	<b>1.763</b>	<b>0.949</b>
	ANN-LM	1.046	0.746	1.023	0.982	6.780	2.035	2.604	0.935
	CDT	11.502	2.128	3.391	0.847	13.856	2.727	3.722	0.799
	RDT	0.475	0.417	0.689	0.992	3.345	1.173	1.829	0.940
	<b>MLR</b>	<b>2.834</b>	<b>1.336</b>	<b>1.683</b>	<b>0.952</b>	<b>3.067</b>	<b>1.450</b>	<b>1.751</b>	<b>0.945</b>

The obtained results indicate that for piezometer 20, the best performance was related to the ANN-PSO method, while piezometer 28 and 30 exhibited their best performance with ANN-HS and MLR methods, respectively.

In order to achieve a better understanding of the findings derived from the methods used in the present study, the obtained results are represented as dispersion diagrams for piezometers 20, 28, and 30 in Figures (6) to (8).

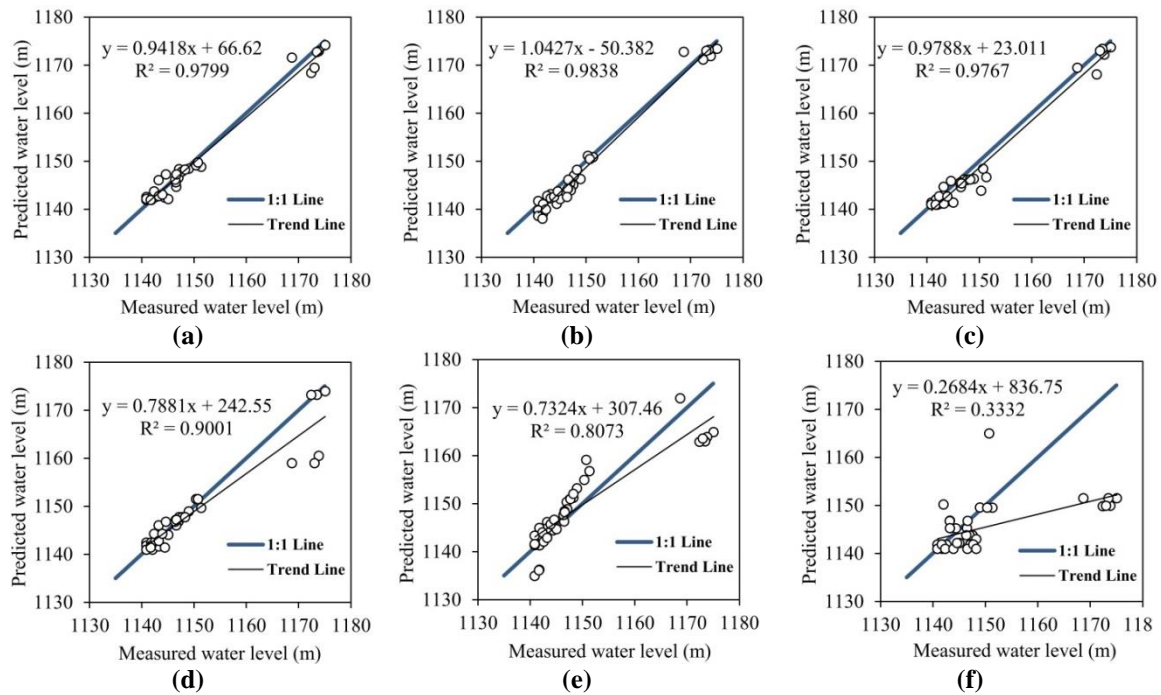


**Figure 6. Results obtained from data-driven models in test stage for simulating piezometer 20 level variations; (a) ANN-PSO, (b) ANN-LM, (c) ANN-HS, (d) RDT, (e) MLR, (f) CDT**

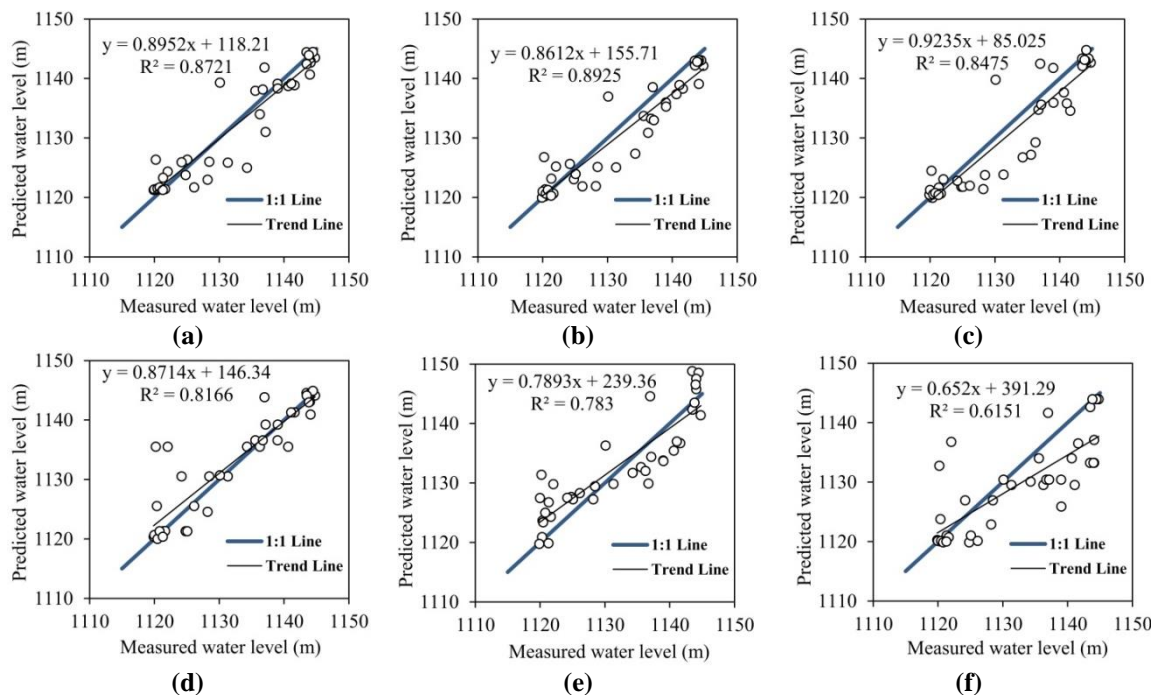


**Figure 7- Results obtained from data-driven models in test stage for simulating piezometer 28 level variations; (a) ANN-HS, (b) ANN-PSO, (c) ANN-LM, (d) RDT, (e) MLR, (f) CDT**

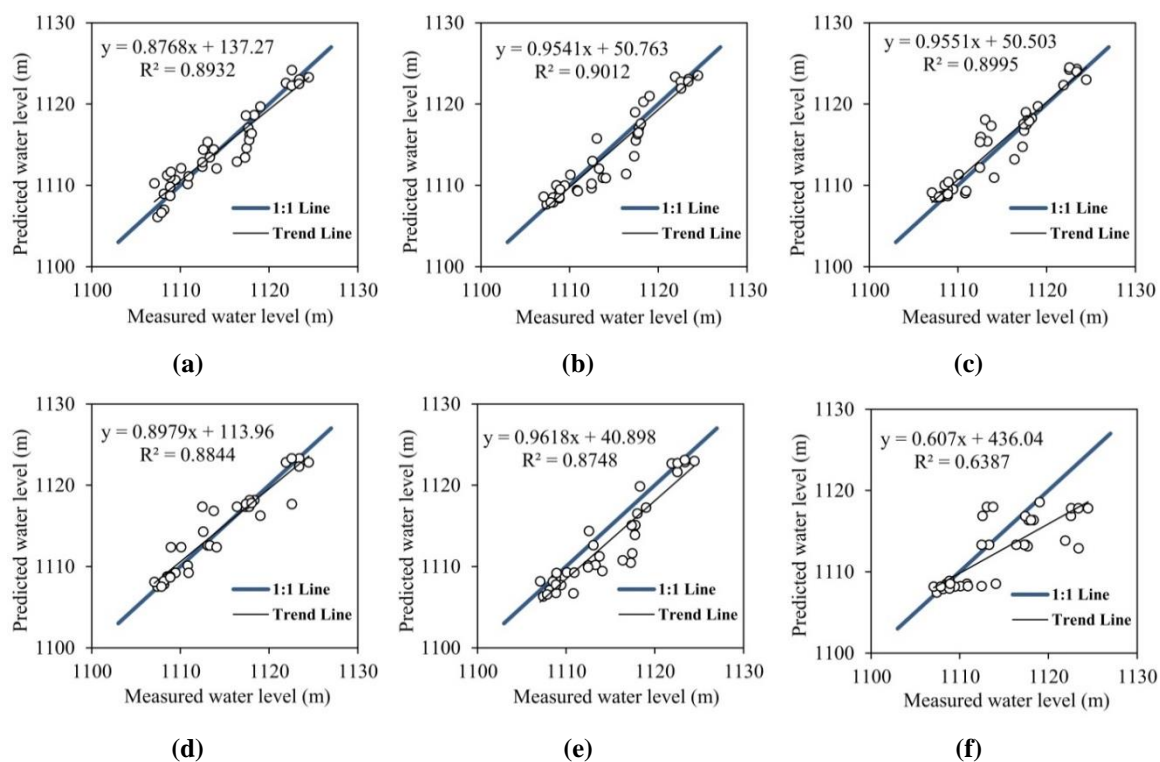


**Figure 8. Results obtained from data-driven models in test stage for simulating piezometer 30 level variations; (a) MLR, (b) ANN-HS, (c) ANN-PSO, (d) RDT, (e) ANN-LM, (f) CDT**

For piezometer 20, the best performance was obtained by combination ANN-PSO algorithm (considering RMSE criterion), while piezometer 28 exhibited its best performance in combination of ANN-HS algorithm. Besides, piezometer 30 showed its best performance by applying MLR method.

The Man-Whitney test can be used to investigate two groups' dependence or independence from the observed data. The initial hypothesis ( $H_0$ ) is that the two groups of data are equal, and the hypothesis-1 is that the average of the two groups of data are not statistically equal at a certain confidence level. The correct hypothesis can be determined by calculating the p-value at the given confidence level ( $\alpha$ ); so that, if the p-value is smaller than  $\alpha$ , the  $H_0$  (equality of the two groups) will be rejected, and otherwise it will be accepted. In the present study, in order to answer the question that whether or not different soft computing methods used in the study have statistically significant differences, it was attempted to statistically investigate the case and perform the Man-Whitney test, the results of which are provided in Table (7).

**Table 7- Statistical investigation of results obtained via Man-Whitney method**

Piezometer	Model	p-value	Significantly different (95%)	Significantly different (99%)
20	Observed vs. ANN-LM	0.142	NO	NO
	Observed vs. ANN-HS	0.156	NO	NO
	Observed vs. ANN-PSO	0.872	NO	NO
	Observed vs. CDT	0.136	NO	NO
	Observed vs. RDT	0.979	NO	NO
	Observed vs. MLR	0.433	NO	NO
28	Observed vs. ANN-LM	0.483	NO	NO
	Observed vs. ANN-HS	0.921	NO	NO
	Observed vs. ANN-PSO	0.491	NO	NO
	Observed vs. CDT	0.135	NO	NO
	Observed vs. RDT	0.815	NO	NO
	Observed vs. MLR	0.659	NO	NO
30	Observed vs. ANN-LM	0.123	NO	NO
	Observed vs. ANN-HS	0.736	NO	NO
	Observed vs. ANN-PSO	0.533	NO	NO
	Observed vs. CDT	0.106	NO	NO
	Observed vs. RDT	0.921	NO	NO
	Observed vs. MLR	0.831	NO	NO

In Table (7), the results of the data driven models obtained by various methods were evaluated using Man-Whitney test. The results in Table (7) indicate that in all the models used in this study there was no significant difference between the modelling methods.

In this study, the hydraulics of governing equations for modelling the piezometric are actually captured by the black-box nature of the ANN models by adjusting synaptic weights in their structure. It is highly recommended to compare the results of numerical/mathematical methods for predicting the piezometric with the soft computing models. However, due to the limitation of having precise databases (such as hydraulic conductivity coefficient in the body of dam/foundation) for setting up numerical/mathematical, this could not be achieved in this study.

#### 4. Conclusion

Soft computing is of special importance for solving the nonlinear problems. In this regard, the ANNs as well as their combination with meta-heuristic algorithms are highly regarded in solving the engineering problems. These networks are indeed powerful tools for optimizing the learning and generalizing the training samples; besides, they are among the most important soft computing sub-branches of the decision trees, which are commonly capable to predict and classify the quantitative and qualitative data and are widely used for solving the hydraulic and non-hydraulic problems.

Moreover, they are among the major effective parameters in dams' stability as well as its

relevant problems; therefore, dam seepage monitoring and also dam surveillance are of special importance for the safety of the dam. On this basis, the present study attempted to investigate the prediction of water level of piezometers of double-curvature arch dam using feed-forward multi-layer artificial neural network (FNN) with Levenberg-Marquardt optimization algorithm as well as PSO and HS algorithms along with classification and regression decision trees and multivariate linear regression model. Despite the appropriate performance of the methods used in simulating the piezometric water level variations, analysis of the statistical results of the used methods revealed the superiority of none of the method over the other ones.

## References

1. Rankovic, V. Novakovic, A. Grujovic, N. Divac, D. & Milivojevic, N. 2014 Predicting piezometric water level in dam via artificial neural network. *Neural Computing & Applications* 24 (5), 1115-1121.
2. Li, M. C. Guo, X. Y. Shi, J. & Zhu, Z. B. 2015 Seepage and stress of anti- seepage structures constructed with different concrete materials in an RCC gravity dam. *Water Science and Engineering* 8 (4), 326-334.
3. Tan, X. Wang, X. Khoshnevisan, S. & Hou, X. 2017 Seepage analysis of earth dams considering spatial variability of hydraulic parameters. *Engineering Geology* 228, 260-269.
4. Xiang, Y. Fu, Y. S. Zhu, K. Yuan, H. & Fang, Z. Y. 2017 Seepage safety monitoring model of an earth rock dam under influence of high-impact typhoons on particle swarm optimization method. *Water science and Engineering* 10 (1), 70-77.
5. Zhou, C. B. Liu, W. Chen, Y. F. Hu, R. & Wei, K. 2015 Inverse modeling of leakage through a rockfill dam foundation during its construction stage using transient flow model, neural network and genetic algorithm. *Engineering Geology* 187, 183-195.
6. Su, H. Tian, S. Kang, Y. Xie, W. & Chen, J. 2017 Monitoring water seepage velocity in dikes using distributed optical fiber temperature sensors. *Automation in Construction* 76, 71-84.
7. Turkmen, S. Ozguler, E. Taga, H. & Karaogullarindan, T. 2002 Seepage problems in the karstic limestone foundation of the Kalecik Dam (south Turkey). *Engineering Geology* 63 (3-4), 247-257.
8. Tayfur, G. Swiatek, D. Wita, A. & Singh, V.P. 2005 Case study: finite element method and artificial neural network models for flow through Jeziorsko Earthfill Dam in Poland. *Journal of Hydraulic Engineering* 131 (6), 431-440.
9. Gholizadeh, S. & Seyedpoor, S. M. 2011 Shape optimization of arch dam by metaheuristics and neural networks for frequency constraints *Science Iranica* 18 (5), 1020-1027.



10. Stojanovic, B. Milivojevic, M. Milivojevic, N. & Antonijevic, D. 2016 A self-tuning system for dam behavior modeling based on evolving artificial neural network. *Advances in Engineering Software* 97, 85-95.
11. Nourani, V. Mousavi, S. Sadikoglu, F. & Singh, V. 2017 Experimental and AI-based numerical modeling of contaminant transport in porous media. *Journal of Hydrology* 205, 78-95.
12. Peymab Company. 1991 Report of Jiroft Dam Study.
13. Zounemat-Kermani, M., 2012 Hourly predictive Levenberg–Marquardt ANN and multi linear regression models for predicting of dew point temperature. *Meteorology and Atmospheric Physics*, 117(3-4), 181-192.
14. Breiman, L. Friedman, J. H. Olshen, R. A. & Stone, C.J. 1984 Classification and regression tree. Chapman & Hall/CRC.
15. Swetapadma, A., & Yadav, A. (2017). A novel decision tree regression-based fault distance estimation scheme for transmission lines. *IEEE Transactions on Power Delivery*, 32(1), 234-245.
16. Lagacherie, P. & Holmes, S. 1997 Addressing geographical data errors in a classification tree for soil unit prediction. *International Journal Geographical Information Science* 11 (2), 183-198.
17. Salazar, F. Toledo, M. A. Onate, E. & Suarez, B. 2016 Interpretation of dam deformation and leakage with boosted regression tree. *Engineering Structures* 119, 230-251.
18. Nerini, D. Durbec, J. P. Mante, C. Garcia, F. & Ghattas, B. 2000 Forecasting physicochemical variables by a classification tree method application to the Berre Lagoon (South France). *Acta Biotheoretica* 48 (3-4), 181-196.
19. Paensuwan, N. Yokoyama, A. Verma, S.C. & Nakachi, Y. 2011 Application of Decision Tree Classification to the Probabilistic TTC Evaluation. *Journal of International Council on Electrical Engineering* 1 (3), 223-330
20. Seyedashraf, O. Rezaei, A. & Akhtari, A. A. 2017 Dam break flow solution using artificial neural network. *Ocean Engineerig* 142, 125-132.
21. Zounemat-Kermani, M., 2014 Principal component analysis (PCA) for estimating chlorophyll concentration using forward and generalized regression neural networks. *Applied Artificial Intelligence*, 28(1), pp.16-29.
22. Sapna, S. Tamilarasi, A. & Kumar, M. P. 2012 Backpropagation Learning Algorithm Based on Levenberg Marquardt Algorithm. *Computer Science & Information Technology* 07, 393-398.

23. Alsmadi, M. K. S. Omar, K. B. & Noah, S.A. 2009 Back Propagation Algorithm: The Best Algorithm among Multi-layer Perceptron Algorithm. *International Journal of Computer Science and Network Security*. 9,378-383.
24. Hamid, N. A. Nawi, N. M. GhaZali, R. & Salleh, M. N. M . 2011 Accelerating Learning Performance of Back Propagation Algorithm by Using Adaptive Gain Together with Adaptive Momentum and Adaptive Learning Rate on Classification Problems. *International Journal of Software Engineering and its Applications* 5, 31-44.
25. Zounemat-Kermani, M., Kisi, O. and Rajaei, T., 2013. Performance of radial basis and LM-feed forward artificial neural networks for predicting daily watershed runoff. *Applied Soft Computing*, 13(12), pp.4633-4644.
26. Kennedy, J. Eberhart, R. 1995 Particle swarm optimization. In: *Proceedings of the 1995 IEEE International Conference on Neural Networks*, Perth, 4, 1942-1948.
27. Chau, K.W. 2006 Particle swarm optimization training algorithm for ANNs in stage prediction of Shing Mun River. *Journal of Hydrology* 329 (3-4), 363-367.
28. Gyanesh, D. Prasant, K. P. & Sasmita, K. P. 2014 Artificial Neural Network trained by particle swarm optimization for non-linear channel equalization. *Expert Systems with Application* 41 (7), 3491-3496.
29. Xiang, Y. Fu, Y. S. Zhu, K. Yuan, H. & Fang, Z. Y. 2017 Seepage safety monitoring model of an earth rock dam under influence of high-impact typhoons on particle swarm optimization method. *Water science and Engineering* 10 (1), 70-77.
30. Mun, S. & Cho, Y. H. 2012 Modified harmony search optimization for constrained design problems. *Expert Systems Applications* 39 (1), 419-423.
31. Geem, Z. W. Kim, J. & Loganathan, G. 2002 Harmony search optimization: Application to pipe network design. *International Journal of Model Simulation* 22, 125-133.
32. Yadav, P. Kumar, R. Panda, S. K. Chang, C.S. 2012 An Intelligent Tuned Harmony Search algorithm for optimization. *Information science* 196, 47-72.
33. Ruby, M. & Botez, R. M. 2016 Trajectory Optimization for vertical navigation using the Harmony Search algorithm. *IFAC-PapersOnLine* 49 (17), 11-16.



© 2018 by the authors. Licensee SCU, Ahvaz, Iran. This article is an open access article distributed under the terms and conditions of the Creative Commons Attribution 4.0 International (CC BY 4.0 license) (<http://creativecommons.org/licenses/by/4.0/>).





نشریه تخصصی

# سازه های هیدرولیکی

صاحب امتیاز: دانشگاه شهید چمران اهواز

مدیر مسئول: دکتر حمیدرضا غفوری

سر دبیر: دکتر علی حقیقی

مدیر داخلی: دکتر سید محمد اشرفی

گروه مهندسی عمران، دانشکده مهندسی، دانشگاه شهید چمران اهواز، اهواز، ایران

دارای اعتبار علمی پژوهشی از وزارت علوم تحقیقات و فناوری

Print ISSN: 2345-413X

Online ISSN: 2345-5156



## اعضای هیأت تحریریه

### دکتر حسین محمدولی سامانی

گروه مهندسی عمران، دانشکده مهندسی، دانشگاه شهید چمران اهواز  
(تخصص: سازه های هیدرولیکی)

### دکتر محمود شفاعی بجستان

گروه سازه های آبی، دانشکده مهندسی علوم آب، دانشگاه شهید چمران اهواز  
(تخصص: سازه های هیدرولیکی)

### دکتر علی حقیقی

گروه مهندسی عمران، دانشکده مهندسی، دانشگاه شهید چمران اهواز  
(تخصص: آب و فاضلاب و هیدرولیک)

### دکتر محمدسیروس پاکباز

گروه مهندسی عمران، دانشکده مهندسی، دانشگاه شهید چمران اهواز  
(تخصص: ژئوتکنیک)

### دکتر سعیدرضا صباغ یزدی

دانشکده مهندسی عمران، دانشگاه صنعتی خواجه نصیرالدین طوسی (تخصص: سازه های هیدرولیکی و مدل سازی عددی)

### دکتر مجتبی لیب زاده

گروه مهندسی عمران، دانشکده مهندسی، دانشگاه شهید چمران اهواز (تخصص: سازه و سازه های هیدرولیکی)

### دکتر هلنا راموس

گروه مهندسی عمران، دانشگاه لیسبون پرتغال (تخصص: هیدرولیک سیستم های تحت فشار و هیدروانفورماتیک)

### دکتر عبدالرسول تلوری

گروه مهندسی عمران، دانشگاه آزاد اسلامی، واحد تهران شمال  
(تخصص: هیدرولوژی و منابع آب)

### دکتر آرش ادیب

گروه مهندسی عمران، دانشکده مهندسی، دانشگاه شهید چمران اهواز  
(تخصص: هیدرولوژی و منابع آب)

### دکتر سید عباس حق شناس

گروه فیزیک فضا، موسسه ژئوفیزیک دانشگاه تهران (تخصص: سواحل و بنادر)

### دکتر محمد واقفی

گروه مهندسی عمران، دانشکده فنی و مهندسی، دانشگاه خلیج فارس (تخصص: سازه های هیدرولیکی)

### دکتر محمد ذونعمت کرمانی

بخش مهندسی آب، دانشگاه شهید باهنر کرمان (تخصص: هیدرولیک محاسباتی)

### دکتر طاهر رجایی

گروه مهندسی عمران، دانشکده فنی و مهندسی، دانشگاه قم (تخصص: آب و محیط زیست)

# Journal of Hydraulic Structures

Scientific Professional Journal

## Contents

Volume 4, Issue 2, Autumn 2018

**A Mass Conservative Method for Numerical Modeling of Axisymmetric flow (1-9)**

R. Asadi

**Development of A new Hydraulic Relationship for Submerged Slide Gates (10-16)**

S. Jahan Kohan; Hossein M.V. Samani; H. Ebrahimi

**Effect of rice husk ash on the swelling pressure of bentonite soil stabilized with lime in the presence or lack of sulfate (17-26)**

Mohammad S. Pakbaz; S. SeyedAlizadeh Ganji

**Characteristic Based Split Finite Element for Unsteady Dam-Break Problem (27-41)**

J. Parsa

**Boundary Integral Equations for Quasi-Static Unsaturated Porous Media (42-59)**

E. Jabbari; M. Behnia

**Evaluating performance of meta-heuristic algorithms and decision tree models in simulating water level variations of dams' piezometers (60-80)**

R. Salajegheh; A. Mahdavi-Meymand; M. Zounemat-Kermani



**Address:**

Department of Civil Engineering, Faculty of Engineering, Shahid Chamran University of Ahvaz

Phone: +986133330011, +986133330012

Website: [jhs.scu.ac.ir](http://jhs.scu.ac.ir)

Email: [jhs@scu.ac.ir](mailto:jhs@scu.ac.ir)

Ahvaz, Khuzestan Province, Iran